

University of Louisville

ThinkIR: The University of Louisville's Institutional Repository

Electronic Theses and Dissertations

5-2023

Engineering 3D architected metamaterials for enhanced mechanical properties and functionalities.

Huan Jiang
University of Louisville

Follow this and additional works at: <https://ir.library.louisville.edu/etd>



Part of the [Applied Mechanics Commons](#), [Computer-Aided Engineering and Design Commons](#), and the [Manufacturing Commons](#)

Recommended Citation

Jiang, Huan, "Engineering 3D architected metamaterials for enhanced mechanical properties and functionalities." (2023). *Electronic Theses and Dissertations*. Paper 4053.

Retrieved from <https://ir.library.louisville.edu/etd/4053>

This Doctoral Dissertation is brought to you for free and open access by ThinkIR: The University of Louisville's Institutional Repository. It has been accepted for inclusion in Electronic Theses and Dissertations by an authorized administrator of ThinkIR: The University of Louisville's Institutional Repository. This title appears here courtesy of the author, who has retained all other copyrights. For more information, please contact thinkir@louisville.edu.

ENGINEERING 3D ARCHITECTED METAMATERIALS FOR ENHANCED
MECHANICAL PROPERTIES AND FUNCTIONALITIES

By

Huan Jiang

A Dissertation

Submitted to the Faculty of the
J.B. Speed School of Engineering of the University of Louisville
in Fulfillment of the Requirements
for the Degree of

Doctor of Philosophy
in Mechanical Engineering

Department of Mechanical Engineering
University of Louisville
Louisville, Kentucky, United States

May, 2023

Copyright 2023 by Huan Jiang

All rights reserved

ENGINEERING 3D ARCHITECTED METAMATERIALS FOR ENHANCED
METAMATERIALS AND FUNCTIONALITIES

By

Huan Jiang

A Dissertation Approved on

February 25, 2023

by the following Dissertation Committee:

Dr. Yanyu Chen

Dissertation Chairman

Dr. Shamus McNamara

Committee member

Dr. Roger Bradshaw

Committee member

Dr. Thomas Berfield

Committee member

DEDICATION

This dissertation is dedicated to my parents

Mrs. Shi-Ying Xu

and

Mr. Yong-Hao Jiang

for their endless love, sacrifice, and guidance throughout my life

ACKNOWLEDGEMENT

First and foremost, I am extremely grateful to my PhD supervisor, Dr. Yanyu Chen, for his invaluable mentorship and friendship throughout this journey. I thank him for providing insightful feedback, sharing his valuable expertise, and for guiding me throughout the research studies at University of Louisville. He is more than an advisor, but a role model that I wish I could become in the future. I will always be grateful to you for your support and kindness.

I greatly acknowledge Prof. Shamus McNamara, Dr. Roger Bradshaw, Dr. Thomas Berfield for being on my dissertation committee. Special thanks to Dr. Xin-Lin Gao at Southern Methodist University for his valuable suggestions during my PhD journey. Thanks to Dr. Lei Liu, Dr. Zian Jia, Dr. Tian Yu, Dr. Heng Zhang for beneficial discussions. I would also like to thank Dr. Peter Quesada and Dr. Kevin Murphy for their help during my research study at University of Louisville. I would like to extend my gratitude to the Mechanical department, professors and the staffs, Dr. Srinivasan Rasipuram, John Jones and Diane Jenne.

I also would like to take this opportunity to thank my lab mate and colleagues Zhennan Zhang, Dr. Faith Usta, Dr. Sandipan Banerjee, Ahmed Islam, Kavish Sudan, Pavan Ajjarapu, Saransh Gupta, Varun Shreyas, Ranga Pidathala, Shruti Kumar, Akhil Tantry, Shihan Zhang, Pu Han, Sontush Rauniyar, Sumit Paul, Naresh Koju, Julio Izquierdo, Hannah Ziegler and Aaron Coomes for their help and support throughout my time at University of Louisville.

Finally, I would specially like to thank my parents and brother for their unequivocal support.

ABSTRACT

ENGINEERING 3D ARCHITECTED METAMATERIALS FOR ENHANCED METAMATERIALS AND FUNCTIONALITIES

Huan Jiang

February 26, 2023

Compared with conventional materials, architected metamaterials have shown unprecedented mechanical properties and functionalities applications. Featured with controlled introduction of porosity and different composition, architected metamaterials have demonstrated unprecedent properties not found in natural materials. Such design strategies enable researchers to tailor materials and structures with multifunctionalities and satisfy conflicting design requirements, such as high stiffness and toughness; high strength with vibration mitigation properties, etc. Furthermore, with the booming advancement of 3D printing technologies, architected materials with precisely defined complex topologies can be fabricated effortlessly, which in turn promotes the research significantly. The research objectives of this dissertation are to achieve the enhanced mechanical properties and multifunctionalities of architected metamaterials by integrative design, computational modeling, 3D printing, and mechanical testing.

Phononic crystal materials are capable of prohibiting the propagation of mechanical waves in certain frequency ranges. These certain frequency ranges are represented by phononic band gaps. Formally, band gaps are formed through two main mechanisms, Bragg scattering and local resonance. Band gaps induced by Bragg scattering are dependent on periodicity and the symmetry of the lattice. However, phononic crystals with Bragg-type band gaps are limited in their application because they do not attenuate vibration at lower frequencies without requiring large geometries. It is not practical to build huge models to achieve low frequency vibration mitigation. Alternatively, band gaps formed by local resonance are due to the excitation of resonant frequencies, and these band gaps are independent of periodicity. Therefore, lower frequency band gaps have been explored mostly through the production of phononic metamaterials that exploit locally resonant masses to absorb vibrational energy. However, despite research advances, the application of phononic metamaterials is still largely hindered by their limited operation frequency ranges. Designing lightweight phononic metamaterials with low-frequency vibration mitigation capability is still a challenging topic. On the other hand, conventional phononic crystals usually exhibit very poor mechanical properties, such as low stiffness, strength, and energy absorption. This could largely limit their practical applications. Ideally, multifunctional materials and structures with both vibration mitigation property and high mechanical performance are demanded. In this work, we propose architected polymer foam material to overcome the challenges.

Beside altering the topological architecture of metamaterials, tailoring the composition of materials is another approach to enhance the mechanical properties and realize multifunctionalities. Natural materials have adopted this strategy for long period of time.

Biological structural materials such as nacre, glass sea sponges feature unusual mechanical properties due to the synergistic interplay between hard and soft material phases. These exceptional mechanical performance are highly demanded in engineering applications. As such, intensive efforts have been devoted to developing lightweight structural composites to meet the requirements. Despite the significant advances in research, the design and fabrication of low-cost structural materials with lightweight and superior mechanical performance still represent a challenge. Taking inspiration from cork material, we propose a new type of multilayered cellular composite (MCC) structure composed of hard brittle and soft flexible phases to tackle this challenge.

On the other hand, piezoelectric materials with high sensitivity but low energy absorption have largely limited their applications, especially during harsh environment where external load could significantly damage the materials. Enlightened by the multiphase composite concept, we apply this design motif to develop a new interpenetrating-phased piezoelectric materials by combining PZT material as skeleton and PDMS material as matrix. By using a facial camphene-templated freeze-casting method, the co-continuous composites are fabricated with good quality. Through experiment and simulation studies, the proposed composite demonstrates multifunction with exceptional energy absorption and high sensitivity. Based on the above experimental studies, we further propose to use topology optimization framework to obtain the composites with the best performance of multifunctionalities. Specifically, we will use the solid isotropic material with penalization (SIMP) approach to optimize the piezoelectric materials with multi-objectives of 1) energy absorption and 2) electric-mechanical conversion property. The materials for the optimization design will be elastic PZT as skeleton and elastic material

PDMS as matrix. To enable the gradient search of objective function efficiently, we will use adjoint method to derive the shape sensitivity analysis.

TABLE OF CONTENTS

| | |
|--|----|
| CHAPTER 1 | 1 |
| INTRODUCTION | 1 |
| 1.1 Overview of architected materials | 1 |
| 1.2 Background and motivation | 4 |
| 1.2.1 architected materials for vibration attenuation..... | 4 |
| 1.2.2 Mechanical performance of architected foams under large deformation..... | 6 |
| 1.2.3 Mechanical and piezoelectric performance of multiphase metamaterials | 8 |
| 1.2.4 Topology optimization of multifunctional composites | 12 |
| CHAPTER 2 | 15 |
| MATERIALS AND METHODS..... | 15 |
| 2.1 Periodic structures and wave propagation | 15 |
| 2.2 Finite element simulations | 17 |
| 2.3 3D printing of architected metamaterials..... | 21 |
| 2.4 Mechanical testing | 23 |
| CHAPTER 3 | 24 |
| 3D ARCHITECTED HOLLOW SPHERE FOAMS FOR NOISE AND VIBRATION IN CONTROL..... | 24 |
| 3.1 Introduction..... | 24 |
| 3.2 Model description | 26 |
| 3.3 Numerical model validation with experiment..... | 27 |
| 3.4 Design flexibility of phononic band gaps | 31 |
| 3.4.1 Effect of geometric parameters | 31 |
| 3.4.2 Effect of stiffness contrast..... | 33 |
| 3.4.3 Effect of lattice symmetry | 36 |
| 3.5 Simultaneous existence of omnidirectional acoustic and elastic band gaps | 38 |
| 3.6 Conclusions..... | 42 |
| CHAPTER 4 | 44 |

| | |
|---|-----|
| 3D PRINTED ARCHITECTED POLYMER FOAM FOR ENHANCED MECHANICAL PROPERTIES | 44 |
| 4.1 Introduction..... | 44 |
| 4.2 Model description | 46 |
| 4.3 Results and discussion | 49 |
| 4.3.1 Effect of binder size | 49 |
| 4.3.2 Effect of shell thickness | 56 |
| 4.3.3 Effect of different graded design strategies | 62 |
| 4.3.4 Comparison of graded designs with existing architected materials | 69 |
| 4.4 Conclusions..... | 74 |
| CHAPTER 5 | 76 |
| MULTIPHASE COMPOSITES WITH EXCEPTIONAL MECHANICAL PERFORMANCE... | 76 |
| 5.1 Introduction..... | 76 |
| 5.2 Bioinspired multilayered composites for exceptional performance..... | 78 |
| 5.2.1 Model description | 78 |
| 5.2.2 Results and discussion | 81 |
| 5.3 Conclusions..... | 95 |
| CHAPTER 6 | 97 |
| PIEZOELECTRIC COMPOSITES WITH MULTIFUNCTIONALITIES AND TOPOLOGY OPTIMIZATION | 97 |
| 6.1 Introduction..... | 97 |
| 6.2 3D piezoelectric composites with high energy absorption and sensing..... | 100 |
| 6.2.1 Fabrication and structural characteristics..... | 100 |
| 6.2.2 The experimental set-up for impact test and d_{33} measurement of the PZT-PDMS composites..... | 103 |
| 6.2.3 Experimental energy-absorbing behaviors..... | 105 |
| 6.2.4 The experimental set-up and method of the d_{33} measurement of the PZT-PDMS piezoelectric composites | 111 |
| 6.2.5 Impact loading monitoring..... | 112 |
| 6.2.6 Dynamic compressive loading measurement..... | 117 |
| 6.3 Topology optimization of piezoelectric composites | 119 |
| 6.3.1 SIMP for elastic compliance optimization..... | 120 |
| 6.3.2 Finite element verification for piezoelectricity | 123 |
| 6.3.3 Topology optimization of piezoelectric composite..... | 125 |

| | |
|------------------------------|-----|
| 6.4 Conclusions..... | 130 |
| CHAPTER 7 | 132 |
| CONCLUSIONS AND OUTLOOK..... | 132 |
| 7.1 Main contributions | 132 |
| 7.2 Future work..... | 135 |
| REFERENCES | 137 |
| CURRICULUM VITAE | 149 |

LIST OF TABLES

| | |
|---|----|
| Table 1 The parameters of the models with volume fraction from 10% to 50% | 79 |
|---|----|

LIST OF FIGURES

| | |
|--|----|
| Figure 1 Application of architected metamaterials in different industry sectors..... | 3 |
| Figure 2 Schematic of a two-dimensional periodic lattice structure..... | 16 |
| Figure 3 Stress-strain relation from experimental data..... | 20 |
| Figure 4 Geometric description of the proposed architected hollow sphere foam (AHSF) with a body-centered-cubic (BCC) lattice symmetry. | 27 |
| Figure 5 Elastic wave transmission test on the 3D printed AHSF and numerical modeling validation..... | 29 |
| Figure 6 Effects of binder and hollow sphere geometric features on the phononic band gap properties..... | 32 |
| Figure 7 Effect of stiffness contrasts between spheres and binders on phononic dispersion relations of the AHSF with a BCC lattice symmetry..... | 34 |
| Figure 8 Effect of stiffness contrast on the first phononic band gap properties. | 36 |
| Figure 9 Effect of lattice symmetry and stiffness contrast on phononic dispersion relations | 37 |
| Figure 10 Acoustic and elastic dispersion relations for the conventional solid sphere foam and proposed hollow sphere foam proposed hollow sphere foam with $R/t = 10$ | 39 |

| | |
|---|----|
| Figure 11 Finite element simulated acoustic and elastic transmission along $\Gamma - H$ direction | 42 |
| Figure 12 Design and 3D printing of uniform foam (UF), graded binder foam (GBF), graded thickness foam (GTF), and hybrid graded foam (HGF) | 48 |
| Figure 13 Effect of binder size on mechanical performance | 51 |
| Figure 14 Effect of binder size on mechanical performance | 54 |
| Figure 15 Contour plots of Mises stress of different binder sizes | 55 |
| Figure 16 Effect of relative density on mechanical performance | 58 |
| Figure 17 Effect of relative density on mechanical performance | 59 |
| Figure 18 Contour plot of Mises stress of different relative densities | 61 |
| Figure 19 Effect of uniform and gradient design on mechanical performance | 63 |
| Figure 20 Effect of uniform and gradient design on mechanical performance | 66 |
| Figure 21 Contour plot of Mises stress of uniform and graded design models | 69 |
| Figure 22 Comparison of typical graded materials | 71 |
| Figure 23 Three architected materials with graded design | 72 |
| Figure 24 Mises stress distribution of three architected materials with graded design | 73 |
| Figure 25 The design process of the proposed multilayered cellular composites | 80 |
| Figure 26 Bioinspired multilayered cellular composite design and uniaxial compression tests | 81 |

| | |
|---|-----|
| Figure 27 Mechanical deformation of the 3D printed VW and MCC structures..... | 84 |
| Figure 28 | 87 |
| Figure 29 Measured strain evolution of the 3D printed samples..... | 88 |
| Figure 30 Simulated strain and von Mises stress evolution of the VW and MCC structures | 89 |
| Figure 31 Mechanical properties of the MCC configurations under cyclic loading tests | 92 |
| Figure 32 | 95 |
| Figure 33 Diagram of the fabrication processes for the IP3C based on camphene-templated freeze casting. | 101 |
| Figure 34 Structural characteristics of the as-fabricated 3-D interpenetrating-phase PDMS- PZT composites | 102 |
| Figure 35 Experiment setup for piezoelectric coefficient measurement | 103 |
| Figure 36 Experiment setup for impact test..... | 104 |
| Figure 37 “Quasi-static” unidirectional loading-unloading stress-strain curves of the IP3C and the corresponding non-structured 0-3 PZT-PDMS composite at 5% (solid line) and 10% (dashed line) strain, respectively..... | 106 |
| Figure 38 Simulated mechanical response of the PZT-PDMS composites under compression | 108 |
| Figure 39 Experimental mechanical characterizations of the PZT-PDMS composite under dynamic loading conditions | 109 |

| | |
|---|-----|
| Figure 40 Experiment setup for d33 measurement. | 111 |
| Figure 41 The experimental piezoelectricity of the IP3C..... | 114 |
| Figure 42 The simulated electric potential of piezoelectric composites..... | 115 |
| Figure 43 The electro-mechanical responses of the IP3C for the potential applications in impact sensing and energy harvesting | 116 |
| Figure 44 Comparison of interpenetrating phase composite and conventional composite. | 118 |
| Figure 45 The comparison of the properties of the proposed 3-D interpenetrating-phase PZT-PDMS composite with other materials..... | 119 |
| Figure 46 Numerical examples of beams for compliance optimization | 122 |
| Figure 47 Piezoelectric finite element code verification against ABAQUS..... | 125 |
| Figure 48 Topology optimization of piezoelectric composites considering linear elastic properties..... | 130 |

CHAPTER 1

INTRODUCTION

1.1 Overview of architected materials

Since the early 2000s, metamaterials have emerged as a rapidly growing interdisciplinary area, involving physics, engineering, materials science, optics, and nanoscience. The properties of metamaterials are tailored by manipulating their internal physical structure. This makes them remarkably different from natural materials, whose properties are mainly determined by their chemical constituents and bonds. Originating from creating artificial electromagnetic materials [1], metamaterial concept has extended to various fields, for example, phononic metamaterials [2, 3], thermal metamaterials [4, 5], phononic metamaterials [6, 7], mechanical metamaterials [8, 9] etc.

The term “architected material”, which also means metamaterial, was first used in an overview paper by Ashby and Brechet [10]. It was coined to make link between the practice in architecture and structural engineering which uses topology optimization to produce reliable, lightweight constructions. An architected material is combination of several materials with certain amount of porosity which can be configured to reach performances not offered by any individual material. Hence, there is clear target in terms of the properties and performance at the onset, which motivates and thereafter guides its development. Architected materials are unique, in the sense that the performance is exclusively controlled

by geometry at multiple length scales, rather than the chemical composition or processing alone.

Analogous to the lattice structure of a crystal in solid state physics, metamaterials typically refer to cellular materials with periodic arrangements of unit cells in two dimensions or representative volume element (RVE) in three dimensions [11]. Among various material architectures, metamaterials can achieve the highest structure efficiency per unit weight [12]. Therefore, they have been widely used in engineering applications where weight is critical, such as aerospace engineering, automobiles, medical engineering, etc. In recent years, the research interests in metamaterials has expanded broadly to solve the challenges that haven't been tackled before. Figure 1 summarizes some characteristics of architected metamaterials that are of particular interest in a wide range of engineering disciplines. New designs, functions, and applications are still quickly and continuously added to this figure.

The intensive research on architected metamaterials is attributed to mainly two factors. The one that comes first is the rapid progress in the development of the 3D printing technologies. Notably, the emergence of various additive manufacturing technologies enables fabrication of architected materials with significantly complex architectures, small scale prototypes, detailed features and excellent quality by using a variety of materials. Up to now, polymers, metals, and ceramics have been broadly used as the base material for additive manufacturing for the purpose of different applications. Correspondingly, the different additive manufacturing processes for disparate materials include stereolithography (SLA), fused deposition modeling (FDM), two-photon lithography, powder bed fusion, binder jetting, etc. Remarkably, the 3D nickel nano-architected

materials are fabricated by a lithography-based process [13], marking a milestone of 3D printed architected materials. The second factor is the advancement of the optimization algorithm and computational capability to handle large-scale models. Essentially, the design of architected materials is to find the architecture with material layouts. Computers with the efficient algorithms can determine the final topological architectures.

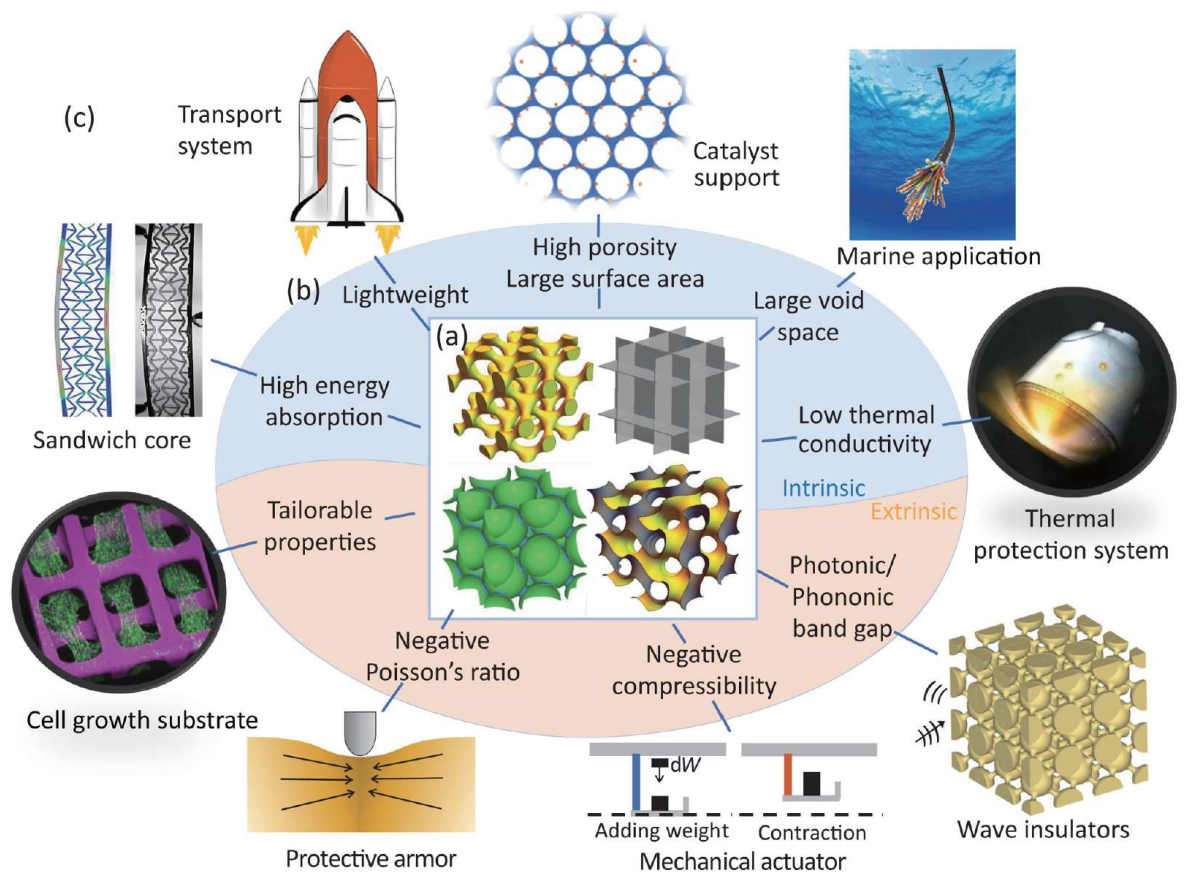


Figure 1 Application of architected metamaterials in different industry sectors

1.2 Background and motivation

1.2.1 architected materials for vibration attenuation

Noise and vibration are becoming an increasingly hazardous form of pollution as cities become busier and technology advances. Sources of noise and vibration pollution can be airborne or structural-borne and include construction, traffic, and wind. These undesired noises and vibration not only have negative impacts on the physical and social health by impacting sleep patterns, hearing abilities, and concentration [14, 15], but also deteriorate the structural integrity of civil infrastructures [16, 17] and the functionality of high-precision industrial equipment [18]. To control noise and vibration pollution, both active and passive control methods have been developed in the past few decades. Active noise control works best for mechanical waves that travel primarily in the longitudinal direction through gas mediums, such as air. Passive control involves the passing of waves through a soft or hard material so that the mechanical waves will either be dampened or reflected, respectively. While each method is effective in its own way, these control methods can contribute negatively to the cost or mass of a system and are not appropriate in all applications [19]. Many newly-developed composites such as carbon fiber-reinforced composites exhibit increased strength properties at the expense of noise and vibration control capabilities compared to more traditional soft bulk materials used in passive control approach [20]. For this reason, the architectures and mechanical properties of composite materials are being analyzed and optimized to exhibit enhanced strength and damping properties [21, 22]. Moving towards architected materials, which are rationally designed multiscale material systems, exhibit novel functionalities and unique properties that cannot be readily achieved in natural bulk solids [23, 24]. In addition to the unusual mechanical

and physical properties, architected materials have been designed and optimized for novel elastodynamic wave phenomena. One example of such architected materials is phononic metamaterial, which consists of periodically topological structures and materials dispersions and has the ability to manipulate the propagation of mechanical waves [25-32]. The periodic structures of phononic crystals produce omnidirectional band gaps-ranges of frequencies where elastic waves cannot propagate. In these band gaps, mechanical waves decay exponentially and are thus mitigated.

Intrinsically, phononic band gaps are formed through two main mechanisms, Bragg scattering and local resonance. Band gaps induced by Bragg scattering are dependent on order and the symmetry of the lattice and can be modified with a stronger or weaker mismatch in the mechanical impedance of a composite's materials [33, 34]. Band gaps form by way of local resonance due to the excitation of resonant frequencies; these band gaps are independent of periodicity [35-39]. Phononic crystals with Bragg-type band gaps are limited, however, in their application because they do not attenuate vibration at lower frequencies without requiring large geometries. Inducing these lower frequency band gaps is being achieved through the production of phononic metamaterials that exploit locally resonant masses to absorb energy [40]. Despite these advances, the application of phononic metamaterials is largely hindered by their limited operation frequency ranges and inferior mechanical properties. Designing lightweight phononic metamaterials with low-frequency vibration mitigation capability is still challenging.

In the past decades, hollow sphere foams (HSFs) have been investigated intensively, because of their exceptional acoustic properties. It has been demonstrated that both random and rationally designed HSFs can manipulate mechanical wave propagation. For instance,

perforated HSFs with wide acoustic attenuation ranges show great promise to serve as acoustic liners for airplane engines [41]. Our recent numerical work further demonstrates that perforated AHSFs can simultaneously control sound and elastic wave propagation [42]. In addition, HSFs offer manufacturing flexibility in material selection and can be assembled into relatively defect-free periodic structures [43, 44], making them ideal for use in multiple fields of application. Moving towards architected hollow sphere foams, we propose newly designed architected foam structure to tackle the challenge of low-frequency vibration mitigation.

1.2.2 Mechanical performance of architected foams under large deformation

On the other hand, materials and structures featured with high stiffness, strength, energy absorption, etc. are highly demanded in various applications, such as aerospace engineering, auto industry, defense industry, etc. Conventionally, random foam materials such as syntactic foams, Voronoi foams, and Alporas foams have been studied. For example, the mechanical behavior of a sandwich structure with syntactic foam core was investigated under quasi-static and dynamic loading [45]. It was found that the energy absorption increased by 23 % under dynamic load compared to a quasi-static load. The failure mechanism for syntactic foam under quasi-static and dynamic load was found to be shear cracking. Mechanical behavior of 3D Voronoi foam with closed-cell morphology was also studied [46]. It was shown that the plateau stress can increase by 8.6 times, and energy absorption can be enhanced by 8.5 times through manipulating the degree of the cell shape irregularity. Laguerre tessellation foam model was explored to show different responses to the variation of cell size and cell wall thickness [47]. It was found that the compressive and shear strength are more sensitive to cell size and thickness variation than

compressive and shear stiffness, and the combined effect of cell size and thickness on strength is less than the sum of their individual effects. Despite these prominent mechanical properties, the lack of control at the microstructural level for random foams poses a challenge for predicting the long-term stability in structure and performance [48][13]. In contrast, architected materials with rationally designed structures can be employed to achieve engineered mechanical properties and functionalities [49]. Architected materials, such as lattice [50] or honeycombs [51] have been reported to be significantly more structurally efficient than stochastic foams with the same relative density [52].

More recently, functionally graded design strategy (FGDS) has drawn much attention due to its capability to enable the creation of materials with lightweight, damage tolerant, and high energy absorption. FGDS was first proposed by Niino et al. [53] to overcome the huge temperature difference between the outer surface of the spacecraft and the internal space caused by air friction. Since then, this concept has enlightened researchers to create novel FGDS to achieve better mechanical performance. For example, additively manufactured BCC-lattice and BCCz-lattice of uniform and graded design were investigated by compressive experiments [54]. It was found that with the same amount of energy absorption, the densification for graded structure occurred at 7 % lower strain compared to the uniform one. This contributes to the impressive feature that the graded materials can absorb significantly more energy under compressive deformation than the uniform materials with the same volume fraction. Additionally, the uniform structure shows shear failure mode at the early stage of strain, while the graded structure exhibits a layer-by-layer failure mechanism. This can be employed to eliminate undesirable failure modes in lattice structures while maintaining high specific energy absorption.

Despite the above-mentioned development in architected materials for high mechanical performance, the materials featuring with simultaneous high mechanical performance and vibration mitigation is still a challenging topic. Following the architected hollow sphere foam structure model, we apply the graded design strategy to tackle this challenge. Using the experimental and numerical approaches, we will demonstrate that the architected hollow sphere foam structure can be featured with multifunctionality.

1.2.3 Mechanical and piezoelectric performance of multiphase metamaterials

Besides focusing on the architecture of the metamaterials as discussed before, tailoring the composition of materials is another approach to enhance the mechanical properties and realize multifunctionalities. Efforts have been devoted to develop multi-material lattices combining strength and ductility through multiphase designs. For example, metal-coated hybrid meso-lattice composites were studied for their mechanical performance; by combining multi-scale experimental analysis employing high-resolution imaging system with a simulation model that incorporates progressive damage and fracture mechanics, it was shown that the average stiffness and strength can be enhanced by 68.3% and 34.9% compared to the polymer only lattices [55]. Three-dimensional high-entropy alloy-polymer composite nanolattices were fabricated via two-phono lithography and magnetron sputtering deposition [56], it was reported that the composite nanolattices exhibit a high specific strength of $0.027 \text{ MPa/kg}\cdot\text{m}^3$, and an ultrahigh energy absorption per unit volume of 4.0 MJ/m^3 , coupled with nearly complete recovery after compression under strains exceeding 50%. This study overcomes the traditional strength-recoverability trade-off, showing the superiority of multiphase material design. Architected lattices with multicore-shell was 3D printed using novel 3D printing technique [57], and a high stiffness

and toughness were achieved. Other lattice-based architected material studies also demonstrated that the multimaterial design strategy can be leveraged to obtain significant enhancement of mechanical properties compared to single material design [58-60]. However, the above-mentioned investigations are mainly focused on the lattice structures due to the difficulties of fabrication of complicated 3D geometrical models. Recent advances in additive manufacturing such as multi-material and multiscale 3D printing have, however, enabled the production of bioinspired nacreous composites by emulating internal architectures and compositions [61-64]. Bio-inspired natural materials have offered great insights for designing architected engineering materials with fantastic material properties. For example, the hierarchical assembly of brittle minerals and soft proteins provides nacreous composites an unusual combination of stiffness, strength, damage tolerance, and impact resistance [65-68]. Similar microstructure designs with the synergistic interplay between hard brittle and soft organic layers have also been identified in glass sea sponges [69, 70], bones [71, 72], and teeth [73], which feature with remarkable mechanical properties. Meanwhile, biological materials inspired by wood and cork [74] exhibit superior mechanical properties while maintaining the characteristics of lightweight. Therefore, it is possible to tailor custom lightweight, high specific strength, and energy absorption characteristics by engineering the topology of cellular materials. Inspired by the cork structure, we propose multilayered cellular composites to enhance the mechanical properties.

Piezoelectric materials have been intensively used in various applications due to the unique piezoelectric effect. The conventional piezoelectric materials are limited by their poor sensing and mechanical performance. Enlighted by the multiphase cellular

composites, we apply this design strategy to piezoelectric materials. Piezoelectric composites have not been a new concept, it has been studied since last century [75]. As they discussed in the paper, connectivity is a critical parameter in composites designed for use as piezoelectric transducers or sensors. Totally 10 important connectivity patterns in diphasic solids, ranging from 0-0 unconnected checkboard pattern to 3-3 pattern where both phases are interpenetrating self-connected. However, the fabricating techniques at that time was quite limited, 3-3 connectivity composites can hardly be constructed. The advancement of 3D printing techniques today make it possible.

Piezoelectric composites, which can generate electric signals upon impacts by the piezoelectricity of its piezoelectric fillers and consume the imposed mechanical energy by the viscoelasticity of its polymeric matrix, have been considered as a desired candidate for the advanced multifunctional materials. However, the performance of conventional 0–3 and 1–3 hybrid piezoelectric composites is restricted by the random distribution of the spatial discontinuous particles and fibers, respectively, which renders poor stress transfer efficiency from the surrounding polymeric matrix to the active piezoelectric fillers [76, 77]. As a result, the energy-absorbing capability and piezoelectric response of these piezoelectric composites are quite limited. A proper combination of the two disparate constitutive materials will enable the design of multifunctional composites with exceptional energy dissipation behavior, considerable mechanical flexibility, and high piezoelectrical sensitivity simultaneously. Recent studies indicate that introducing bi-continuous architectures to composite materials is an alternative way that can fulfill the multifunctional need [55, 78, 79]. For instance, M. Yan [78] and our coworkers [79] have demonstrated that the bi-continuous architected piezoceramic-polymer composite can

render highly effective load transfer, resulting in significantly improved piezoelectricity, while M. Zhang [55] has provided a multi-design strategy to enhance the damping capacities in metals by developing a bi-continuous interpenetrating-phase architected Mg–NiTi composite. Furthermore, it has been reported that the aligned microstructure can improve the electric poling of structured piezoelectric materials [80], and architected composite structures have long been a subject of great interest towards the development of improved impact and vibration protection systems [81]. However, there still lacks research to simultaneously enhance piezoelectricity and damping capacities. To implement this multifunctional need and achieve a good combination of damping and piezoelectricity, H. Cui and co-workers [82] surface-functionalized the piezoelectric nanoparticles with ultraviolet sensitive monomers and used the 3D printing method to sculpt the functionalized piezoelectric nanoparticles into designed 3D structures. However, this method needs complex functionalization processes and a high-resolution additive manufacturing system, which hinder its large-scale practical applications. In this work, in order to solve the challenges, we use a facial camphene templated freeze-casting method to fabricate the 3-3 connectivity piezoelectric composites. Combining experimental characterization and numerical simulation, we will study the multifunctionalities of the proposed composites.

1.2.4 Topology optimization of multifunctional composites

Architected materials have demonstrated their capabilities in achieving unprecedented mechanical properties and functionalities. However, how to optimally control the porosity distribution and material layouts become crucial in designing the architected materials. Conventionally, experiment-based trial and error, intuition-driven, and experience-driven

design approaches are used for attaining the optimized design. These methods have been proved to be expensive and inefficient. Topology optimization, on the other hand, is capable of effectively navigating the rapidly expanding design space. Intrinsically, formal mathematical programming coupled with physics modeling is used to drive the design decisions, and thus exploration proceeds in a systematic manner toward (locally) optimal designs. This mathematically driven nature makes topology optimization a powerful alternative to alter structure connectivity has produced a number of compelling examples of high-performance, non-intuitive devices and components, from compliant mechanism inverters [83] to multiphysics actuators [84], cellular composites with negative Poisson's ratio, and lattice metamaterials with wave attenuation properties.

Up to now, there have been several topology optimization frameworks developed to solve the structural optimization problem. One main approach to structural design for variable topologies is the method of homogenization [85-87], where a material model with microscale voids is introduced and the optimization problem is defined by finding the optimal porosity using one of the optimality criteria. By transforming the topology design problem into an easier 'sizing' problem, the homogenization technique is capable of producing internal holes without knowing their existence. However, homogenization approach is not without its drawbacks. In fact, most of the time, the homogenization method may not yield the intended results for some objectives in the modeling of structural design. It often yields the designs with infinitesimal pores in the materials which makes the structure not manufacturable. In addition, numerical instabilities could introduce 'non-physical' artifacts in results and make the designs sensitive to variations in the loading. In order to tackle these problems, different other techniques have been brought out. For

example, solid isotropic material with penalization (SIMP) is one of the approaches, which is conceptually simple [88-90]. In this method, material properties are assumed to be constant within each element used to discretize the design domain, and the design variables are element densities. This material properties are modeled to be proportional to the relative density raised to some power. The power-law-based method has been widely used to various problems with multiple constraints, multiple materials, and multiple physics. Another approach for topology optimization is called evolutionary structural optimization (ESO) [91]. This method is based on the concept of gradually removing the material to obtain an optimal design. The approach was developed for various problems of structural optimization including stress considerations, stiffness constraints, and frequency optimization, etc. The key process of this approach is to use proper criterion to assess the contribution of each element to the specific response of the structure and subsequently to remove some elements with the least contribution. Level set-based topology optimization is another method that has been intensively applied in designing structures. The concept of level set was initially proposed by Osher and Sethian [92]. The overall concept involves eliminating materials in regions where the stress is low and adding materials in regions where the stress is high. The advantages of this method can be summarized in three points [93]. First, it has the potential to concurrently deal with the complicated shape and topology change of structural boundaries. Second, the weak material is moved away in the finite element analysis, which avoids the occurrence of artificial localized modes. Third, structural can be formulated as the solution to Hamilton-Jacobi equation with relation to shape derivative of the boundaries.

In this work, we use the solid isotropic material with penalization (SIMP) topology optimization method to optimize the piezoelectric composites due to the easier implementation. We will use the adjoint method to derive the sensitivity analysis of the objective function. For simplicity, we assume the linear elastic behavior of the material properties.

Overall, the research objective of this thesis is to achieve enhanced mechanical performance and multifunctionalities using architected metamaterials by integrative numerical and experimental approaches. We first propose architected hollow sphere foam structure and demonstrate the effectiveness of noise and vibration control with superior mechanical performance. We then present multi-phase composites with exceptional energy absorption and multifunctionality. Finally, a topology optimization framework is proposed to optimize the composite structure with optimum performance of energy absorption and sensing.

CHAPTER 2

MATERIALS AND METHODS

2.1 Periodic structures and wave propagation

A periodic structure is defined as an assembly of objects that repeat regularly in space. Depending on its repeating directions, we have one-dimensional (1D), two-dimensional (2D), and three-dimensional (3D) periodic structures. To demonstrate the periodic feature of the periodic structure, we will use a two-dimensional periodic structure as an example. Figure 2 (a) shows a representative 2D periodic lattice structure, which extends infinitely in the 2D plane. It is noticeable that the point lattice is equivalent to the repeated objects. We can use the two lattice vectors (\mathbf{a}_1 , \mathbf{a}_2) along with a lattice angle to uniquely define the periodic structure:

$$\mathbf{R} = n_1 \mathbf{a}_1 + n_2 \mathbf{a}_2 \quad (2.1)$$

where n_1 and n_2 are arbitrary integer numbers. Depending on the structural periodicity, there are five types of two-dimensional point lattices, i.e., oblique, rectangular, square, triangular, and rhombus. A similar procedure can be applied to 1D and 3D periodic structures.

To study wave propagation in periodic structures, it is necessary to find the relation between wave vectors and their corresponding eigenfrequencies, which is called a phononic dispersion relation. The most fundamental property of phononic dispersion

relation is the existence of complete wave band gaps: frequency range where wave propagation is suppressed. To do this, we need to find the wave vectors associated with the periodic structure that can completely describe the wave propagation. When the plane wave propagating in periodic structures, there are certain wave vectors that satisfying the periodicity of the point lattice. As a result, we have

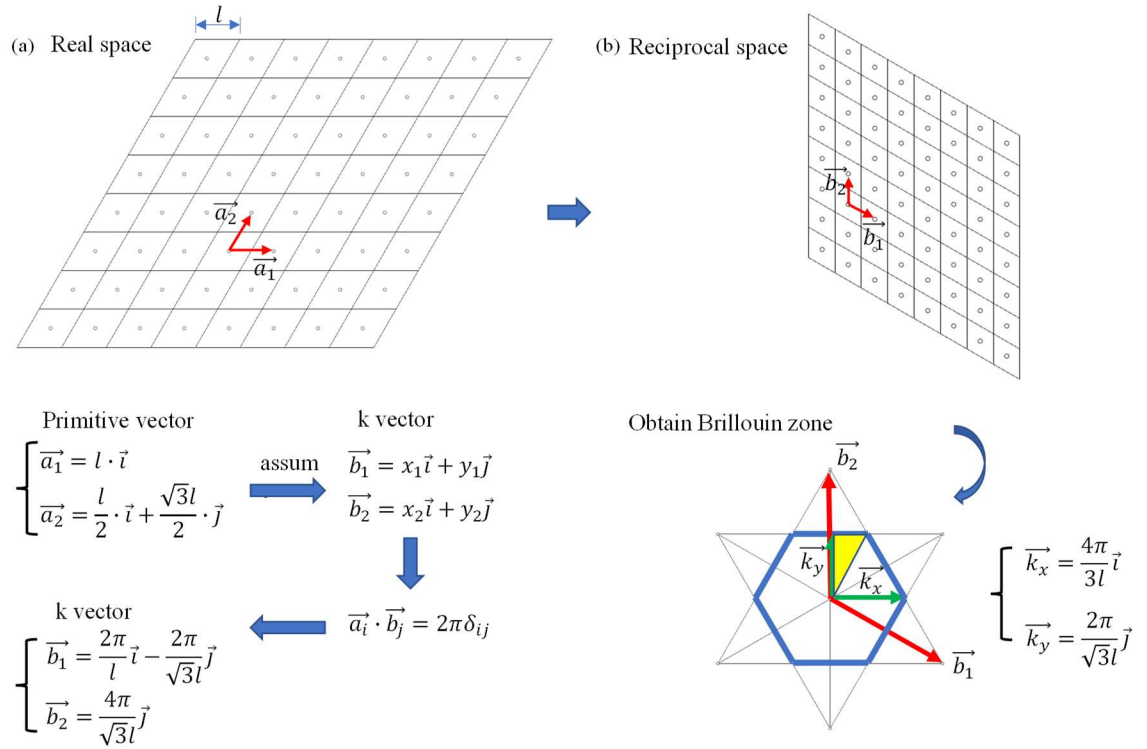


Figure 2 Schematic of a two-dimensional periodic lattice structure (a) point lattice in real space (b) reciprocal lattice in k-space

$$e^{i\mathbf{k} \cdot \mathbf{r}} = e^{i\mathbf{k} \cdot (\mathbf{r} + \mathbf{R})} \quad (2.2)$$

By combining Eq. (2.2) with Eq. (2.1), we can calculate the wave vector, \mathbf{k} , as shown in Figure 2. By connecting the midpoints of the reciprocal lattices, we have a highly symmetric yellow area, which is called irreducible Brillouin zone.

2.2 Finite element simulations

In chapter 3, Finite element simulations were conducted to understand the wave propagation behavior of architected foam structures. For the acoustic wave simulation, the governing equations can be expressed as the frequency-domain Helmholtz equation:

$$\nabla \cdot \left(\frac{\nabla p}{\rho} \right) + \frac{\omega^2}{\rho c_l^2} p = 0 \quad (3-1)$$

where p is the pressure, ρ is the mass density, ω is the angular frequency, and c_l is the speed of sound. We assume that the architected foam is infinite and periodic in x , y , and z directions. Numerical simulations are conducted on a unit cell with Floquet-Bloch periodic boundary condition to capture the infinite periodic nature of the 3D architected foams. The Floquet-Bloch periodic boundary condition is applied to the unit cell along three directions, respectively and can be expressed as

$$\begin{aligned} p(x + a_1, y, z) &= p(x, y, z) \exp(ik_1 a_1) \\ p(x, y + a_2, z) &= p(x, y, z) \exp(ik_2 a_2) \\ p(x, y, z + a_3) &= p(x, y, z) \exp(ik_3 a_3) \end{aligned} \quad (3-2)$$

where a_1 , a_2 and a_3 are lattice constants along x , y , and z directions, respectively. k_1 , k_2 and k_3 are the Bloch wave vectors. The governing equation (3-1) combining with the boundary condition (3-2), leads to the standard eigenvalue problem:

$$(\mathbf{K} - \omega^2 \mathbf{M}) p = 0 \quad (3-3)$$

where \mathbf{K} and \mathbf{M} are assembled stiffness matrix and mass matrix of the unit cell, respectively. The unit cell is discretized using ten-node tetrahedron elements. In the

simulations, we have used a discretization of ten elements for the minimum wave-length. Equation (3-3) is then numerically solved by imposing the three components of the wave vectors and hence calculates the corresponding eigenfrequencies. The acoustic dispersion relations are obtained by scanning the wave vectors in the first irreducible Brillouin zone, as introduced in the section 2.1.

The governing equation of elastic wave propagating in the 3D architected foam is given by

$$-\rho\omega^2\mathbf{u} = \frac{E}{2(1+\nu)}\nabla^2\mathbf{u} + \frac{E}{2(1+\nu)(1-2\nu)}\nabla(\nabla\cdot\mathbf{u}) \quad (3-4)$$

where \mathbf{u} is the displacement vector and ω is the angular frequency. E , ν , and ρ are Young's modulus, the Poisson's ratio, and the density of the constituent materials, respectively. By following a similar procedure as acoustic wave dispersion relation analysis, we can construct the elastic wave dispersion relations for the 3D architected foams by applying Floquet-Bloch periodic boundary conditions and scanning the wave vectors along the first irreducible zone. For both acoustic and elastic wave simulations, we choose a glassy polymer (Nylon 12) as the solid phase with a modulus of 1.6 GPa, Poisson's ratio of 0.33, and a density of 1174 kg/m³. The transverse and longitudinal wave velocities of this polymer are 715.79 m/s and 1421.01 m/s, respectively, while the longitudinal velocity and density of air are 343 m/s and 1.2 kg/m³, respectively.

In chapter 4, we use simplified elastic-plastic model to simulate the Nylon-12 material. The constitutive model for the 3D printed Nylon material was characterized by uniaxial tensile tests of three dogbone samples. The test was performed according to the ASTM D638 standard. The measured stress-strain relation is shown in Figure 3. Here, nominal stress

and nominal strain were calculated by Eq. (2.3) and (2.4), respectively. True stress and true strain were calculated by Eq. (2.5) and (2.6), respectively.

$$\sigma_0 = F/A_0 \quad (2.3)$$

$$\varepsilon_0 = \delta/L_0 \quad (2.4)$$

$$\sigma_T = \sigma_0 (1 + \varepsilon_0) \quad (2.5)$$

$$\varepsilon_T = \ln(1 + \varepsilon_0) \quad (2.6)$$

where σ_0 and ε_0 represent the nominal stress and nominal strain. F , A_0 , δ , and L_0 are the load, original cross-section area, displacement, and original length of the sample, respectively. σ_T and ε_T denote true stress and true strain. The Young's modulus was extracted as the average slope of the stress-strain curves. The average slope of the stress-strain curves mean the average of three repeated tests for the first slope in Figure 3 (b).

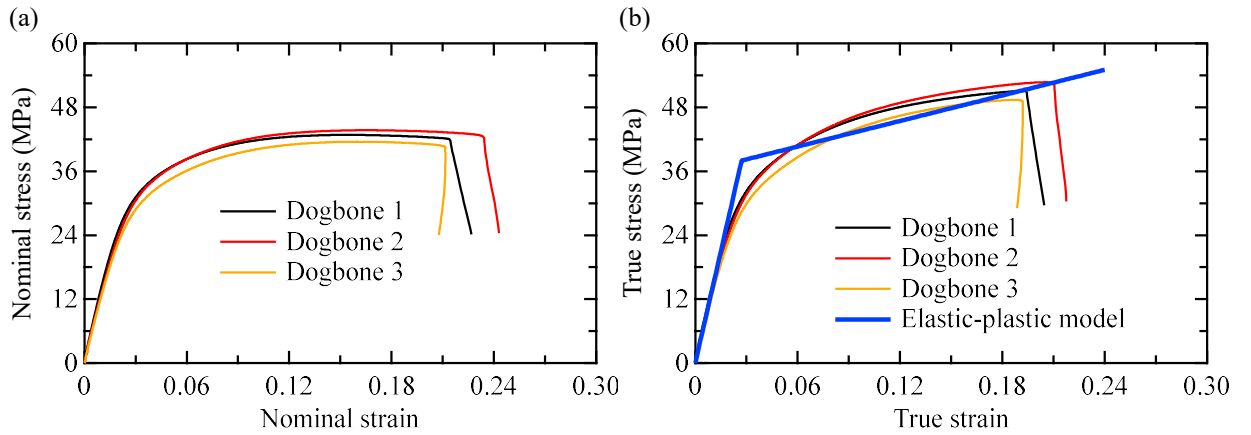


Figure 3 Stress-strain relation from experimental data (a) Nominal stress vs. nominal strain of three dogbone samples. (b) True stress vs. true strain of three dogbone samples and the fitted elastic-plastic model.

In chapter 5, for the VeroWhitePlus polymer material, a user-defined viscoplastic constitutive model was first developed to simulate the response of the 3D printed polymer in [94], where the detailed description of implementation was given. In addition, reference also adopted this model and made it publicly available. In this paper, we referred to for this constitutive model. The strain energy potential for the Arruda-Boyce model is [95]

$$W = \mu \left\{ \frac{1}{2}(\bar{I}_1 - 3) + \frac{1}{20\lambda_L^2}(\bar{I}_1^2 - 9) + \frac{11}{1050\lambda_L^4}(\bar{I}_1^3 - 27) + \frac{19}{7000\lambda_L^6}(\bar{I}_1^4 - 81) + \frac{519}{673750\lambda_L^8}(\bar{I}_1^5 - 243) + \frac{K_0}{2} \left(\frac{J_e^2 - 1}{2} - \ln J_e \right) \right\} \quad (2.7)$$

where μ is the initial shear modulus, λ_L is the limiting network stretch, K_0 is the initial bulk modulus, J_e is the elastic volume ratio related to temperature. \bar{I}_1 is defined as

$$\bar{I}_1 = I_1 J^{-2/3} \quad (2.8)$$

$$I_1 = \text{trace}(\mathbf{B}) = B_{11} + B_{22} + B_{33} \quad (2.9)$$

where \mathbf{B} is left Cauchy-Green deformation tensor. The total volumetric ratio can be described as

$$J = \sqrt{\det(\mathbf{B})} \quad (2.10)$$

If thermal effect is not considered, $J_e = J$.

The effective shear strain rate can be determined through equation [95]

$$\dot{\gamma}^p = \gamma_0 \exp \left[-\frac{\Delta G}{\kappa \Theta} \left(1 - \left(\frac{\sigma_e}{s} \right)^{5/6} \right) \right] \quad (2.11)$$

where γ_0 is the pre-exponential shear strain rate, s is the thermal shear yield strength, κ is the Boltzmann's constant, σ_e is the effective stress, ΔG is the initial free energy change.

The rate of shear yield strength for strain-softening is determined through [95]

$$\dot{s} = h \left(1 - \frac{s}{s_s} \right) \dot{\gamma}^p \quad (2.12)$$

where s_s is s at steady state, h is the slope of strain-softening zone.

2.3 3D printing of architected metamaterials

In chapter 3 and 4, we use the HP jet fusion 580 printer (HP Inc., USA) for fabricating. HP jet fusion 580 printer is featured with the unique multi-agent and multi-pass printing process. The resolution of this printer is $80 \mu m$. Nylon-12 (Polyamide-12) polymers were used as the base material. Nylon-12 is a semi-crystalline polymer with superior properties, such as good processability, high mechanical property at moderate temperatures [96], and low costs. Nylon-12 has long been used by injection molders and more recently has been adopted as base material in additive manufacturing for fabricating functional parts and prototypes. The Nylon-12 powder melting point is $189^\circ C$, and the particle size is $58 \mu m$. The Nylon-12 powder exhibits initial viscosity of $660 Pa \cdot s$ at $190^\circ C$ and increases to $800 Pa \cdot s$ within 10 min. This commercial HP printer adopts Multi Jet Fusion technology, also known as MJF. It utilizes two carriages to transform powdered Nylon-12 into solid parts. The process parameters are set as follows, Printing Profile: Mono Balanced; Cooling Profile: Auto Cool and Reclaim; Annealing Profile: Auto; Fresh Percentage Mix Ratio: 20 %. Initially, the material is spread evenly across the build platform, then a carriage with HP thermal inkjet array passes over the working area, printing fusing, detailing, and

coloring agents on the material. During another pass of the carriage, this working area is exposed to the thermal fusing energy, which bonds the part layers together. Unlike other 3D printing technologies, the new materials and agents are printed on top of a previous layer that is still molten. Therefore, these two layers can fuse completely, and polymers can lock in with each other across the layer boundary, making high-quality products.

In chapter 5, we use Objet260 Connex3 printer (Stratasys Ltd., USA) to fabricate our samples, which is a high-resolution multi-material color 3D printer with a resolution of 16 . VeroWhitePlus (VW+) is used as the base material. VW+ Resin is a material used to create 3D printed objects from a base of photosensitive polymer liquid. VW+ Resin enables the printer to create objects which are particularly smooth and precise. Compared with standard engineering plastics, such as standard ABS thermoplastic, VW+ is stronger and stiffer. Therefore, the VW+ material is generally designated for functional testing, patterns, prototypes, and models. During the printing process, the liquid photopolymer resin is ejected onto the printer tray from the printer head orifices, and then immediately cured by UV light. Once a layer is cured, the following layer repeats the same process. This layer-by-layer fabrication mode enables high-quality products. When the printing process was complete, samples were carefully moved to the WaterJet (Stratasys, USA) machine to remove the supporting material.

2.4 Mechanical testing

All the architected polymer foam samples are uniaxially compressed by an Instron universal testing machine (5569A, Instron, USA). The compressive extension rate was set to 3.75 mm/min, corresponding to the compressive strain rate of $5 \times 10^{-4} / s$. The specimens

are loaded to 70 % strain. Prior to the testing, 2D Digital Image Correlation (GOM, Germany) equipment is installed to capture deformation patterns and failure modes.

CHAPTER 3

3D ARCHITECTED HOLLOW SPHERE FOAMS FOR NOISE AND VIBRATION CONTROL

3.1 Introduction

Noise and vibration, arising from construction such as pile driving and blasting, ground transportation, airplane engines, and fluid flow, are not only an annoyance, but also have adverse health, social, and economic impacts. To mitigate the undesired noise and vibration, active control and passive control approaches have been widely adopted and remained the same for decades [97]. Though these approaches are effective under certain circumstances, they still suffer from some drawbacks. For example, the attenuation frequency range is relatively narrow in the active control, limiting its potential applications in complex noise and vibrational environments. For passive control, there is a conflict between the wave energy absorption and structural weight as well as mechanical robustness. As such, conventional approaches have resulted in suboptimal control of noise and vibration. Moving towards architected metamaterials, which are rationally designed multiscale material systems, exhibit novel functionalities and unique properties that cannot be readily achieved in natural bulk solids. One example of such architected metamaterials is phononic metamaterial, which consists of periodically topological structures and materials dispersions.

Here we choose architected hollow sphere foams (AHSFs) as the model system to address the above challenge. In the past decades, hollow sphere foams (HSFs) have been investigated intensively, because of their exceptional mechanical, thermal, and acoustic properties. For example, earlier finite element simulations have revealed that architected hollow sphere metallic foams with a face-centered cubic lattice symmetry exhibit the highest moduli and yield strength when compared with foams with other lattice symmetries [43, 98]. In addition, anisotropic feature and considerable fatigue resistance of HSFs have been reported [99, 100]. Under large deformation, HSFs show good energy absorption characteristic, which is controlled by loading rate, geometric parameters, and topologies [101]. These prominent mechanical properties make hollow sphere foams ideal candidate for automotive applications where lightweight design and enhanced mechanical properties are simultaneously pursued. In addition to these mechanical properties, theoretical models along with finite elements simulations indicate that architected hollow sphere foams can be designed with low thermal conductivity by tailoring the packing fraction, shell, and binder geometry [44]. In parallel, it has been demonstrated that both random and rationally designed HSFs can manipulate mechanical wave propagation. For instance, perforated HSFs with wide acoustic attenuation ranges show great promise to serve as acoustic liners for airplane engines [41]. Our recent numerical work further demonstrates that perforated AHSFs can simultaneously control sound and elastic wave propagation [42]. In addition to these multifunctionalities, HSFs offer manufacturing flexibility in material selection and can be assembled into relatively defect-free periodic structures [43, 44], making them ideal for use in multiple fields of application. Because of the multifunctionalities, versatile design space, and manufacturing flexibility, AHSFs offer an ideal model system to

investigate how to achieve lightweight phononic metamaterials with low-frequency vibration mitigation.

3.2 Model description

In this work, we designed and fabricated AHSFs composed of hollow spheres connected by binders with a body-centered-cubic (BCC) lattice symmetry (Figure 4(a)). The unit cell for Bloch wave propagation analysis and detailed geometric description of each component can be found in Figure 4(b) and (c). We demonstrate both experimentally and numerically the existence of phononic band gaps in the proposed AHSFs. Numerical simulations indicate that the band gap properties are controlled by the geometric features of the hollow sphere and binder. Remarkably, phononic band gap can be altered to a low-frequency range by tailoring the stiffness contrast between the hollow sphere and binder. In addition to the AHSF with a BCC lattice symmetry, we will show that the elastic wave phenomena persist in AHSFs with other topologies.

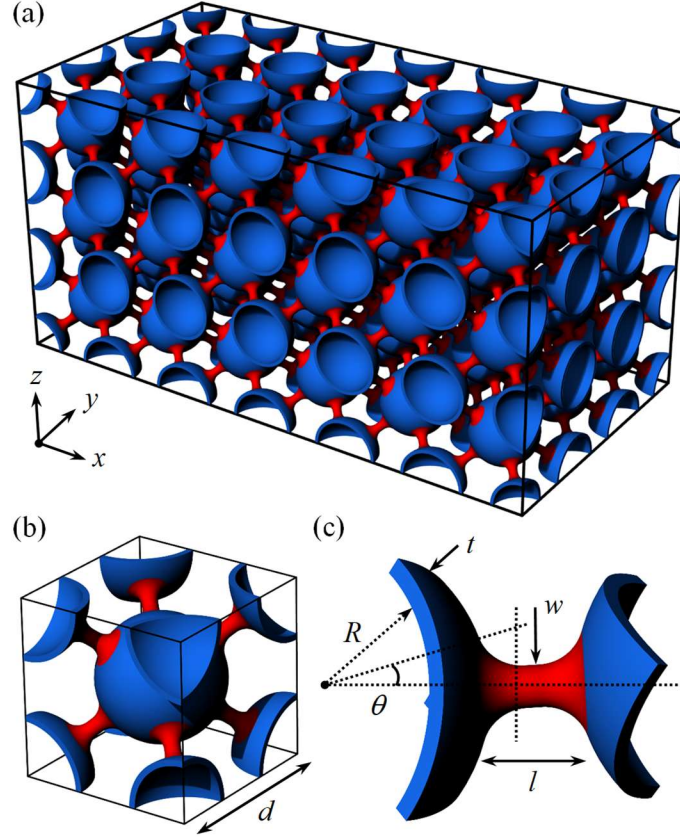


Figure 4 Geometric description of the proposed architected hollow sphere foam (AHSF) with a body-centered-cubic (BCC) lattice symmetry (a) AHSF consists of spheres (blue) and binders (red). (b) The unit cell of the AHSF for Bloch wave analysis. The lattice constant is d . (c) Dimensions of the hollow sphere and binder. Here R and t are the sphere's outer radius and thickness, respectively. l and w are the binder's length and diameter, respectively. θ is half of the angle subtended by the binder.

3.3 Numerical model validation with experiment

We start by focusing on the existence of phononic band gaps in the proposed AHSFs through a combined experimental and numerical effort. For our simulations and experiment, the lattice constant of the unit cell is 3 cm and the volume fraction of the sample is 10.8%. The lattice constant is determined by the operating frequency range of the dynamic signal

analyzer and the maximum build volume of our 3D printer. To avoid unsintered powder to be encapsulated inside the hollow spheres, AHSF model composed of $6 \times 3 \times 3$ unit cells was cut into six equivalent layers and fabricated by using an HP Jet Fusion 3D 4200 printer (Figure 5(a)). Then, the six layers were glued together using glue gel, and the assembled sample was kept at room temperature for seven days to allow for the saturation of the curing. The mechanical properties of the constitutive material Nylon PA12 were measured by following ASTM D695. The basic properties of Nylon PA12 are characterized by Young's modulus $E = 1.312 \text{ GPa}$, Poisson's ratio $\nu = 0.33$, and density of $\rho = 979 \text{ kg/m}^3$.

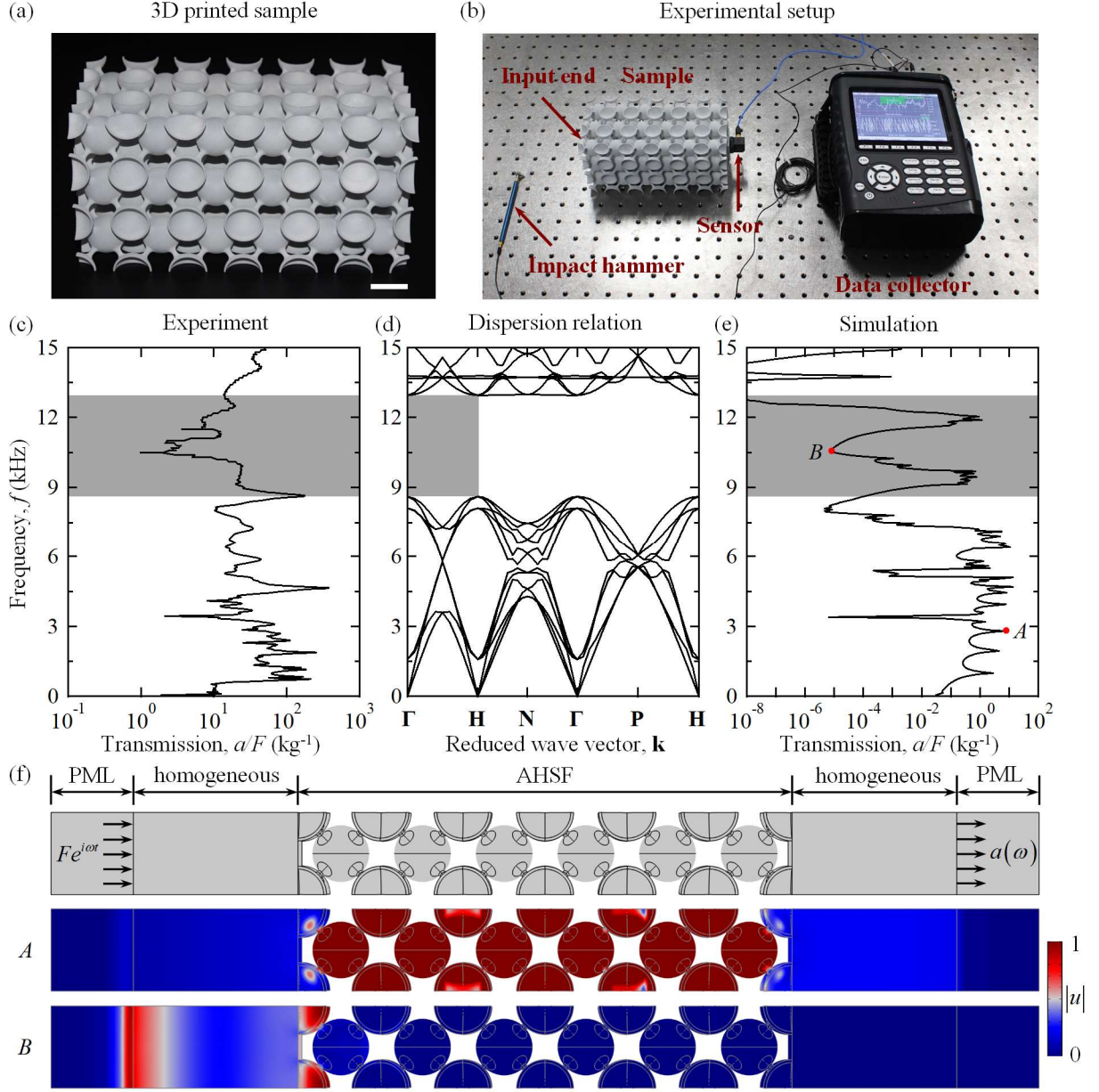


Figure 5 Elastic wave transmission test on the 3D printed AHSF and numerical modeling validation (a) 3D printed AHSF composed of $6 \times 3 \times 3$ unit cells for elastic wave transmission test. Here $d = 3$ cm, $R = \sqrt{3}/5d$, $R/t = 10$, $l/w = 2$ and $\theta = 18^\circ$. Scale bar: 2 cm. (b) Experimental setup for elastic wave propagation test. (c) Measured elastic wave transmission spectra along ΓH (x) direction. (d) Simulated phononic dispersion relation. (e) Simulated wave transmission spectrum. The gray shaded areas in (c)-(e) indicate the band

gaps. (f) Finite element model and dynamic responses of the AHSF under excitation frequencies outside (point A: $f = 2.8$ kHz) and inside (point B: $f = 10.6$ kHz) the band gap. The color legend represents total displacement amplitude.

To confirm the experimentally observed attenuation zone, we performed numerical simulations on the single unit cell and the finite size AHSF with $6 \times 1 \times 1$ unit cells using a commercial finite element package, COMSOL MULTIPHYSICS. Floquet-Bloch periodic boundary conditions introduced in CHAPTER 2 are applied in COMSOL. The phononic dispersion relation is constructed by performing eigenfrequency analyses to a unit cell. The unit cell is discretized using 4-node tetrahedral elements, which are one-tenth of the minimum wavelength. The dynamic response of the proposed AHSF under elastic wave excitations is calculated by performing frequency domain analyses. Perfectly matched layers (PMLs) are applied at the two ends of the homogeneous parts to prevent reflections by scattering waves from the domain boundaries. Figure 5(d) and (e) report the simulated phononic dispersion relation and transmission spectrum, respectively. Notably, we have a good qualitative agreement for the partial band gap between the simulations and experiments (highlighted in gray). The dynamic responses of the AHSF under harmonic excitation frequencies inside and outside the band gap further solidify this phenomenon (Figure 5(f)). When the incident frequency lies outside the band gap (point A), elastic wave can propagate freely through the AHSF. By contrast, the incident wave energy will be reflected when the incident wave frequency is located inside the band gap (point B).

3.4 Design flexibility of phononic band gaps

3.4.1 Effect of geometric parameters

We then numerically investigate the effects of architected foam geometric features on the evolution of the first phononic band gap. The unique design of architected foams allows us to study the roles of the hollow sphere and binder independently. The mechanical properties of the constitutive material are defined by Young's modulus $E = 1.6\text{GPa}$, Poisson's ratio $\nu = 0.33$, and density of $\rho = 1174\text{kg/m}^3$ unless otherwise specified. As shown in Figure 6(a), by increasing the fillet angle of binder, the relative size of the omnidirectional band gap decreases gradually. The relative band gap size was changed from 0.68 to 0.31 when the fillet angle is doubled from 10° to 20° . By contrast, the binder slenderness ratio has a pronounced impact on the band gap properties. For a wide binder ($l/w = 2$) representing a strong connection between binders and hollow spheres, the first omnidirectional band gap has a relatively small size of 0.1. When the binders become slender ($l/w = 10$) corresponding to a soft connection, the band gap size increases to 1.47, which is one order of magnitude larger (Figure 6(b)). To further understand these trends, one can assume that the proposed AHSF behaves as a 3D mass-spring system, where hollow spheres act as lumped masses and binders work as springs. Each mass is accompanied by its eight nearest neighbors and connected by the spring. Analytical formulations reveal that the first omnidirectional phononic band gap results from oscillation and interaction among these masses [102-104] and thus the opening of the first band gaps are controlled by the geometric features of the binders and hollow spheres. To confirm this, Figure 6(c) shows the effect of hollow sphere thickness and thus the mass on the band gap properties. As expected, by increasing the sphere thickness and thus the

lumped mass of the system, a larger omnidirectional band gap can be observed. These parametric analyses not only demonstrate the design flexibility of the proposed AHSFs with targeted phononic band gaps, but also imply that a weak connection among hollow spheres can lead to large band gap size in a low-frequency range.

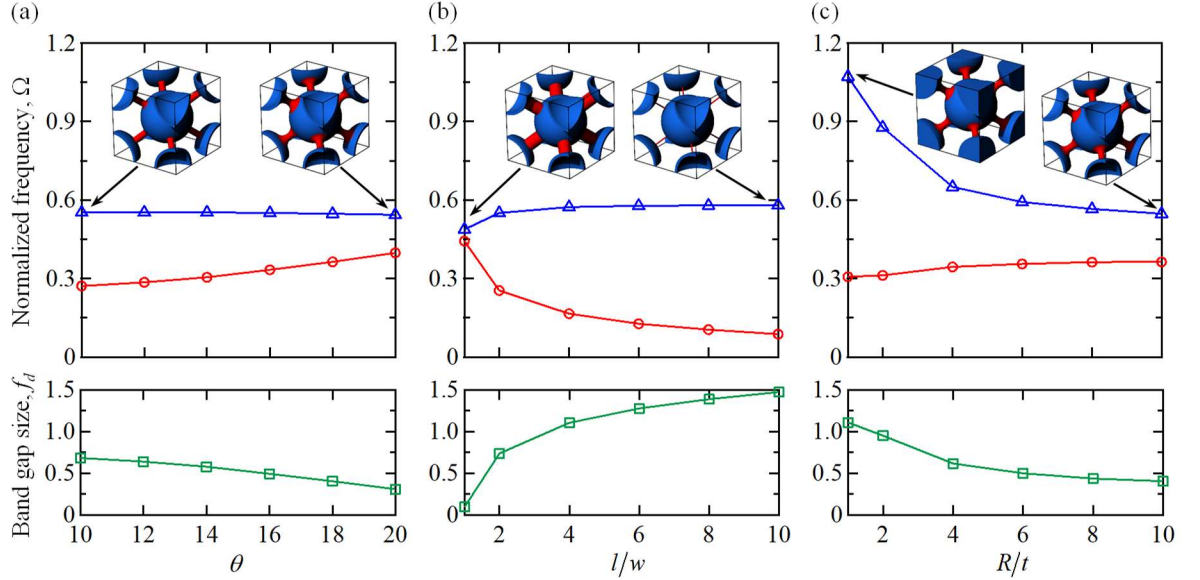


Figure 6 Effects of binder and hollow sphere geometric features on the phononic band gap properties (a) Effect of binder fillet angle. Here $d = 3$ cm, $R = \sqrt{3}/5d$, $R/t = 10$, and $l/w = 2$. (b) Effect of binder slenderness ratio. Here $d = 3$ cm, $R = \sqrt{3}/5d$, $R/t = 10$, and $\theta = 18^\circ$. (c) Effect of hollow sphere thickness. Here $d = 3$ cm, $R = \sqrt{3}/5d$, $l/w = 2$, and $\theta = 18^\circ$. The normalized frequency is defined as $\Omega = fd/c_t$, where c_t is the transverse velocity of the solid phase. The omnidirectional band gap size (green squares \square) is defined as $f_d = 2(f_u - f_l)/(f_u + f_l)$, where f_u and f_l present the frequencies of upper (blue triangles Δ) and lower (red circles \circ) band edge limits of the omnidirectional band gap, respectively.

3.4.2 Effect of stiffness contrast

We have shown the targeted phononic band gaps can be achieved by tailoring the geometric parameters of the AHSFs. Next, we fix the geometric parameters of the AHSFs and change the stiffness contrast between spheres and binders (E_s/E_b) to study the effect of this contrast on the band gaps. Here we choose $d = 3$ cm, $R = \sqrt{3}/5d$, $R/t = 10$, $l/w = 2$ and $\theta = 18^\circ$. As displayed in Figure 6, the first omnidirectional band gap is enlarged from $\Omega = 0.36 \sim 0.55$ to $\Omega = 0.18 \sim 0.53$ when the binder stiffness varies from one to one-tenth that of the sphere. By further decreasing the stiffness of the binders, the first band gap rapidly shifts toward a much lower frequency range. For example, when the stiffness ratio is $E_s/E_b = 1000$, the frequency range of the band gap decreases to $\Omega = 0.02 \sim 0.094$. To gain physical insights into this trend, we plot the eigenmodes at high symmetry points of the band edges, as shown in Figure 7. The initial AHSF with a single constitutive material shows a Bragg type band gap because of the global vibration modes at the band edges (Figure 7(a)-(b)). With the increase of stiffness contrast, the vibration modes demonstrate a strong localized characteristic. For example, as one can see in Figure 7(c) and (d), the vibrational energy is localized in the hollow spheres at the upper band edges; at the lower band edges, the wave energy is concentrated on the soft binders. Essentially, these eigenmodes analyses suggest that by tailoring the stiffness contrast between components, the band gap formation mechanisms can be switched from Bragg scattering to local resonance.

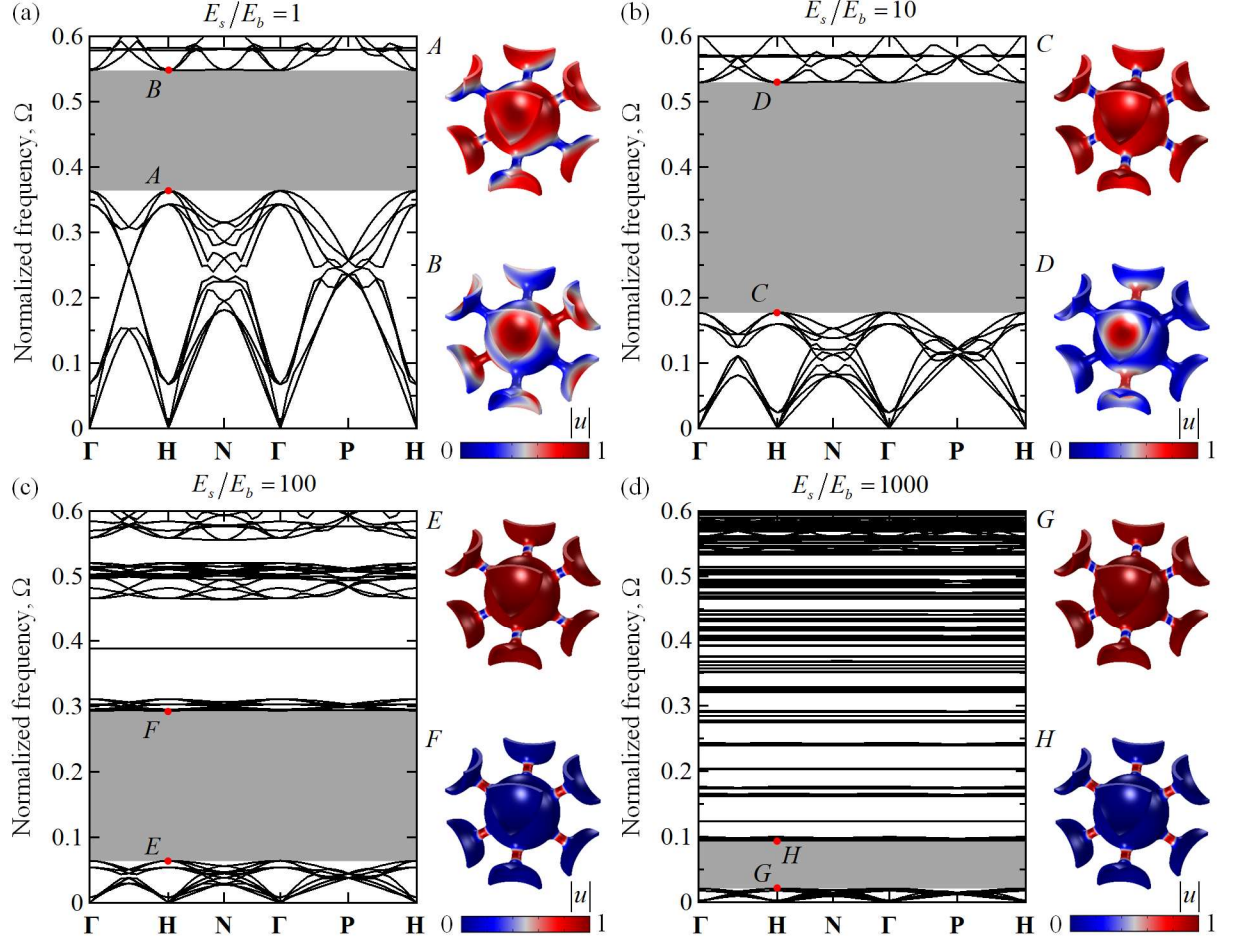


Figure 7 Effect of stiffness contrasts between spheres and binders on phononic dispersion relations of the AHSF with a BCC lattice symmetry (a) $E_s/E_b = 1$, (b) $E_s/E_b = 10$, (c) $E_s/E_b = 100$, and (d) $E_s/E_b = 1000$. Here $d = 3$ cm, $R = \sqrt{3}/5d$, $R/t = 10$, $l/w = 2$ and $\theta = 18^\circ$. The gray shaded areas in the dispersion relations represent the first omnidirectional band gaps. The contour plots are eigenmodes at high symmetry points of the first irreducible Brillouin zone.

A more detailed analysis of the effect of stiffness contrast on the first band gap properties is summarized in Figure 8. The band gap is abruptly shifted toward low-frequency range with the increase of stiffness ratio, while the relative band gap size

increases linearly until a critical value is reached. At this threshold, the stiffness contrast is 50. Compared with conventional approaches such as harnessing structural instability to tune band gap properties [105, 106], the proposed approach does not need to change the architectures by applying external stimuli. Importantly, compared with existing 3D phononic crystals [102, 103, 107, 108], the proposed AHSF only requires a volume fraction of 10.8% while exhibiting a comparable band gap size exceeding 130%. This remarkable low-frequency band gap feature along with the lightweight design offers a promising approach for low-frequency vibration control, such as ground transportation induced vibrations and low amplitude seismic waves [109, 110]. In addition to choose different constitutive materials, the stiffness contrast can be accomplished by using active materials, such as shape memory polymers [111], shape memory alloys [112], and magnetic elastomers [113, 114]. As demonstrated by recent experimental work, the stiffness of 3D printed shape memory polymer can be tuned over three orders of magnitude by resistance wire heating [115]. For our case, by wrapping the binders with designed resistance wire, one can tune the binder stiffness and hence achieve tunable low-frequency band gaps, as predicted by our numerical simulations.

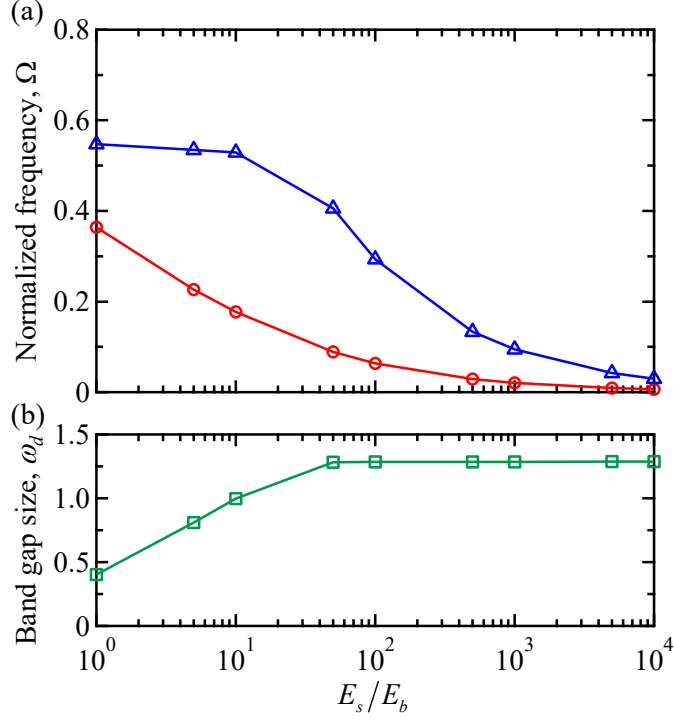


Figure 8 Effect of stiffness contrast on the first phononic band gap properties. (a) Omnidirectional band gap position (a) Omnidirectional band gap position. (b) The relative band gap size of omnidirectional band gaps. For the definition of normalized frequency and band gap size, please refer to the caption of Figure 6 for explanation.

3.4.3 Effect of lattice symmetry

The elastic wave propagation results reported so far are focused on AHSFs with a BCC lattice symmetry. We now proceed to examine the effect of lattice symmetry on the band gap properties. Figure 9 reports the phononic dispersion relations of AHSFs with a simple cubic (SC) and a face-centered-cubic (FCC) lattice symmetry. For the AHSF with an SC lattice symmetry, an omnidirectional band gap is observed in $\Omega = 0.28 \sim 0.47$, which is shifted to $\Omega = 0.05 \sim 0.25$ when the stiffness contrast increases to 100. Notably, the relative band gap size is enlarged from 0.52 to 1.36. Similar evolution trend of the first band gap

can be observed in the dispersion relations of the AHSF with an FCC lattice symmetry. The relative band gap size is increased from 0.22 to 1.23. Physically, the global vibration modes of the initial AHSFs with SC and FCC lattice symmetries indicate Bragg type band gaps, while the localized deformation patterns in AHSFs with a high stiffness contrast suggest locally resonant band gaps. These results imply that the proposed design strategy and physical mechanisms are robust and can be extended to architected foams with other topologies.

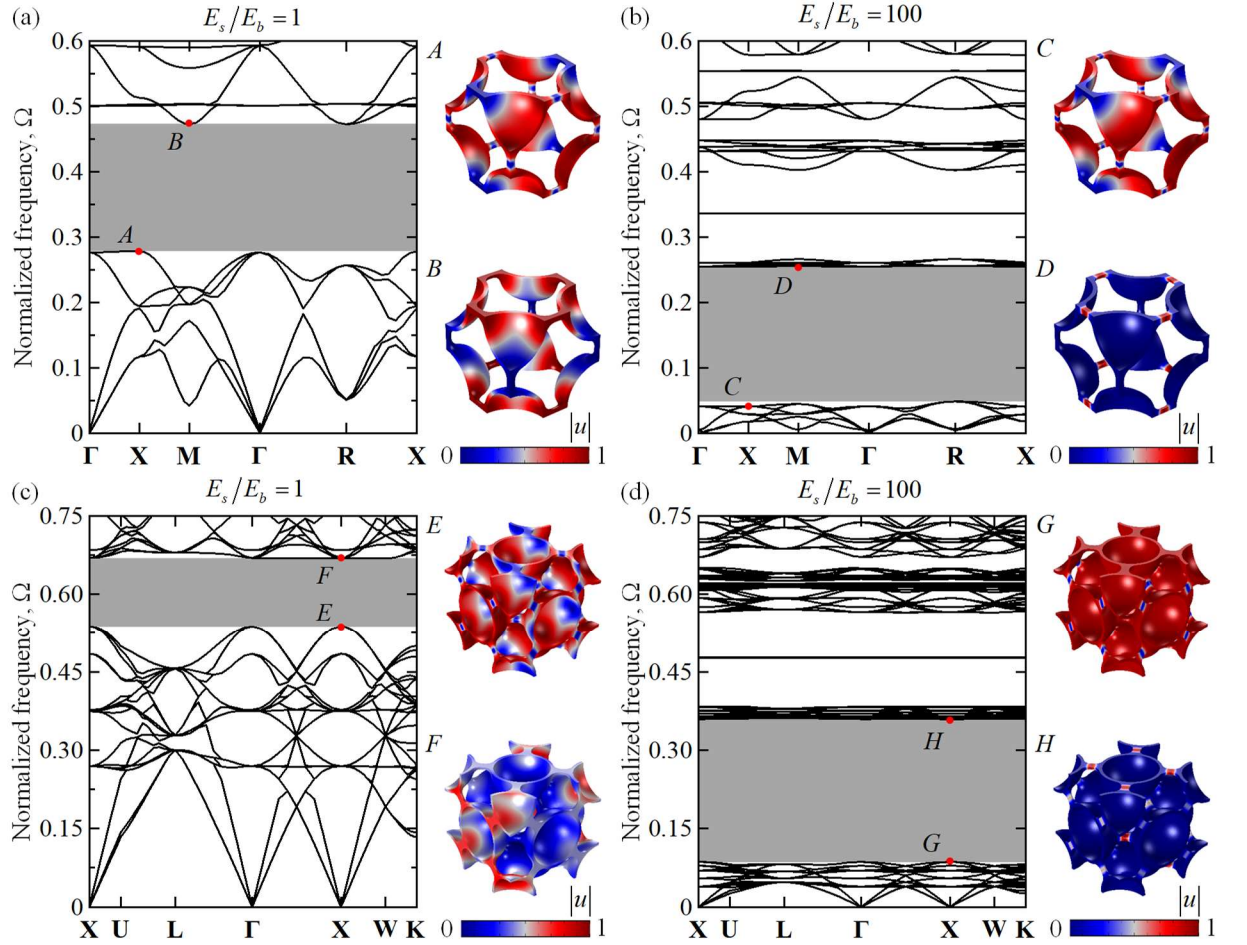


Figure 9 Effect of lattice symmetry and stiffness contrast on phononic dispersion relations

(a)-(b) AHSFs with a simple cubic (SC) lattice symmetry, but with $E_s/E_b = 1$ and

$E_s/E_b = 100$. (c)-(d) AHSFs with a face-centered-cubic (FCC) lattice symmetry, but with $E_s/E_b = 1$ and $E_s/E_b = 100$. Here $R = \sqrt{3}/5d$, $R/t = 10$, $l/w = 2$ and $\theta = 18^\circ$.

3.5 Simultaneous existence of omnidirectional acoustic and elastic band gaps

To demonstrate the simultaneous acoustic and elastic wave attenuation capabilities in the proposed 3D AHSFs, we begin by constructing their acoustic and elastic dispersion relations, as shown in Figure 10. For the purpose of comparison, acoustic and elastic wave dispersion relations for the initial cellular solid structure are also presented. As shown in Figure 10(a), no omnidirectional band gap is perceived in the acoustic dispersion relation for the cellular solid structure. This is because the volume fraction (58.1%) of the solid phase is still too low to generate destructive interferences, as evidenced by the eigenmodes at the high symmetry points A and B. While a large omnidirectional band gap ranging from 7.313 kHz to 25.574 kHz emerges in the elastic wave phononic dispersion. Direct observation of the eigenmodes at the high symmetry points C and D indicate that this large omnidirectional band gap is due to the Bragg scatterings of propagating elastic waves (Figure 10(b)). These analyses denote that a large volume fraction of the solid phase is essential for simultaneous noise and vibration control, which eventually compromises their structural efficiency.

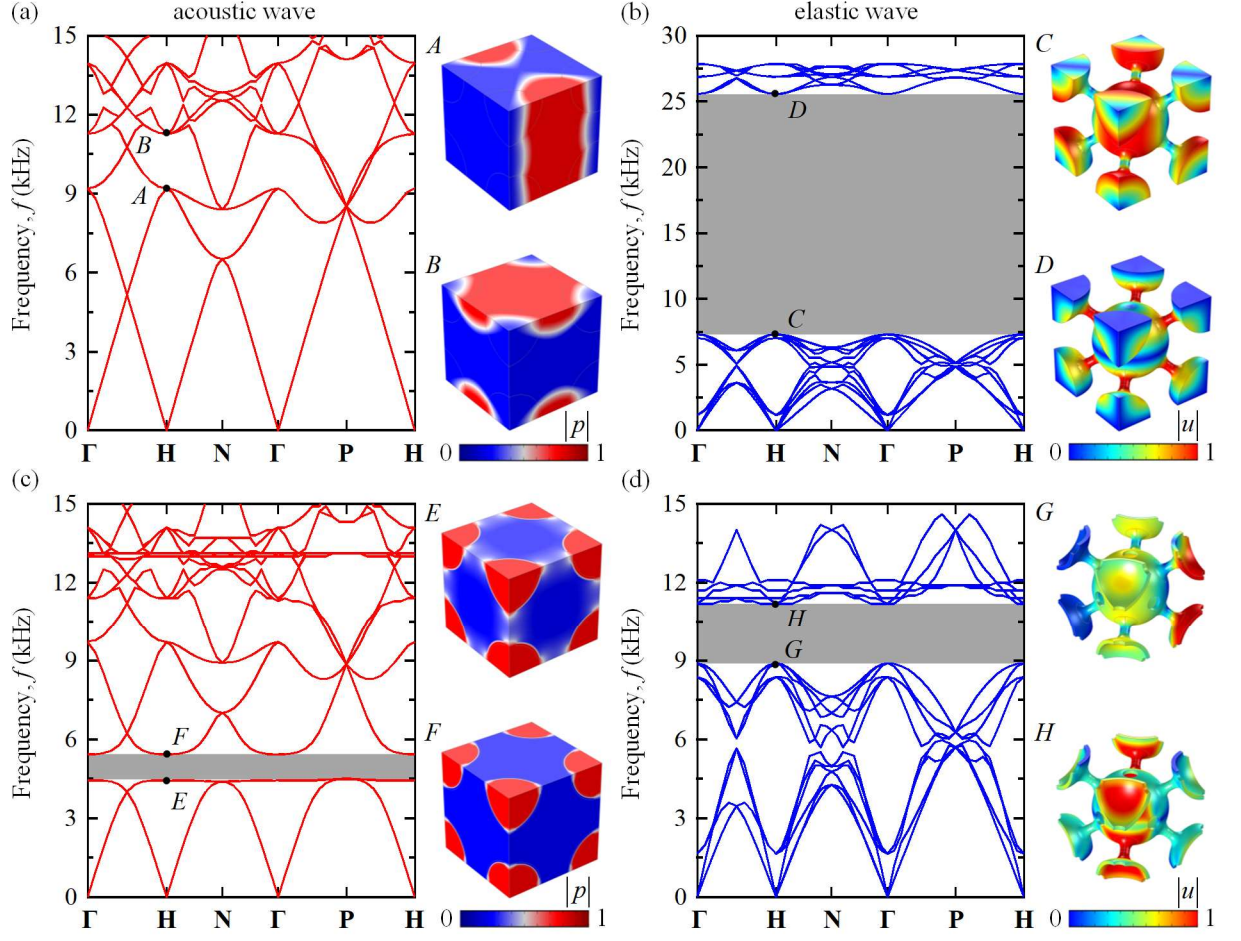


Figure 10 Acoustic and elastic dispersion relations for the conventional solid sphere foam and proposed hollow sphere foam (a) and (b) Acoustic and elastic dispersion relations for solid sphere foam, respectively. (c) and (d) Acoustic and elastic dispersion relations for the proposed hollow sphere foam with $R/t=10$. Here, $a = 3$ cm, $R = \sqrt{3}/5a$, $r_h = 2t$, $l/w=2$ and $\theta=18^\circ$. The gray shaded areas in the dispersion relations represent the omnidirectional band gaps. The contour plots are eigenmodes at high symmetry points of the first irreducible Brillouin zone. The legend for acoustic analysis represents the amplitude of the pressure field, while for elastic wave analysis, the legend indicates the displacement amplitude.

By contrast, an omnidirectional acoustic band gap is observed in the proposed AHSF, due to the local resonance 10(c)). The drilled hollow spheres act as multiple Helmholtz resonators and are regularly connected by the binders. It is interesting to note that even the volume fraction of the solid phase is significantly reduced (from 58.1% to 10.2%), an omnidirectional elastic band gap with considerable width persists. The global vibrational modes at the elastic band gap edges suggest that the Bragg scatterings are responsible for this omnidirectional elastic wave band gap (Figure 10(d)). These numerical simulations imply that by simply modifying the sphere geometry, the acoustic and elastic wave can be attenuated simultaneously, without significantly sacrificing the mechanical properties of the 3D AHSFs.

To validate the simulated acoustic and elastic band gaps in the AHSFs, we calculate the acoustic and elastic wave transmission spectra along $\Gamma - H$ direction by performing frequency domain analyses on finite-size AHSFs. Perfectly matched layers (PMLs) are applied at the two ends of the homogeneous parts to prevent reflections by the scattering waves from the domain boundaries [34, 116]. The PMLs have the same dimensions as the unit cell. Homogeneous parts having the same width and height, but a length twice that of the unit cell are positioned between the AHSFs and the PMLs. Mechanical properties of the glassy polymer are assigned to both PMLs and the homogeneous parts. To model acoustic wave propagation in the AHSFs, a low-amplitude harmonic pressure field is applied on the surface between the PML and the homogeneous part on the left-hand side. Similarly, to model the elastic wave propagation in the AHSFs, a low-amplitude harmonic displacement is applied on the surface between the PML and the homogeneous part on the

left-hand side. Here, we only consider the longitudinal polarization of elastic waves. We have again used a discretization of 10 elements for the minimum wavelength.

The finite element simulation details are described in chapter 2. Figures 11(a) and (b) show the simulated transmission spectrum for acoustic wave and elastic propagation in AHSFs, respectively. A strong attenuation zone from 4.5 kHz to 5.4 kHz is observed in the acoustic wave transmission spectrum (Figure 11(a)), which agrees well with the partial band gaps along $\Gamma - \text{H}$ direction in Figure 10(c). The attenuation zone from 8.9 kHz to 11.2 kHz for elastic wave propagation (Figure 11(b)) also matches well with the partial band gaps along $\Gamma - \text{H}$ direction in Figure 10(d). To more clearly demonstrate the acoustic and vibration mitigation capabilities of the proposed AHSFs, dynamic response of the AHSFs under excitation frequencies within and outside the band gaps are presented. For example, at point A with a frequency of 3.6 kHz and point C with a frequency of 3.3 kHz outside the band gaps, the incident acoustic wave and elastic wave can propagate freely throughout the AHSFs. By contrast, both acoustic and elastic wave energy is reflected by the AHSFs when the excitation frequencies lie in the band gaps, for example at point B and D. These transmission spectra along with the dynamic response not only validate against the simulated phononic band gaps for infinite AHSFs, but also demonstrate the potential applications of finite-size AHSFs for simultaneous noise and vibration mitigation.

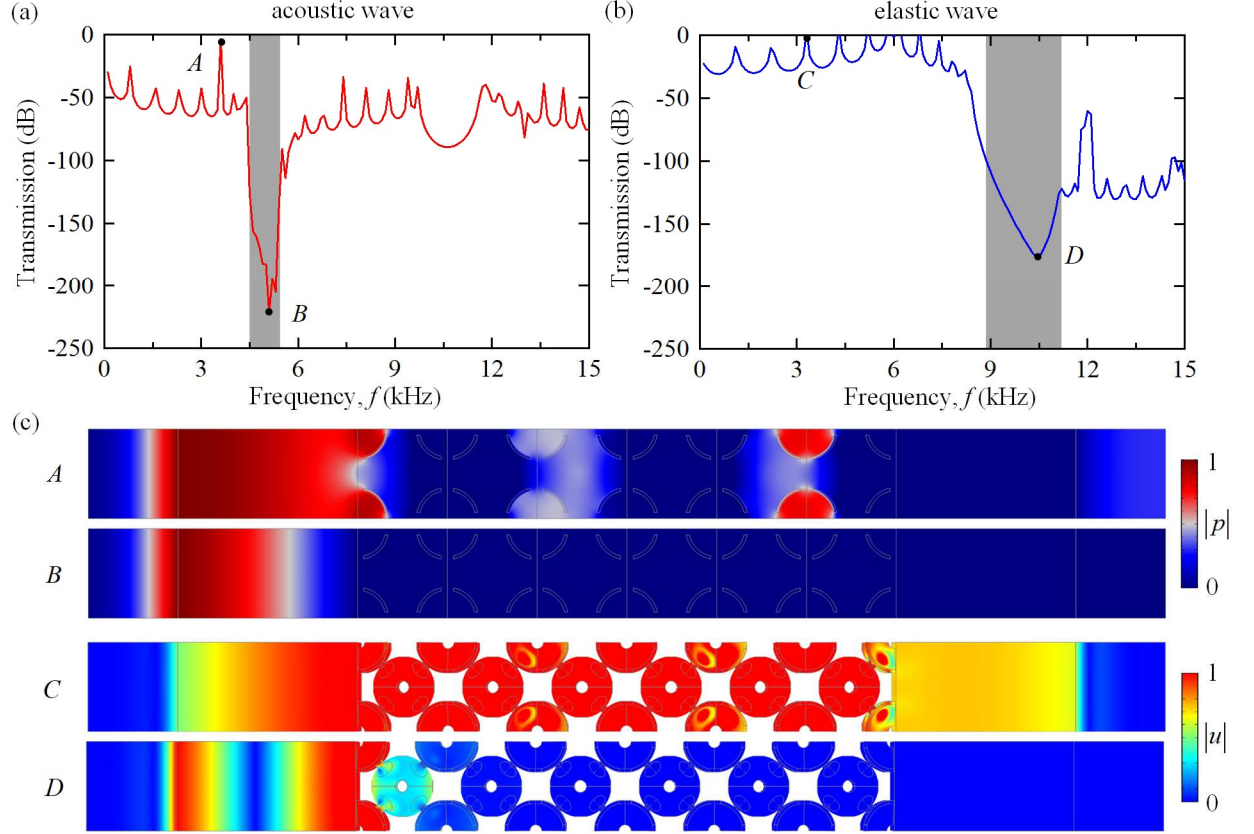


Figure 11 Finite element simulated acoustic and elastic transmission along $\Gamma - H$ direction (a) Acoustic wave transmission spectrum. (b) Elastic wave transmission spectrum. (c) Dynamic response of the finite-size AHSFs under different excitation frequencies. The gray shaded areas in the transmission spectra correspond to the first partial band gaps in figure 10. The legend for acoustic analysis represents the amplitude of the pressure field, while for elastic wave analysis, the legend indicates the displacement amplitude.

3.6 Conclusions

In summary, we have numerically and experimentally demonstrated the existence of an omnidirectional band gap in the 3D printed architected hollow sphere foam. The wave attenuation zone in the measured transmission spectrum agrees well with our numerical predictions. Because of the unique design of the proposed architected foams, we have

shown the design flexibility to change the band gap properties by tailoring the geometric and material parameters of the binder and hollow sphere. Remarkably, without changing the architecture or breaking lattice symmetry, the omnidirectional phononic band gaps can be shifted toward a low-frequency range by simply tailoring the stiffness contrast between hollow sphere and binder. We also evidenced that the proposed design paradigm and the physical mechanisms are robust and are applicable to AHSFs with other lattice symmetries. Remarkably, omnidirectional elastic wave band gaps can be fully decoupled from acoustic waves and independently tuned by tailoring the binder stiffness. The simultaneous acoustic and elastic wave band gaps make the proposed lightweight AHSFs particularly useful for suppressing the undesired noise and vibrations in transportation, navel, and marine engineering.

CHAPTER 4

3D PRINTED ARCHITECTED POLYMER FOAM FOR ENHANCED MECHANICAL PROPERTIES

4.1 Introduction

Recent advances in the industrial and defense industries require innovative engineering designs to address the unprecedented combinations of necessary mechanical properties, including high stiffness, strength, toughness, and energy absorption, with minimal weight and cost. Sandwich structures have attracted increasing interest because of their lightweight, acoustic attenuation, energy absorption, and thermal conductivity. Mechanical behavior of sandwich structures under the blast, low-velocity impact, and quasi-static loading conditions have been extensively investigated. In these sandwich structures, energy-dissipating mechanisms were found to include fiber damage [117], matrix fracture [118, 119], delamination [118, 120], friction [119], core crushing [121, 122], plugging [123, 124], and debonding between the core and facings [118, 125]. In particular, the core of a sandwich structure often absorbs more than half of the initial kinetic energy imparted to plate [125]. Therefore, significant works have been directed towards core topologies. An optimal core should exhibit restricted and constant reactive forces, long-stroke, stable deformation mode, and high specific energy-absorption capacity. However, it is challenging to create such cores because some of the mechanical properties, such as stiffness, strength, and energy absorption, are often mutually exclusive.

Traditionally, random foam materials such as syntactic foams, Voronoi foams, and Alporas foams have been used as sandwich cores. For example, the mechanical behavior of sandwich structure with syntactic foam core was investigated under quasi-static and dynamic loading [45]. It was found that the energy absorption increased by 23% under dynamic load compared to a quasi-static load. In contrast, architected materials with specially designed structures can be employed to achieve engineered mechanical properties and functionalities [49]. Architected materials, such as lattice [50] or honeycombs [51] have been reported to be significantly more structurally efficient than stochastic foams with the same relative density [52]. More recently, functionally graded design strategy (FGDS) has drawn much attention due to its lightweight, damager tolerant, and high energy absorbing capability. FGDS was first proposed by Niino et al. [53] to overcome the huge temperature difference between the outer surface of the spacecraft and the internal space caused by air friction. Since then, this concept has enlightened researchers to create novel FGDS to achieve better mechanical performance. Conventional methods of fabricating graded materials have proven to be limited [126], especially for complicated structures. A more state-of-the-art method to fabricate graded materials is additive manufacturing (AM). One way is to design the graded structure in advance, and then print the model by importing the geometry to the printer. The other way is to control the mechanical parameters during the manufacturing process [127-130]. Despite the tremendous efforts devoted to the functionally graded additive manufacturing process, the majority of the research reported has focused on the control in the design process rather than the control of parameters in the manufacturing process to produce graded structures [131].

Architected polymer foam composed of beam binders and hollow spheres is a type of lightweight architected material that exhibits interesting mechanical properties. We recently studied the mechanical behavior of architected polymer foams under large deformations [49]. It was found that tuning the binder is a more efficient way to tailor the mechanical property compared to relative density. In parallel, the effect of wall thickness, perforated hole diameter, binder radius, and spatial arrangement of architected polymer foams on stiffness and initial yield stress was investigated [132]. The crushing behavior of Simple-Cubic (SC) metal hollow sphere foams with uniform, random, and graded design was investigated [133]. They showed that the deformation modes of the three types of models tend to be consistent when the impact velocity increases. But the impact resistance will increase if the high-density part is positioned in the impact end, which agrees with the findings from [134, 135]. In addition to these mechanical properties, we found that these architected foams can be engineered with simultaneous noise and vibration control capabilities [136]. Notably, it was reported that the phononic band gap can be shifted to a low-frequency range by changing the stiffness difference between spherical shell and binder [137]. Most of these works are focused on the uniform design of architected foams. Here, following our previous work, we will explore the role of different graded designs on the mechanical performance of architected foams. We first systematically study the effect of the binder size and shell thickness on the mechanical behavior of architected uniform foam (UF) (Figure 12(a)). Then we focus our work on the investigation of three types of graded designs, which are graded binder foam (GBF), graded thickness foam (GTF), and hybrid graded foam (HGF) (Figure 12(b)-(d)).

4.2 Model description

The representative volume element (RVE) of the proposed architected foam model consists of perforated spherical shells and beam binders, as shown in Figure 12(e). The lattice constant of the RVE is a . The detailed geometrical dimensions are shown in Figure 12(f). Perforated spherical shell is characterized by external radius R , thickness t , and perforated radius r . Binder is featured by the binder angle θ , fillet radius b , and strut length l . It should be noted that unlike the perforated spherical shell, the binder can be fully determined by any one of its featured parameters, θ , b , or l can be equivalently expressed by external radius R and binder θ . In our following investigation, we will use θ to characterize the size of the binder for the purpose of consistency.

Here, in our design, we adopt the assumption [49]

$$R = 6\sqrt{3}a/25 \quad (4.1)$$

The perforated radius is fixed as

$$r = 3R/10 \quad (4.2)$$

With Eq. (4.1) and (4.2), and the featured dimensions in Figure 12(f), the relative density of the UF can be calculated as

$$\frac{\rho}{\rho_s} = \left(\frac{6\sqrt{3}}{25}\right)^3 \left\{ \frac{91\sqrt{91}\pi}{750} - 2\pi \left(\frac{91}{100} - 2\frac{t}{R} + \left(\frac{t}{R}\right)^2 \right)^{0.5} \left(\frac{91}{150} - \frac{4}{3}\frac{t}{R} + \left(\frac{t}{R}\right)^2 \right) + \frac{\pi}{12} \left(\frac{25}{24} \tan \theta + 1 - \frac{25}{24 \cos \theta} \right) \right\} + c \left(\frac{t}{R}\right)^3 \quad (4.3)$$

where c is the correction coefficient for the volume of binder due to the difficulty of obtaining it analytically. $c = 0.65$ is determined by fitting Eq. (4.3) with CAD calculations [138]. By altering the spherical shell thickness t , one can change the relative density. By modifying the binder angle θ , one can tailor the size of the binder. The GBF, GTF, and

HGF are designed by varying binder angle and shell thickness. It should be noted that in our design, the external radius R is kept unchanged.

The UF model, here, is defined by $\rho/\rho_s = 0.15$, and $\theta = 15^\circ$. The GBF model is defined by $\rho/\rho_s = 0.15$, and θ increasing linearly from 5° to 20° along vertical direction. The GTF model is defined by ρ/ρ_s increasing linearly from 0.15 to 0.30 along vertical direction, and $\theta = 15^\circ$. The HGF model is defined by ρ/ρ_s increasing linearly from 0.15 to 0.30 and θ increasing linearly from 9° to 20° along the vertical direction. Lattice constant $a=25$ mm.

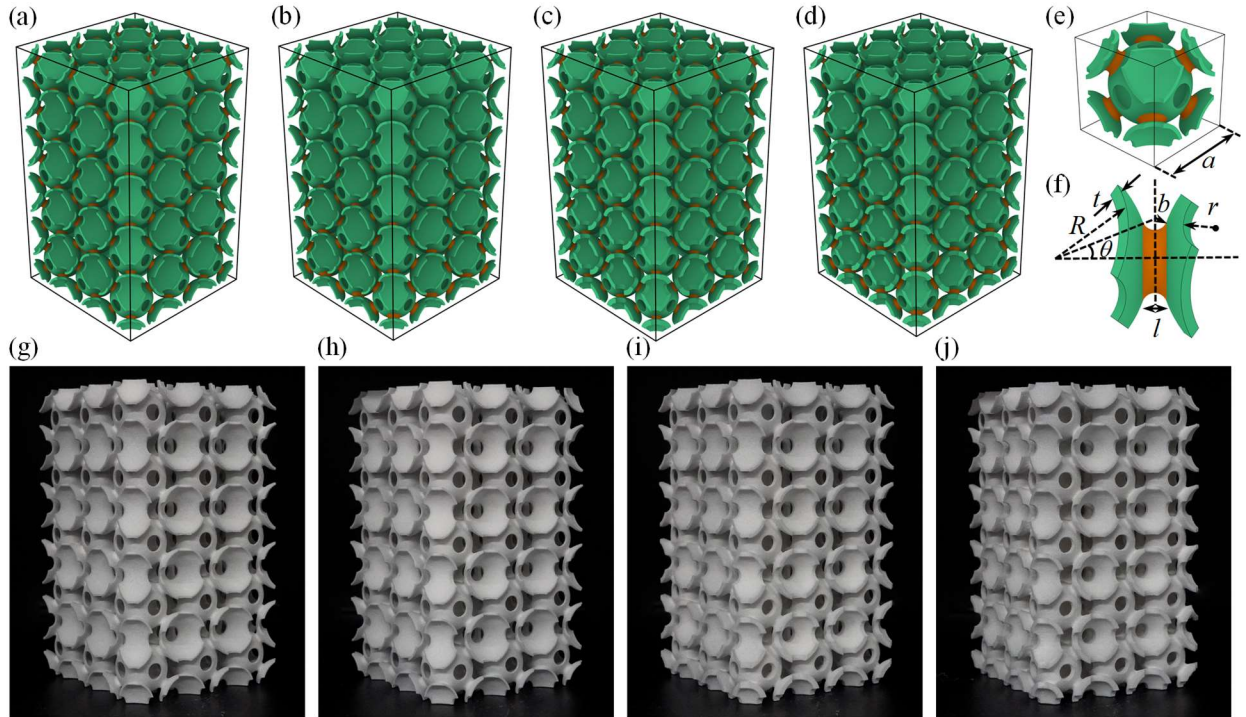


Figure 12 Design and 3D printing of uniform foam (UF), graded binder foam (GBF), graded thickness foam (GTF), and hybrid graded foam (HGF) (a)-(d) $3 \times 3 \times 5$ representative volume elements (RVEs) of UF, GBF, GTF, and HGF. (e) Representative volume element (RVE). a denotes lattice constant. (f) Detailed geometric parameters for

spherical shell and binder. R , θ , t , b , l , r denote spherical radius, binder angle, shell thickness, fillet angle, binder length, and perforated hole radius, respectively. (g)-(j) 3D printed samples of UF, GBF, GTF, and HGF.

4.3 Results and discussion

4.3.1 Effect of binder size

4.3.1.1 Experimental study

The effect of binder size variation on the mechanical behavior of foams is investigated in this section. To this end, seven different binder sizes $\theta = 5^\circ$, 7.5° , 10° , 12.5° , 15° , 17.5° and 20° were considered. For the purpose of comparison, the relative density of each sample was kept the same (0.15). The stress-strain curves for the samples with different binder sizes are shown in Figure 13(a). When the binder size is very small ($\theta = 5^\circ$), the stresses drop to zero at the strain of 0.29. If the binder size is in the medium range ($\theta = 7.5^\circ$, 10° , and 12.5°), the stress-strain curve shows relatively smooth behavior as the deformation proceeds. However, when the binder size is much larger ($\theta = 15^\circ$, 17.5° , and 20°), the stress-strain curve exhibits significant rises and falls for each subsequent failure. These three typical failure modes can be exemplified by three configurations, $\theta = 5^\circ$, 7.5° , and 15° , as shown in Figure 13(b). The three types of failure mechanisms are different from the failure mode in our previous investigation [49]. In our previous work, we only found the third failure mode reported here due to the limited binder range we chose. The failure modes found here play an important role in our graded design structures, as will be discussed later. Deformation patterns of the three failure modes are shown in Figure 13(c)-(e). At the strain $\varepsilon_y = 0.03$, the image of $\theta = 5^\circ$ model shows that one of the binders fractured, as highlighted in the image. Meanwhile, the spherical shells remain intact,

indicating the inability of the binder to connect shells effectively. On the other hand, $\theta = 7.5^\circ$, and $\theta = 15^\circ$ models exhibit no signs of fracture at this point. As the strain proceeds to $\varepsilon_y = 0.1$, $\theta = 5^\circ$ model displays that more binders fail without notable deformation of spherical shells, as one can observe from the highlights in the image. However, at this stage, $\theta = 7.5^\circ$ model begins to show failure for some layers. Unlike $\theta = 5^\circ$, the failure of binders is accompanied by the significant bending of shells. This indicates that binders are strong enough to force the bending deformation of spherical shells, but not strong enough to withstand failure past a certain strain. This mechanism is insightful for our graded design. At this strain, the $\theta = 15^\circ$ model shows spherical shell failure without any signs of binder fracture. As the deformation proceeds, at the strain of $\varepsilon_y = 0.25$, $\theta = 5^\circ$ model shows that most of the binders are failed, which leads to the exploding at the strain of $\varepsilon_y = 0.29$. On the other hand, $\theta = 7.5^\circ$ model exhibits further failure of binders and spherical shells for $\varepsilon_y = 0.25$ and $\varepsilon_y = 0.5$. For $\theta = 15^\circ$ model, layer-by-layer failure occurs at strain $\varepsilon_y = 0.25$ up to $\varepsilon_y = 0.5$. At this stage, there is no observed binder failure even though some of the spherical shells fractured significantly.

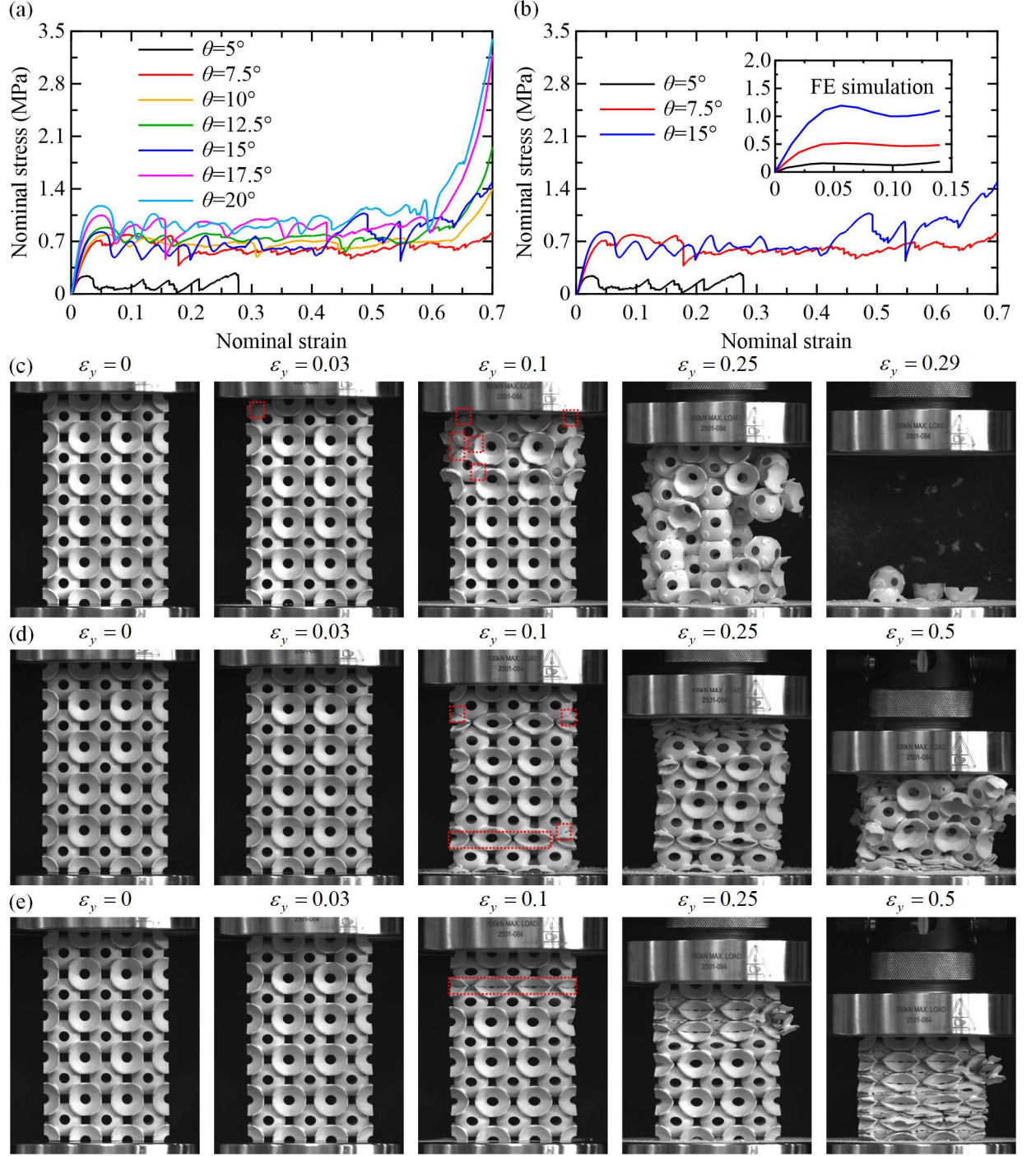


Figure 13 Effect of binder size on mechanical performance (a) Stress-strain curve for different binder sizes. (b) Stress-strain curve for three typical deformation modes and the inset is the FE simulation result. (c)-(e) Deformation patterns for $\theta = 5^\circ$, $\theta = 7.5^\circ$ and $\theta = 15^\circ$ at different strain conditions.

The relative stiffness E/E_s is plotted against binder angle θ on a log-log scale and fitted with a power-law curve, as shown in Figure 14(a). The relationship is found to be $E/E_s \sim \theta^{0.655}$. This relation does not have the classical meaning of deformation mechanism. Instead, it only represents the experimental observation of the relative stiffness with respect to binder angle θ . The bottom horizontal axis of this plot is the binder angle, and the top horizontal axis is relative density ρ/ρ_s . It is shown that increasing binder angle will slightly raise the relative density but significantly enhance the stiffness. For example, when the binder angle increases from 10° to 20° , the relative density increases by 2%. However, the stiffness is enlarged by $\sim 100\%$. The stiffness, strength, and energy absorption for different foams are summarized in Figure 14(b)-(d). The error-bars are attached to these category plots. However, it should be noted that in this group of compressive tests, the repeated tests were conducted for only part of the models due to the expensiveness of printing. The ones that were not repeat tested are $\theta = 10^\circ$, 12.5° , and 17.5° . Nevertheless, from the experimental results of those foams which were repeatedly tested, the results repeated very well. Figure 14(b) and (c) show that the stiffness and strength increase with the increase of the binder angle. It is also found that the strength of $\theta = 5^\circ$ model is considerably low compared to other binder angles. Figure 14(d) shows that energy absorption increases with the binder angle. However, the energy absorption of $\theta = 5^\circ$ is extremely low, indicating the critical role of binder size in designing the architected foam.

4.3.1.2 FE simulation

The purpose of the finite element simulation is to understand how the stress will be distributed around the foam model when the binder sizes are different. To simulate the compression experiments, we fixed the bottom plate translationally and rotationally ($u_x = 0$,

$u_y = 0, u_z = 0, ur_x = 0, ur_y = 0, ur_z = 0$). For the top plate, we constrained all the degrees of freedom except the displacement along z direction ($u_x = 0, u_y = 0, u_z = -87.5, ur_x = 0, ur_y = 0, ur_z = 0$). Figure 15 shows the simulation results for UF with three featured binder angles $\theta = 5^\circ, 7.5^\circ$, and 15° . The purpose of the simulation is to disclose the mechanism of binder size on the mechanical behavior of foams. Therefore, the simulation was performed for compressive strain up to 0.14, as shown in the inset in Figure 13(b). At the strain $\varepsilon_y = 0.01$, the contour plot of $\theta = 5^\circ$ shows that the stress is much more concentrated on local binders than the spherical shells. However, $\theta = 7.5^\circ$ model displays rather even stress distribution on binders and shells. In contrast, the $\theta = 15^\circ$ model exhibits more stress distribution on shells than on binders. At the strain $\varepsilon_y = 0.05$, the stress on the binders further increases for $\theta = 5^\circ$ model, while stress on the shells remains fairly the same. As for $\theta = 7.5^\circ$ model, both the binders and shells are gaining significant stress at this stage, indicating they are playing an equally important role. On the other hand, the stress for $\theta = 15^\circ$ model is more distributed on shells than binders, just like its previous stage. As the deformation proceeds, the same mechanism can be observed for these models at the strain $\varepsilon_y = 0.1$.

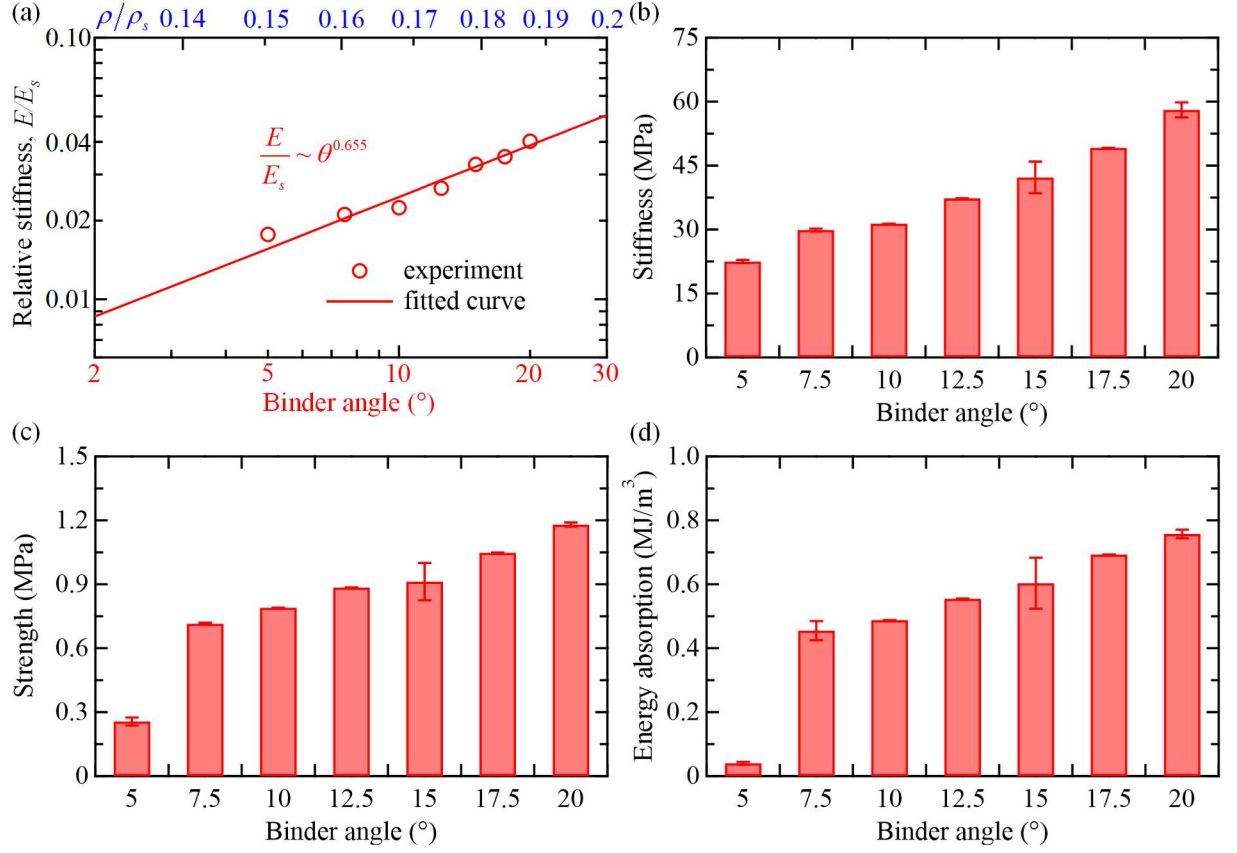


Figure 14 Effect of binder size on mechanical performance (a) Relative stiffness as a function of binder angle and relative density. The circle line denotes the experimental result. The continuous solid line represents the fitted curve. The bottom axis is binder angle and the top axis is relative density (b) Stiffness as a function of binder angle. (c) Strength as a function of binder angle. (d) Energy absorption as a function of binder angle.

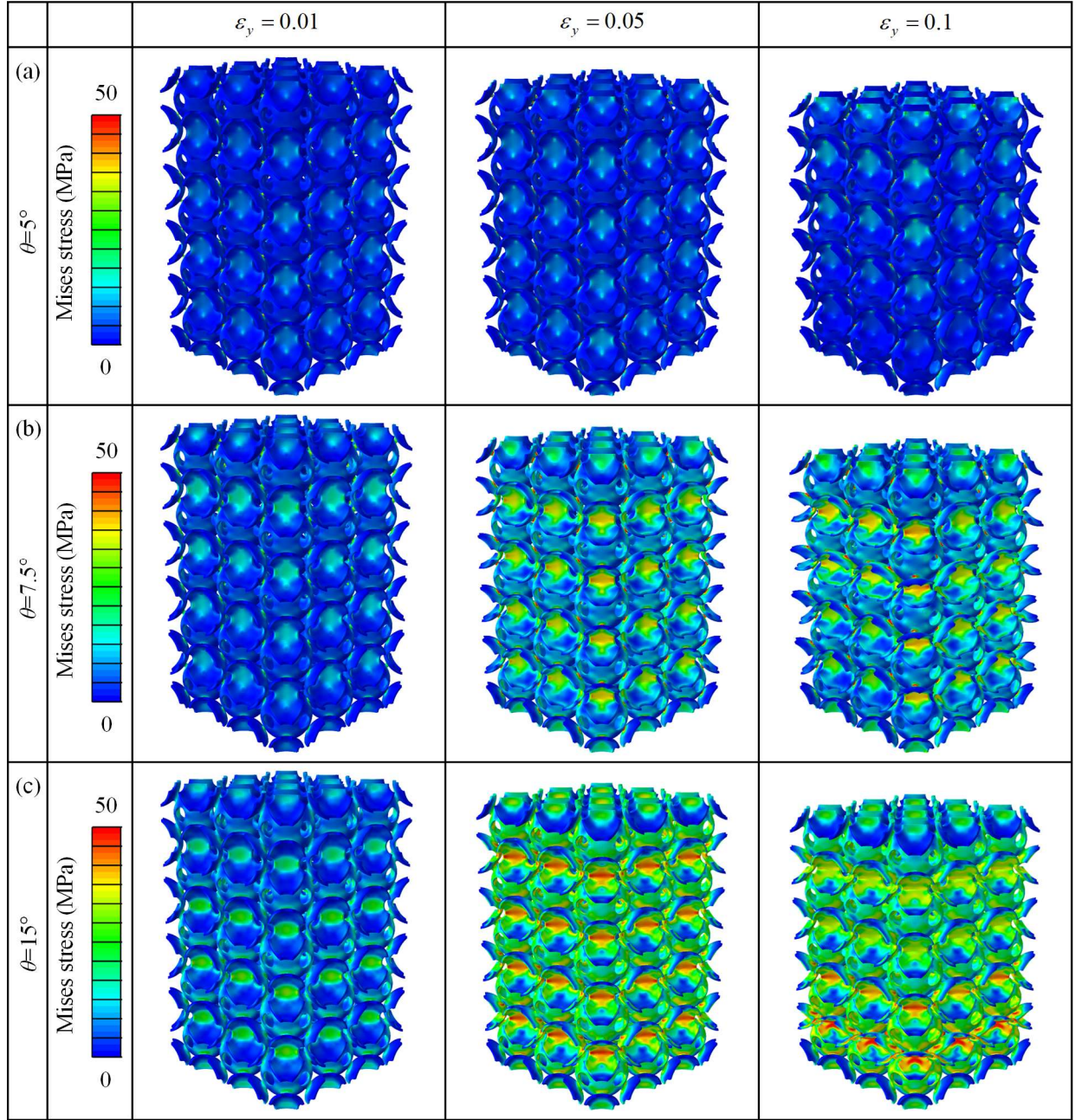


Figure 15 Contour plots of Mises stress of different binder sizes (a) Contour plot of Mises stress for $\theta = 5^\circ$. (b) Contour plot of Mises stress for $\theta = 7.5^\circ$. (c) Contour plot of Mises stress for $\theta = 15^\circ$.

4.3.2 Effect of shell thickness

4.3.2.1 Experimental study

The effect of shell thickness variation on the mechanical behavior of foams is studied in this section. Here, the shell thickness is described by relative density. Four different shell thickness cases were considered, $\rho/\rho_s = 15\%$, 21% , 26% , and 30% . Likewise, the binder angle was fixed to $\theta = 20^\circ$ to isolate the effect of shell thickness. The stress-strain curves for different shell thickness models are shown in Figure 16(a). Considerable differences can be observed in these stress-strain curves across different shell thickness variations. It is noted that with the increase of relative density, the number of peaks-and-valleys is reducing, whilst the difference from peaks to valleys is significantly increasing. This means that more pronounced failure occurs when relative density increases. Figure 16(b) shows the stress-strain curves for the two extreme cases, $\rho/\rho_s = 15\%$, and $\rho/\rho_s = 30\%$. Figure 16(c) and (d) display the deformation patterns for $\rho/\rho_s = 15\%$, and $\rho/\rho_s = 30\%$. At the strain $\varepsilon_y = 0.05$, the second layer from the top of $\rho/\rho_s = 15\%$ model begins to bend substantially, corresponding to the first peak in the stress-strain curve. However, the $\rho/\rho_s = 30\%$ model displays no observable deformation pattern. As the strain increases to $\varepsilon_y = 0.15$, $\rho/\rho_s = 15\%$ model exhibits layer-by-layer failure for the first three layers, corresponding to the beginning three peaks in the stress-strain curve. On the other hand, $\rho/\rho_s = 30\%$ model still shows no noticeable deformation pattern except that global buckling occurs at this point. At the strain $\varepsilon_y = 0.32$, most of the layers failed for $\rho/\rho_s = 15\%$ model through layer-by-layer failure mode. In contrast, $\rho/\rho_s = 30\%$ model features a catastrophic failure, corresponding to the sudden drop of stress on the

stress-strain curve in Figure 16(a). As the strain further proceeds to $\varepsilon_y = 0.6$, $\rho/\rho_s = 15\%$ model is fully packed together, indicating the beginning of densification. $\rho/\rho_s = 30\%$ model, however, is packed disorderly, showing pseudo-densification.

The stiffness of the sample is extracted as the initial slope from strain of 0 to 0.02. The relative stiffness E/E_s is plotted against relative density ρ/ρ_s on a log-log scale and fitted with a power-law curve, as shown in Figure 17(a). The relation is found to be $E/E_s \sim (\rho/\rho_s)^{1.56}$, indicating a bending-dominant deformation behavior. This implies its superior energy absorption performance compared to random foam [52] but inferior stiffness behavior compared to some lattice structures [139, 140]. For example, when the relative density enlarges from 15% to 21%, the stiffness increases by $\sim 100\%$. However, according to our above investigation of the effect of binder angle, the stiffness increases the same amount only by gaining a relative density of 2%. This illustrates that tailoring stiffness by altering binder angle is much more efficient than changing the relative density, which is consistent with previous findings [49]. It should be pointed out that our previous study exhibited significant brittle failure due to different material properties, and in some cases, the stress dropped $\sim 90\%$ after initial yield strength [49]. However, the investigation here shows more ductile behavior. This progressive failure, coupled with the relation between the binder and mechanical performance, serves as the fundamentals for the subsequent graded designs. Yield strength and energy absorption are displayed in Figure 17(b) and (c). As expected, strength and energy absorption are enhanced as the relative density rises.

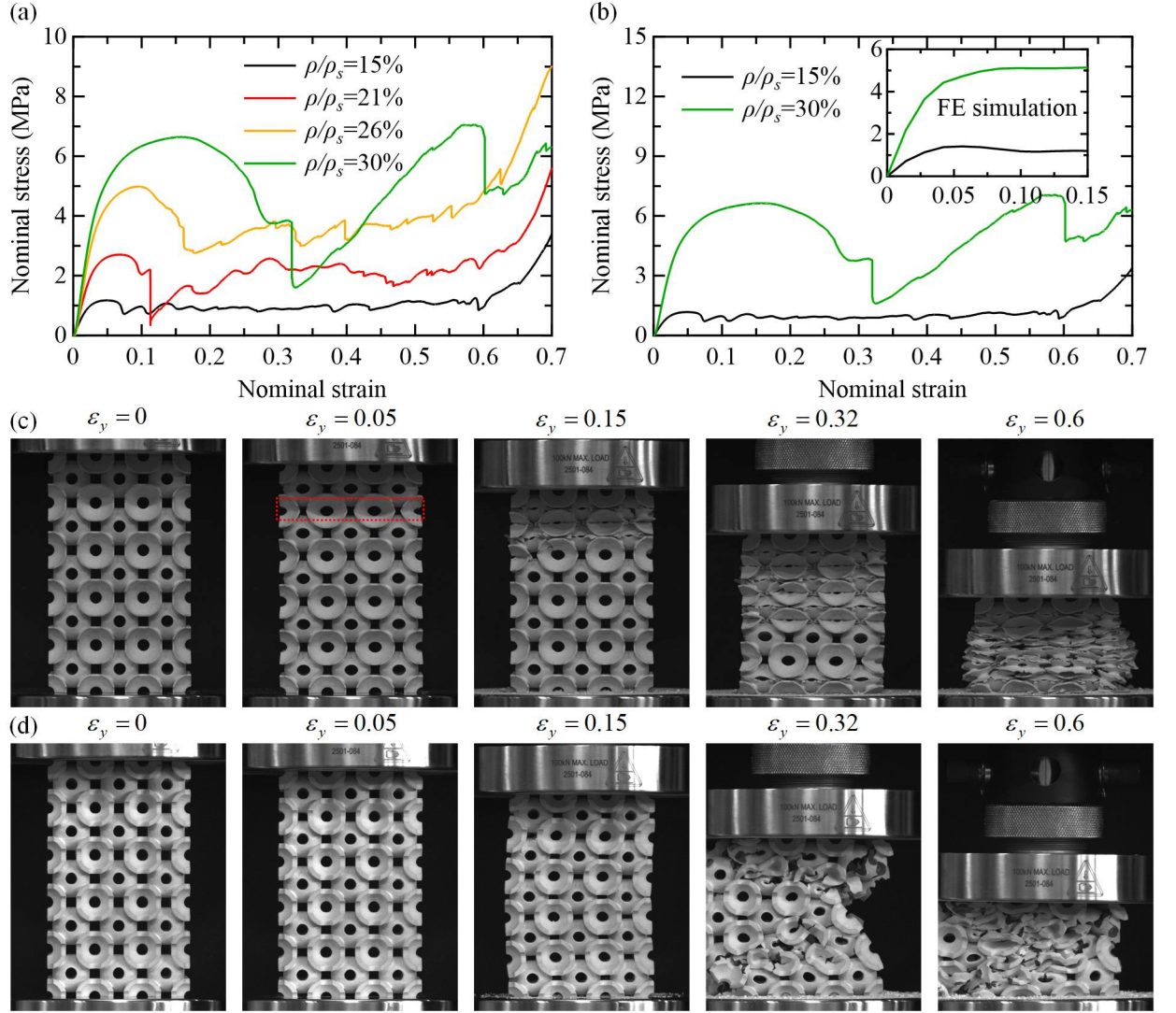


Figure 16 Effect of relative density on mechanical performance (a) Stress-strain curve for different relative densities. (b) Stress-strain curve for two typical deformation modes. The inset is the FE simulation result. (c) and (d) Deformation patterns for $\rho/\rho_s = 0.15$ and $\rho/\rho_s = 0.30$.

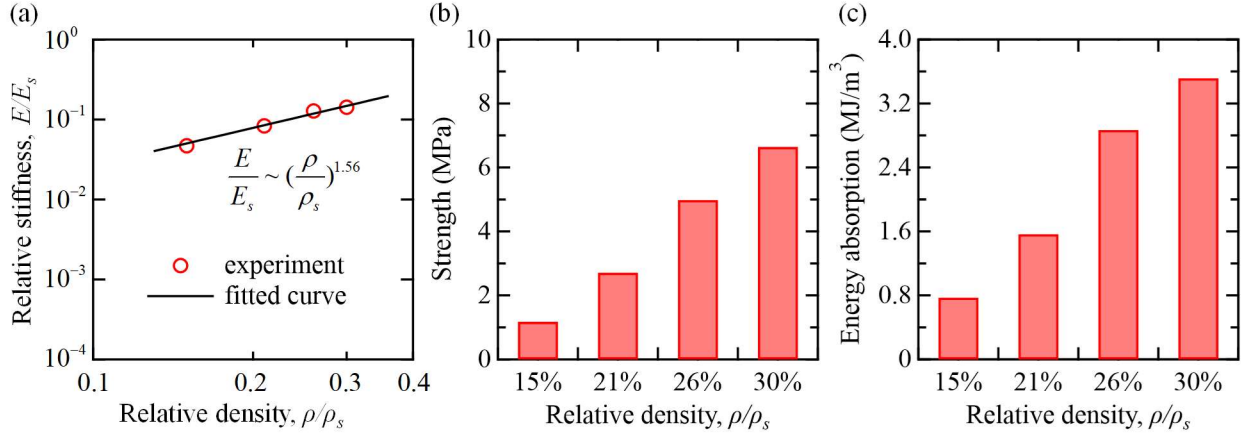


Figure 17 Effect of relative density on mechanical performance (a) Relative stiffness as a function of ρ / ρ_s . The circle line denotes the experimental result. The solid line represents the fitted curve. (b) Stiffness category plot as a function of relative density. (c) Energy absorption category plot as a function of relative density.

4.3.2.2 FE simulation

The purpose of the finite element simulation is to understand how the stress will be distributed around the foam model when the shell thicknesses are different. To simulate the compression experiments, we fixed the bottom plate translationally and rotationally ($u_x=0$, $u_y=0$, $u_z=0$, $ur_x=0$, $ur_y=0$, $ur_z=0$). For the top plate, we constrained all the degrees of freedom except the displacement along z direction ($u_x=0$, $u_y=0$, $u_z=-87.5$, $ur_x=0$, $ur_y=0$, $ur_z=0$). Figure 18 shows the stress contour plot of the simulation results of UF with different relative densities. The corresponding stress-strain curves are displayed in the inset of Figure 16(b). At the strain $\varepsilon_y = 0.01$, the two different relative density models exhibit considerable differences in deformation patterns. $\rho / \rho_s = 0.15$ model shows that the stress is significantly concentrated on the spherical shells, while the stress

of $\rho / \rho_s = 0.30$ model is widely spread across the model. At the strain $\varepsilon_y = 0.05$, the middle two layers of $\rho / \rho_s = 0.15$ begin to show buckling behavior. The experimental stress-strain curve confirms this observation as well. The $\rho / \rho_s = 0.30$ model, on the other hand, shows a further buildup of stress across the entire model at this point. As the strain proceeds to $\varepsilon_y = 0.1$, most of the layers of $\rho / \rho_s = 0.15$ model are buckled. The valley point highlighted in the inset of Figure 16(b) verifies this behavior. However, for $\rho / \rho_s = 0.30$ model, no observable deformation pattern can be found. This explains the smooth rising of stress-strain curve in the inset of Figure 16(b). Meanwhile, the experimental images also confirm this observation at this stage.

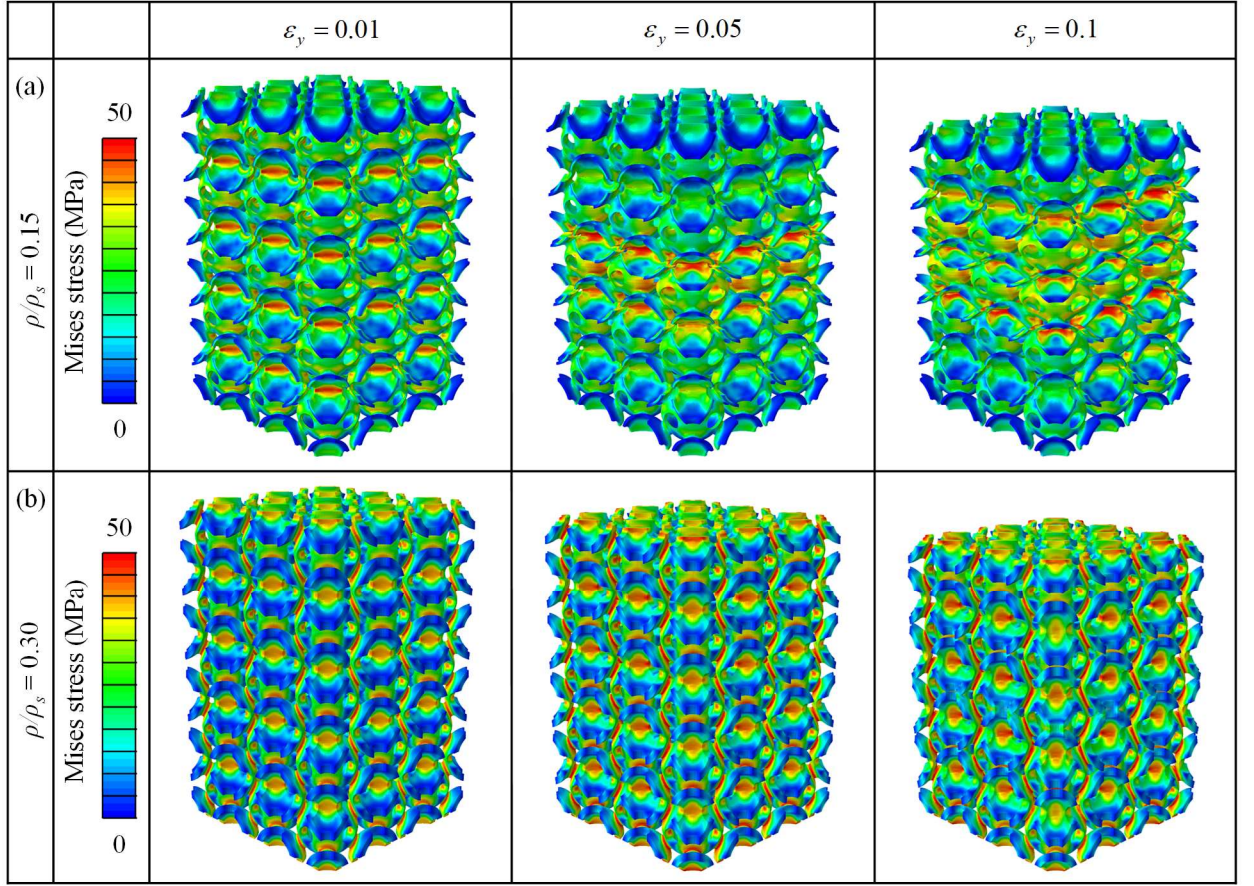


Figure 18 Contour plot of Mises stress of different relative densities (a) Contour plot of Mises stress for $\rho / \rho_s = 0.15$. (b) Contour plot of Mises stress for $\rho / \rho_s = 0.30$.

It has to be pointed out that the finite element simulation results of different thickness model didn't capture the global buckling mode observed in the experimental deformation image in Figure 16. This global buckling could be due to the imperfection of the sample, or because of the boundary conditions or the mechanical tester. This phenomenon will need to be further studied in the future to conduct more experiments, and use the commercial software to simulate the imperfection model to verify what leads to the global buckling phenomenon. Again, this does not affect the general conclusion of our research work that

with the increase of the thickness, the deformation behavior switches from progressive failure to catastrophic failure.

4.3.3 Effect of different graded design strategies

4.3.3.1 Experimental study

In the previous two sections, the effects of binder size and relative density variations on the mechanical performance of foams were investigated separately. The effect of different designs of architected foam is studied in this section. To this end, four design configurations, UF, GBF, GTF, and HGF are considered. Repeated tests were performed for all the samples in this group to eliminate the possibility of rare types of error that may be involved in the experiment. Figure 19(a) shows the experimental and simulated stress-strain curves of UF, GBF, GTF, and HGF. It is noticeable that both UF and GBF exhibit inferior mechanical behavior compared to GTF and HGF. This means that uniform design cannot offer the best option for tailoring foams if the graded design is feasible. However, only designing a graded binder also fails to enhance the performance of foams. On the other hand, both GTF and HGF models exhibit a fluctuant increase of stress before the strain of 0.47. While HGF model keeps rising, GTF model displays a significant drop in stress after this strain. The FE simulation result in the inset shows a similar trend as the experiment. Figure 19(b)-(d) summarize the stiffness, strength, and specific energy absorption (SEA), respectively. It should be noted that SEA here is normalized with respect to UF model. As shown in Figure 19(d), the SEA of HGF model is enhanced by 125% and 185% compared to UF and GBF model. The accumulated specific energy absorption for these four models is plotted in the inset of Figure 19(d). It is found that for the HGF model, the accumulated SEA increases much faster than that of UF and GBF. This indicates that

HGF model is significantly more efficient than UF and GBF model for energy absorption. On the other hand, though GTF shows similar relation with HGF model, the inflection point occurs at a strain of 0.47 for GTF, revealing that HGF is the best option. In fact, the specific energy absorption of HGF model increases by 34% compared to GTF model.

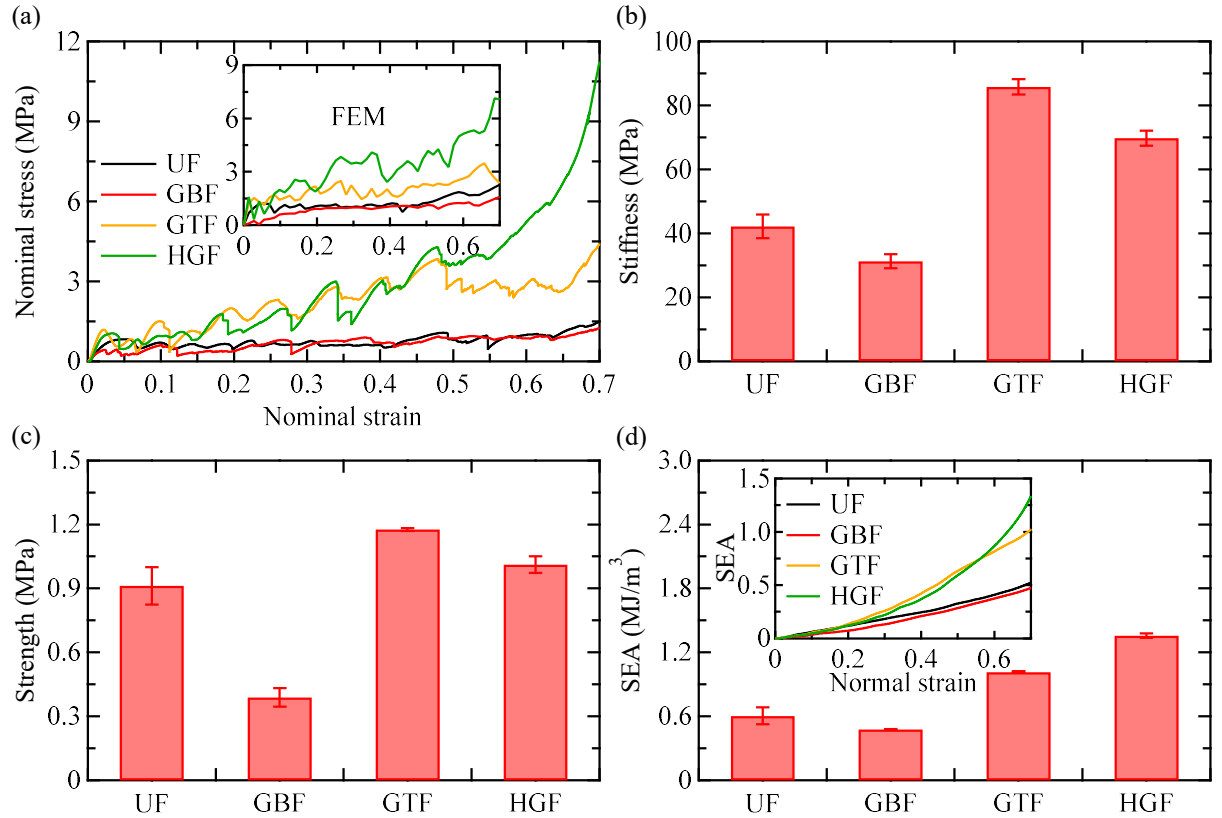


Figure 19 Effect of uniform and gradient design on mechanical performance (a) Experimental stress-strain curve of UF, GBF, GTF, and HGF models. The inset is the stress-strain curve of FE simulation. (b) Stiffness category plot as function of different design configurations. (c) Strength category plot as a function of different design configurations. (d) Specific energy absorption (SEA) category plot as a function of different design configurations.

Figure 20 displays the deformation pattern for UF, GBF, GTF, and HGF model. At the strain $\varepsilon_y = 0.025$, UF model shows no observable failure. GBF model exhibits notable binder failure at the top layer without visible shell bending behavior, meaning that the binder is too weak to bond the spherical shells. This corresponds to the first stress drop on the stress-strain curve in Figure 19(a). GTF model, at this stage, shows discernible shell bending deformation, which corresponds to the peak point on the stress-strain curve. HGF model, unlike the GTF model, reveals no noticeable deformation pattern. This is attributed to the binder size at the top layer. Therefore, the stress-strain curve shows smooth rising at this point. At the strain $\varepsilon_y = 0.14$, the UF model displays a layer-by-layer failure mechanism. In contrast, the GBF model shows that the distinctive binder failure extends to the second layer. The highlights in this deformation image reveal that the two spherical shells remain intact, meaning that the binders of the second layer are not strong enough as well. For the GTF model, the first two layers failed at this moment. However, from the highlighted area, it is noticed that the binders remain intact even though the spherical shells are fully fractured. This observation indicates that the binder is extremely strong, and a catastrophic failure is prone to occur. At this point, the HGF model also shows that the first two layers failed, but no visible intact binder is found in the first layer. As the deformation proceeds, at the strain $\varepsilon_y = 0.47$, all the layers of UF model fail by way of layer-by-layer failure. On the other hand, unlike its previous failure mode, GBF model shows that the binders at this stage are so strong that they remain intact even though shells fractured, as shown in the highlights. By contrast, GTF model displays the inability of the binders to function as effectively as in previous stages, shown in the highlights. This explains why stress drops at the strain of 0.47 on the stress-strain curve in Figure 19(a). As for HGF

model, the deformation proceeds consistently with previous stages. Unlike GTF model, there is no sustained stress-drop for HGF model. However, due to the fracture randomness, it is almost impossible to observe the ideal deformation pattern of one-layer shell failure followed by one-layer binder failure. This is responsible for some intact binders in the previous fractured zone. At the strain $\varepsilon_y = 0.55$, the UF model begins to pack together to prepare densification. The GBF model shows layer-by-layer shell failure at this stage. On the other hand, the image of the GTF model further highlights the weakness of the binders. The HGF model shows densification at this point, which can also be observed from the rise of the stress-strain curve in Figure 19(a).

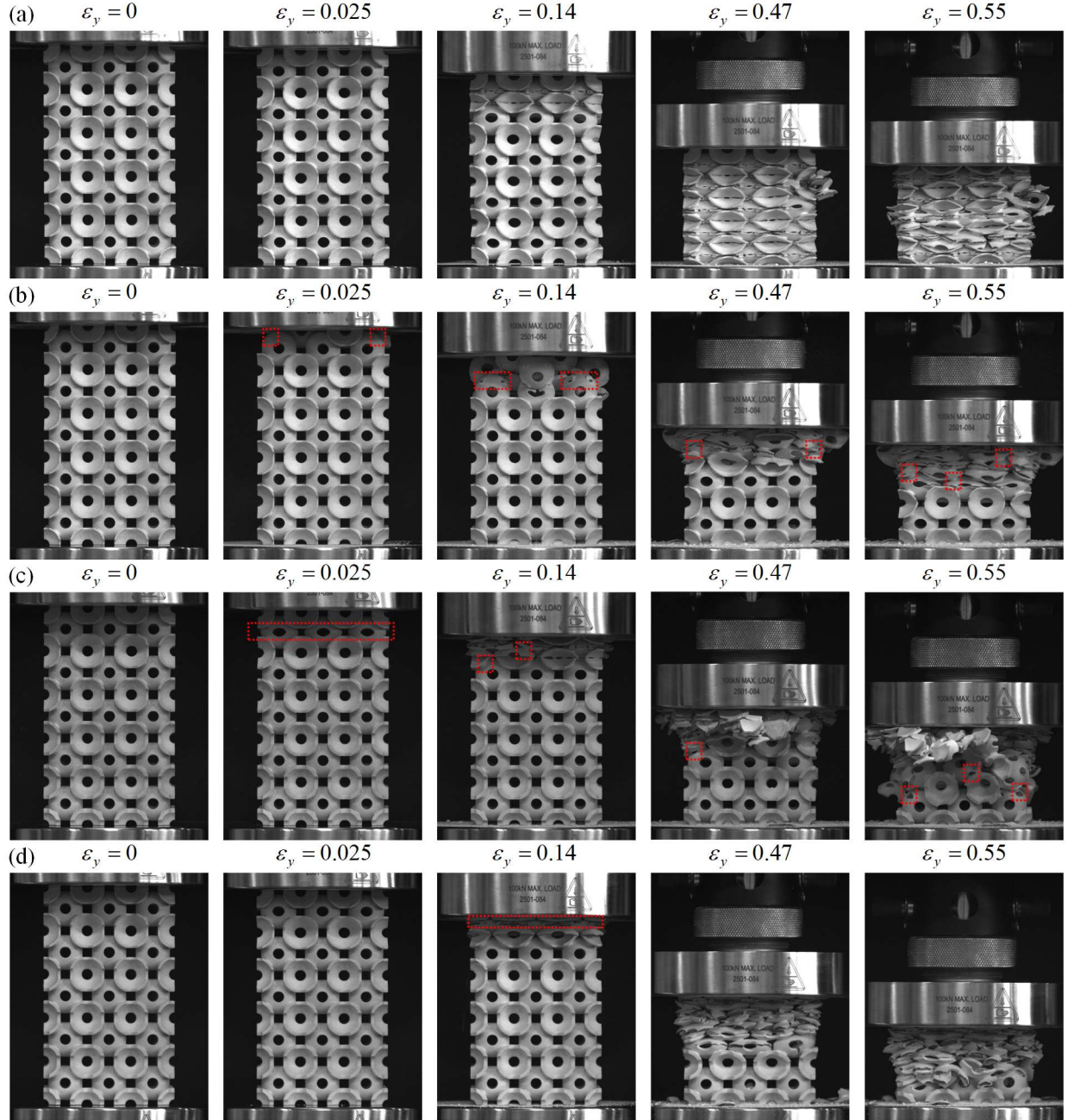


Figure 20 Effect of uniform and gradient design on mechanical performance (a)-(d)

Deformation patterns for the UF, GBF, GTF, and HGF models at different strains.

4.3.3.2 FE simulation

Figure 21 shows the stress contour plot of simulation results of UF, GBF, GTF, and HGF models. As mentioned before, fracture criterion was deployed in the simulation

investigation in this section. However, due to the setup of fracture strain value in Abaqus/Explicit. The Abaqus/Explicit is a finite element analysis product that is particularly powerful to effectively handle severely nonlinear behavior such as contact, which makes it very attractive for the simulation of many quasi-static events, such as crushing of energy absorbing devices, i.e., the architected foam structure studied in this work. In our research study, the fracture will not occur when the binder is robust enough. This is why shells fracture and fall off for the GBF and HGF models, but not for the UF and GTF models. At the strain $\varepsilon_y = 0.014$, the UF model shows the stress is mainly concentrated on the spherical shells of all layers. In contrast, the GBF model displays that stress is overwhelmingly concentrated on the binders of the first layer, meaning that the weakest part of this model is the binder in the first layer. On the other hand, both GTF and HGF reveal that the stress is increasingly spread from the bottom to the top, indicating that the top layers function more efficiently than the bottom layers at this moment. Meanwhile, the stress on the binders of GTF model is almost the same. However, the stress on the binders of the HGF model is distributed similarly to the stress on the spherical shells. This means that the binder at the top functions more efficiently than on the bottom. At the strain $\varepsilon_y = 0.1$, the UF model shows buckling of spherical shells for the second layer to the bottom. At this stage, the first layer of shells of GBF model falls off from the model due to the weakness of the binders in this layer, similar to what was observed in the experiment. In contrast, the GTF model shows no fracture at this point, signifying the robustness of the binder. For the HGF model, the first layer of shells falls off from the model as well. However, it should be noted that this is not the same as the GBF model. The spherical shells in the GBF model function far less efficiently than those in the HGF model before

falling off from the model because of significantly less stress distribution on the shell of GBF model than that of HGF model. At the strain $\varepsilon_y = 0.3$, the UF model shows shell buckling of most layers. On the other hand, the GBF model displays that the shells keep falling off as deformation proceeds. However, the GTF model exhibits that the binder is not robust enough to sustain the load, as highlighted in the red area. This is responsible for the stress drop on the stress-strain curve in the inset of Figure 19(a). The HGF model follows the same deformation pattern as previous stages at this point.

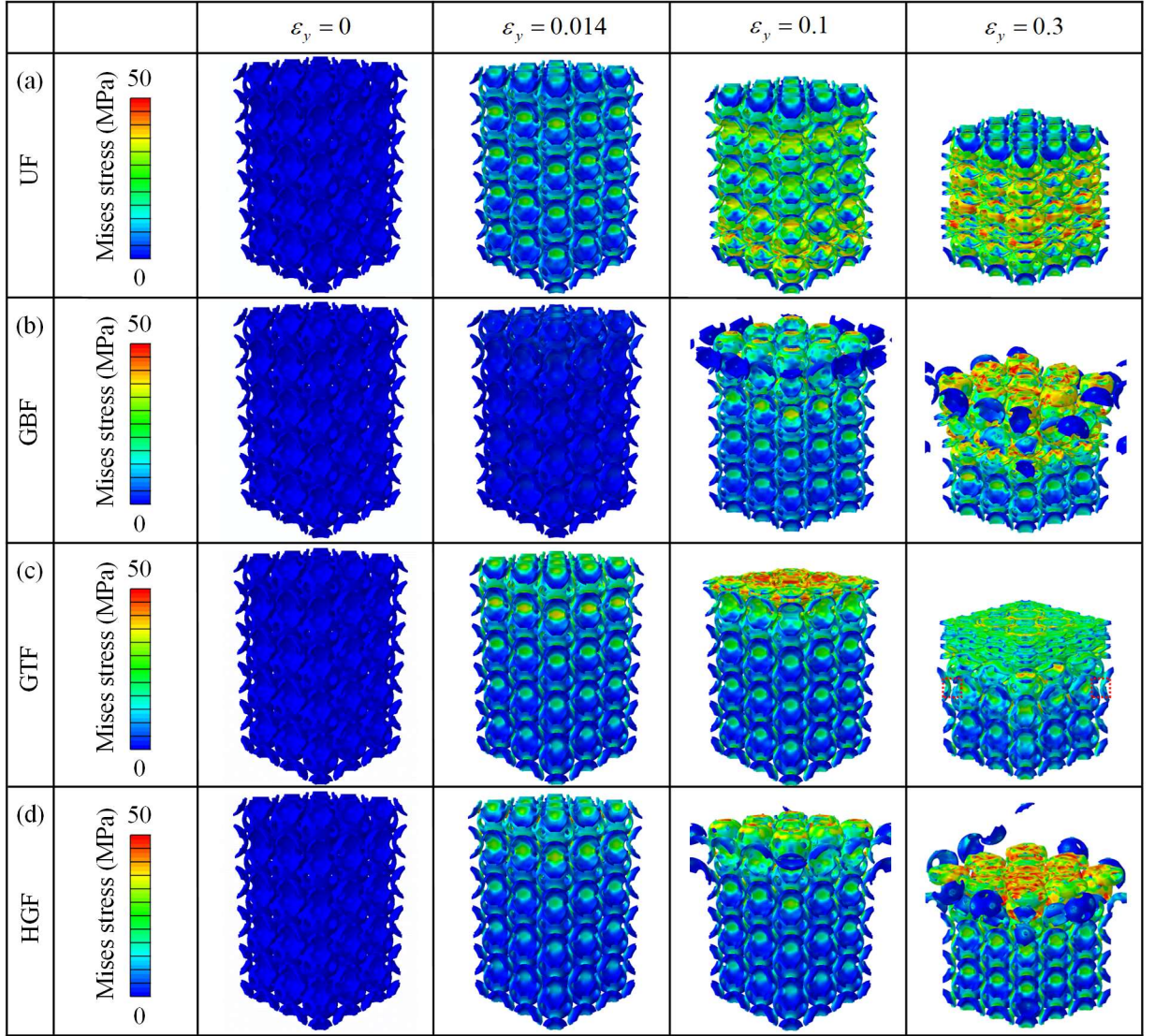


Figure 21 Contour plot of Mises stress of uniform and graded design models (a)-(d)
Contour plot of Mises stress for UF, GBF, GTF, and HGF models at different strains.

4.3.4 Comparison of graded designs with existing architected materials

Having studied the effect of binder size, relative density, and different design parameters, we compared the proposed designs with two other typical graded design structures that have been widely investigated [141]. To do so, the graded BCC-lattice model and graded TPMS-shell model were considered. To obtain a legitimate comparison, we adopted the

design strategy like our proposed model. The relative density at the top is kept as $\rho/\rho_s = 0.15$, and $\rho/\rho_s = 0.30$ is maintained for the bottom. This gives almost the same volume for these three models. The investigation in this section was conducted only in FE simulation due to the inadequate ductile property of nylon material. Meanwhile, no fracture criterion was incorporated in the simulation.

Figure 22(a) shows the stress-strain curves of the three configurations. It is noticeable that both the graded lattice model and HGF model exhibit smooth rising of stress when the deformation proceeds before the strain of 0.55. However, after this point, the graded lattice model begins to gain stress quite radically, while HGF model still displays progressively increasing stress. On the other hand, the graded TPMS model reveals considerably different stress marching behavior, which shows continuous oscillation during stress rising. Figure 22(b) displays the stiffness. Interestingly, the stiffness of graded lattice is significantly smaller than the graded TPMS and HGF model. Meanwhile, the HGF model outperforms graded TPMS in this regard. The stiffness of HGF increases by 346% and 33% compared to the graded lattice and graded TPMS model, respectively. The accumulated SEA curves are plotted in Figure 22(c). The HGF model is notably more efficient in energy absorption than the graded TPMS and graded lattice model. It should be noted that the turning point as highlighted for graded lattice in Figure 22(c) cannot be considered as increasing efficiency because the densification represents the collapse of the structure, which should be treated as more of a solid than a cellular structure. Figure 22(d) exhibits the specific energy absorption before densification. It is found that the SEA of HGF model increases by 141% and 32% when compared to the graded lattice model and graded TPMS model, respectively.

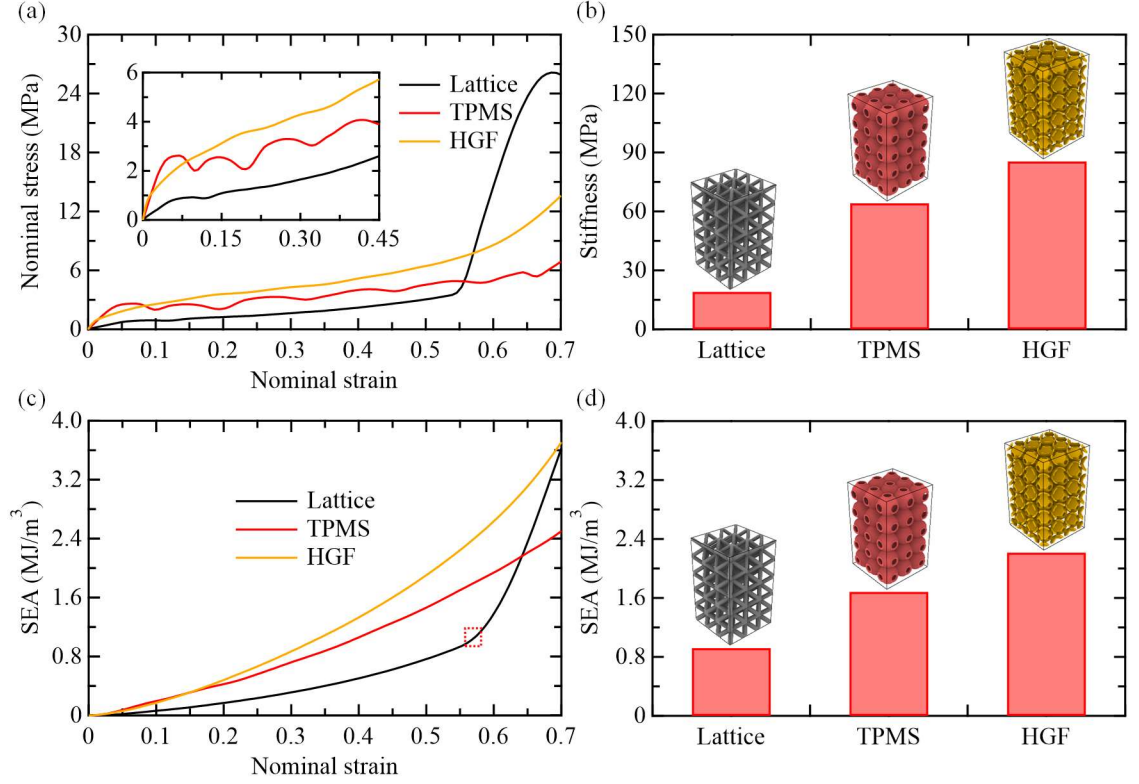


Figure 22 Comparison of typical graded materials (a) Stress-strain curve for graded lattice, graded TPMS, and HGF model. The inset is the stress-strain curve with a strain from 0 to 0.45. (b) Stiffness category plot as a function of different design configurations. (c) Accumulated specific energy absorption (SEA) curve as a function of strain. (d) Specific energy absorption (SEA) category plot as a function of different design configurations.

Here, we discuss the simulated mechanical behavior of different architectures. First of all, the graded lattice, graded TPMS structure, and the proposed HGF model are shown in Figure 23. The relative density for each model increases linearly from $\rho/\rho_s = 0.15$ to $\rho/\rho_s = 0.30$. We use the same constitutive model expect that no damage or fracture was considered. The Mises stress contour plot is shown in Figure 24. At the strain $\varepsilon = 0.05$, the graded lattice shows significant less stress distribution than graded TPMS and HGF model. This explains the low stress-strain behavior in Figure 22 (a). Compared with the graded

TPMS model, the HGF model shows considerable stress concentrated on the binder, while the graded TPMS model shows no observable difference between shells and binders. At the strain $\varepsilon = 0.15$, stress is largely concentrated on the strut joints rather than struts. This indicates that these struts are not fully used under compression. In contrast, graded TPMS and HGF model show relatively uniform stress distribution. However, the first layer binders of the HGF model experience substantial plastic deformation at this stage, while the graded TPMS model only shows shell buckling, as highlighted in Figure 24(b). This behavior corresponds to the fluctuation of the stress-strain curve of the graded TPMS model and a smooth climbing of stress for the HGF model. The significantly different responses further emphasize the vital role of binders in tailoring the mechanical performance of structures. At the strain of $\varepsilon = 0.55$, the struts of the graded lattice accumulate, leading to the turning point of stress-strain relation in Figure 24(a). The graded TPMS exhibits a layer-by-layer shell buckling behavior. In contrast, the HGF model shows simultaneous shell and binder buckling.

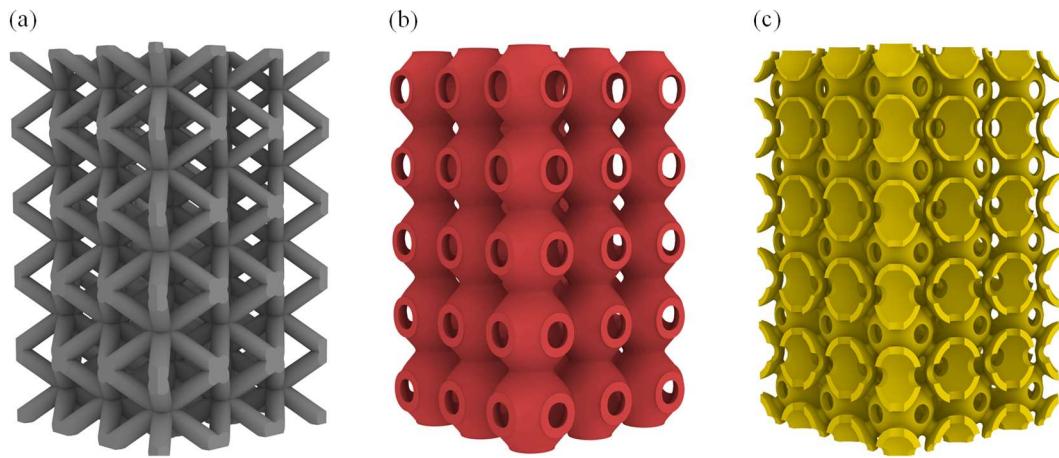


Figure 23 Three architected materials with graded design (a) Graded BCC lattice model. (b) Graded TPMS model. (c) HGF model.

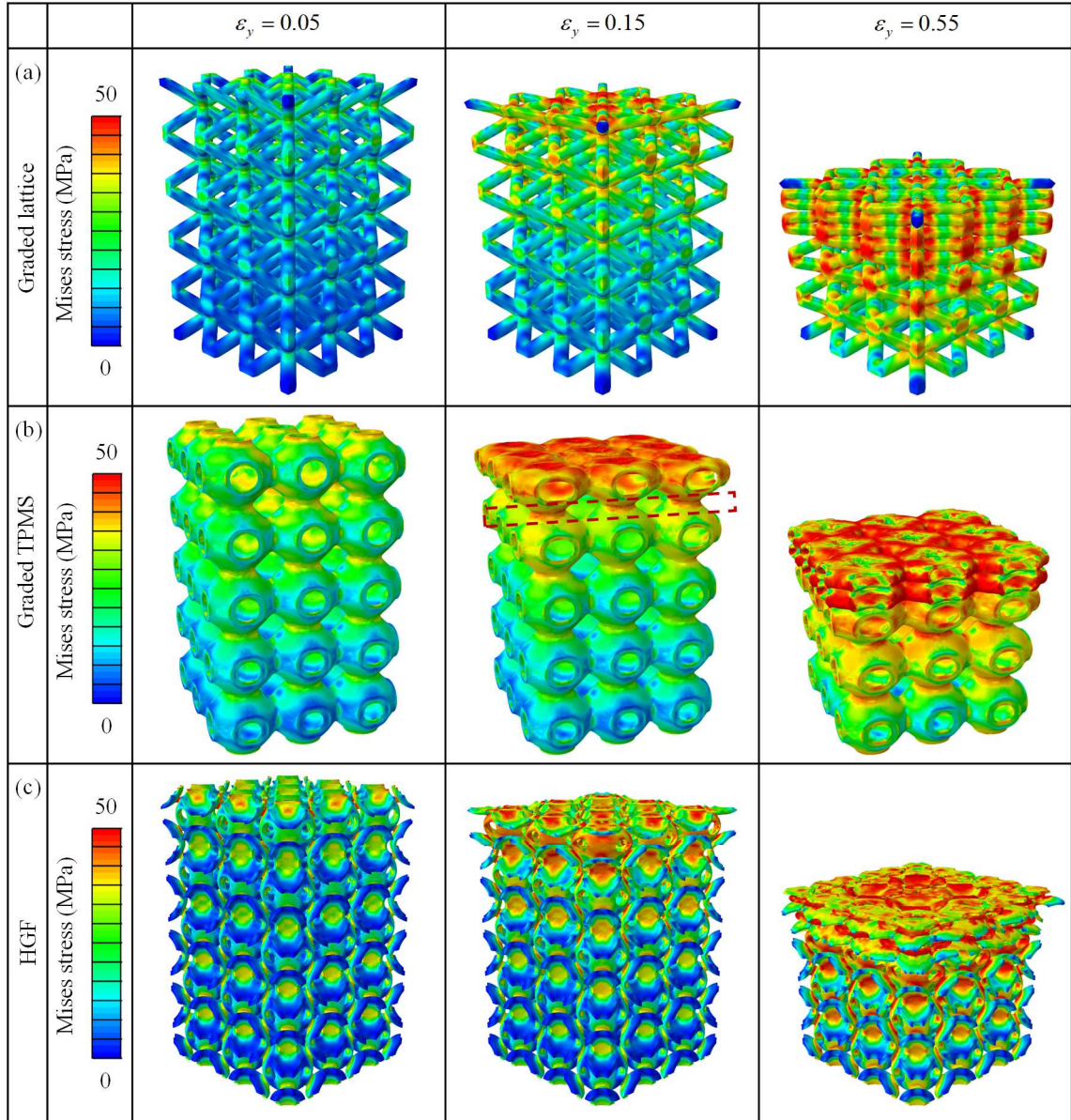


Figure 24 Mises stress distribution of three architected materials with graded design (a) Mises stress distribution of graded lattice model. (b) Mises stress distribution of graded TPMS model. (c) Mises stress distribution of HGF model.

4.4 Conclusions

In this work, the effects of three types of graded designs, including binder size, shell thickness, and a hybrid strategy, on the compressive mechanical performance of architected polymer foams are investigated. It is found that three failure mechanisms dominate the behavior of different binder sizes. When the binder is small, stress will concentrate on the binder, leading to the failure of the binder. If the binder is medium-size, stress will spread to the binder and spherical shell uniformly. Therefore, the binder failure will be accompanied by the failure of the spherical shell. If the binder is large enough, significant stress will gather on the spherical shell. This results in the failure of the spherical shell. Moreover, the stiffness of architected foam can be tailored by choosing the proper binder size. When the binder angle increases from 10° to 20° , the relative density increases by 2%, and the stiffness is enlarged by $\sim 100\%$. On the other hand, the investigation of shell thickness variation shows that the relation between relative stiffness and relative density is $E/E_s \sim (\rho/\rho_s)^{1.56}$, indicating a bending-dominant deformation behavior. Investigations on graded designs indicate that the HGF model is significantly more efficient than UF and GBF models for energy absorption. The specific energy absorption of the HGF model is enhanced by 125% and 185% compared to UF and GBF models, respectively. Meanwhile, the GTF model shares similar energy absorption efficiency with HGF model before the inflection point at the strain of 0.47, after which the efficiency drops significantly. Notably, the specific energy absorption of the HGF model increases by 34% compared to the GTF model. Furthermore, the comparison of the HGF model and existing architected materials shows that the HGF model outperforms these structures in stiffness, energy absorption efficiency, and specific energy absorption. The stiffness of the HGF increases by 346%

and 33% compared to the graded lattice and graded TPMS models, respectively. When it comes to specific energy absorption, the HGF model increases by 141% and 32% compared to the graded lattice model and graded TPMS model, respectively. The findings presented in this work provide guidelines for engineering graded architected foams, which can be employed within a wide range of applications, including packaging, automotive, cores of sandwich structures, and personal protection equipment.

CHAPTER 5

MULTIPHASE COMPOSITES WITH EXCEPTIONAL MECHANICAL PERFORMANCE

5.1 Introduction

Advanced structural materials featuring a combination of lightweight, exceptional stiffness, strength, energy absorption, and damage tolerance are becoming crucially important for multifunctional applications in aerospace, biomedical, semiconductor, and automotive engineering. Lightweight structural materials in automotive engineering offer significant potential to increase vehicle safety and efficiency [142]. A 10% reduction in vehicle weight can result in a 6%-8% fuel economy improvement [143]. This is particularly important for hybrid, plug-in hybrid and electric vehicles, for which lightweight materials improve operational efficiency and increase their all-electric range [144, 145]. Mechanical energy absorption and structural integrity are also essential for automotive structural components to function properly [146-149]; vehicle components such as door assemblies and bumper beams must be robust enough to maintain the safety of passengers even for severe crash conditions [150, 151]. Lightweight, cost-efficient materials and structures are also critical to next-generation aerospace vehicles, particularly emerging electric and hybrid-electric aircraft. To this end, intensive efforts have been devoted to developing lightweight structural composites with exceptional stiffness, strength, impact resistance, and durability. Despite recent advances in materials and manufacturing techniques, the design and

fabrication of low-cost structural materials with lightweight and superior mechanical performance still represent a challenge.

Biological structural materials such as nacre, glass sea sponges, and cellular solids feature unusual mechanical properties that are difficult to reproduce in man-made and artificial materials. For example, the hierarchical assembly of brittle minerals and soft proteins provides nacreous composites an unusual combination of stiffness, strength, damage tolerance, and impact resistance [68, 152, 153]. Recent advances in additive manufacturing such as multi-material and multiscale 3D printing have, however, enabled the production of bioinspired nacreous composites by emulating internal architectures and compositions [62-64, 154]. Similar microstructure designs with the synergistic interplay between hard brittle and soft organic layers have also been identified in glass sea sponges [69, 70, 155, 156], bones [71, 72], and teeth [73, 157]. Cellular solids represent another type of lightweight structural system that can be found in biological materials such as wood and cork [74, 158]. By engineering the topology of cellular materials, one can tailor custom lightweight, high specific strength, and energy absorption characteristics. By using 3D printing techniques researchers have recently developed hierarchical honeycomb structures at cell-wall and macro cellular-structure levels with superior mechanical performance compared with their natural counterparts [159-161]. These numerical and experimental investigations indicate that natural materials are a rich source of inspiration for design principles to develop next-generation structural artificial solids. Most of the current efforts are still nevertheless focused on understanding the fundamental mechanical properties of bioinspired structural materials, such as stiffness, strength, and fracture toughness. Studies related to the mechanical behavior and failure modes under large deformations are

somewhat limited, leaving new deformation mechanisms and optimal materials design principles untapped under such conditions.

In this chapter, we begin by exploring the mechanical behavior of bioinspired multilayered cellular composites under large deformation. The material system investigated here is inspired by the multiscale nature of cork microstructure. Cork is originated from the bark of the oak tree *Quercus Suber* that grows in sub-desertic areas [162]. The microstructure of cork was initially investigated by Robert Hooke in 1664 using an optical microscope and, in modern times, studied in detail by Gibson et al [162]. with a scanning electron microscope (SEM). Cork cells present a hexagonal prism shape (Figure 26(a)) [163]. Due to this unique structure, cork exhibits some outstanding properties, in particular, superior energy absorption that can be used for impact-loaded applications [164]. Another distinctive characteristic of cork is the composition of its cell walls, involving several distinct material layers (Figure 26(b)) [165, 166]. The cork cell walls consist of a thin and stiff, lignin-rich middle lamella (internal primary wall), a thick secondary wall made up of alternating suberin and a wax lamella, and a final thin tertiary wall of polysaccharides (cellulose and hemicellulose). The exact chemical constitution depends, however, on factors such as the geographic origin, the climate and soil conditions, the genetic origin, the dimensions of the tree, together with its age and growth conditions [165, 167]. From a mechanical viewpoint, the combination of its cellular structure and the specific chemical and geometric layout of the lamellae gives rise to the distinctive properties of cork.

5.2 Bioinspired multilayered composites for exceptional performance

5.2.1 Model description

The multilayered cell wall of cork inspires the proposed cellular composite design. It is not the intent of this work to replicate the cork structure at multiple length scales. Instead, we incorporate the multilayered nature into a simple cellular structure. Specifically, the proposed multilayered cellular composite design consists of a triply periodic minimal surface (TPMS) and it is inspired by the multi-material compositions of cork. TPMS models are mathematical surfaces that exhibit zero mean curvature. The smoothness of the surfaces and the absence of intersections enable the reduction of stress concentrations [168, 169]. The Schwarz P minimal surface is one of the simplest TPMS models. For simplicity, the Schwarz P surface has been chosen here as our composite design. The level set function for the surface can be expressed as [170]

$$f(x, y, z) = \cos(x) + \cos(y) + \cos(z) - \frac{1}{2}\cos(x)\cos(y) - \frac{1}{2}\cos(y)\cos(z) - \frac{1}{2}\cos(z)\cos(x) + t \quad (5.1)$$

where the value of t determines the volume fraction of inside and outside the surface. It is found that the minimal surface divides the repeating unit cells (RUCs) in an even manner when $t = -0.3095$. Note that the lattice constant here is $a = 2\pi$ due to the 2π periodicity of this minimal surface function. The printed MCC structure is composed of $3 \times 3 \times 3$ RUCs (Figure 25(c) and (d)).

The model details are shown in Table 1, and Figure 25.

Table 1. The parameters of the models with volume fraction from 10% to 50%.

| Volume fraction | Layer thickness / μm | | | | |
|-----------------|---------------------------|-----|-----|-----|-----|
| % | 1st | 2nd | 3rd | 4th | 5th |

| | | | | | |
|----|-----|-----|-----|-----|-----|
| 10 | 791 | 132 | 791 | 132 | 791 |
| 20 | 703 | 264 | 703 | 264 | 703 |
| 30 | 615 | 395 | 615 | 395 | 615 |
| 40 | 527 | 527 | 527 | 527 | 527 |
| 50 | 439 | 659 | 439 | 659 | 439 |

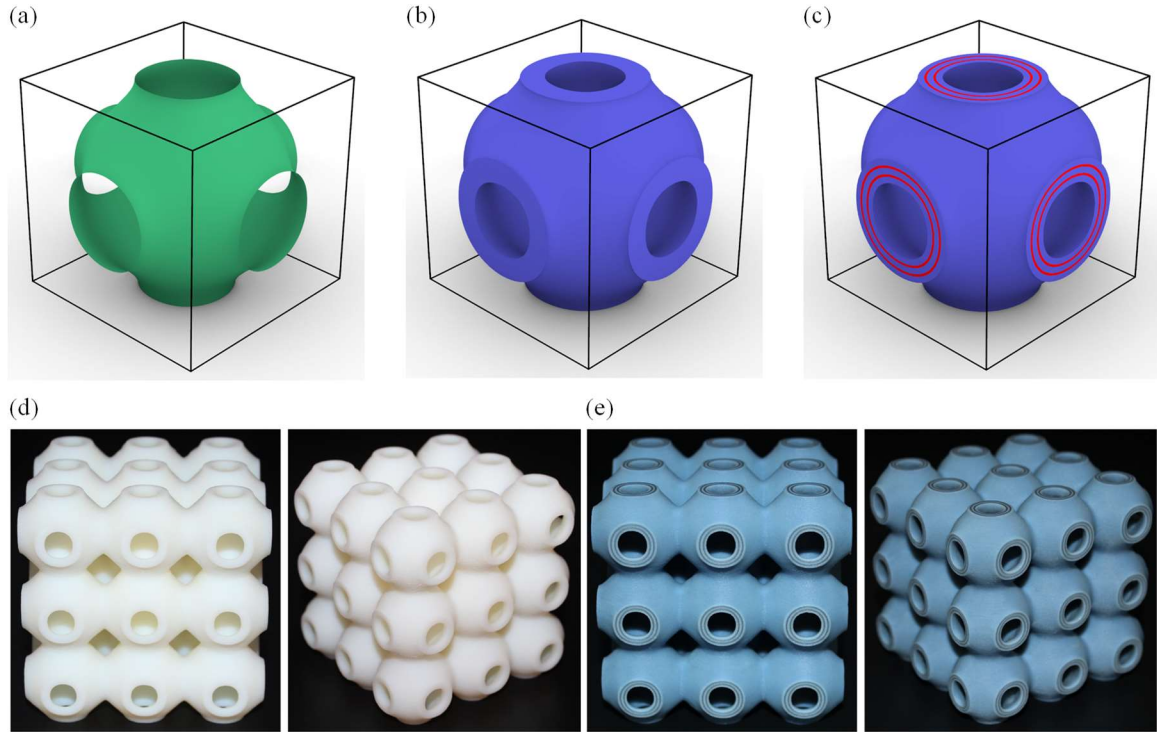


Figure 25 The design process of the proposed multilayered cellular composites (a) Schwarz P minimal surface that divides the representative volume element evenly. (b) Homogeneous VW structure with a volume fraction of 25% and (c) MCC structure with a total volume fraction of 25%. The thickness of each layer from inside to outside is $703\mu m$, $264\mu m$, $703\mu m$, $264\mu m$, and $703\mu m$. (d) 3D printed samples for VW structure and (e) MCC structure.

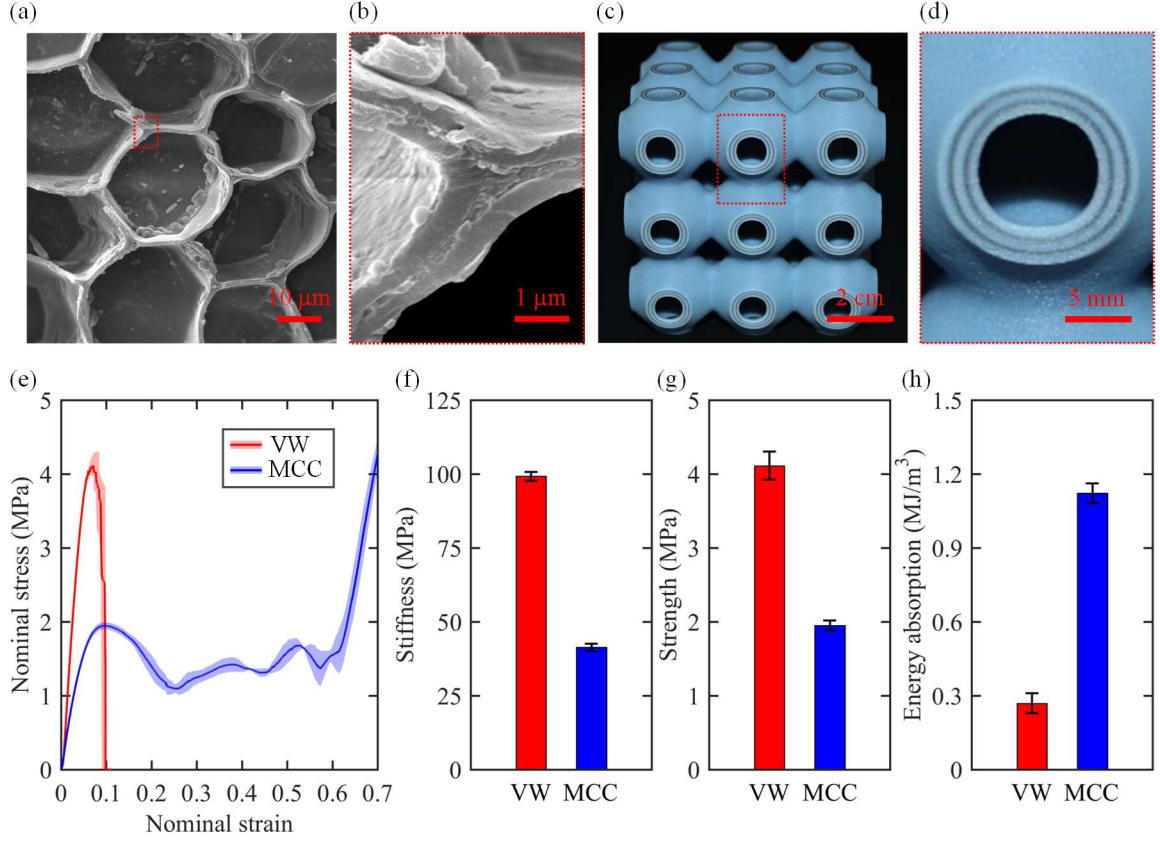


Figure 26 Bioinspired multilayered cellular composite design and uniaxial compression tests (a)-(b) Scanning electron microscope image of cork microstructure and its multilayered cell wall. (c)-(d) 3D printed cellular composite composed of five layers of hard and soft phases. The cellular structure is defined by a Schwarz P minimal surface. (e) Measured compressive stress-strain curves for the 3D printed MCC structure and a VW structure. (f)-(h) Comparisons between the measured stiffness, strength, and energy absorption, respectively.

5.2.2 Results and discussion

5.2.2.1 Uniaxial compression tests

To understand the mechanical behavior of the MCC structure under large deformations, uniaxial compression tests with a strain rate of $5.5 \times 10^{-4} s^{-1}$ have been performed. Figure 26(e) shows the experimental stress-strain curves for the VW and MCC structures up to a

70% compressive strain. Tests were repeated three times and we have observed good repeatability of the results from each test, especially within the small strain range, as indicated by the small variation of stress ranges in the shadow. For the VW structure, the stress increases rapidly until the strain reaches 7% and then drops abruptly to zero, associated with a catastrophic failure mode. The MCC structure is more compliant than the VW configuration, and the initial stress peak occurs at 10% strain, followed by a long stress plateau until approximately 60% of compression before densification. This stark contrast between the two layouts is due to the different failure modes for the VW and MCC structures, which will be discussed below. Comparisons of stiffness, strength and energy absorption between the VW and MCC configurations are summarized in Figures 26(f)-(h). The MCC shows a decrease in the stiffness and strength compared to the VW decreased by 58.3% and 52.6%, respectively. The energy absorption is however increased by 317% in the case of the MCC configuration.

To explain the significant difference in the compressive stress-strain behavior, the measured mechanical deformation patterns of the VW and MCC structures are shown at different strain levels. As shown in Figure 27(a), the VW structure begins to fracture locally at the bottom layer when the strain reaches 5.7% (Figure 27(b) *A*). Failure initiates in the bottom layer and locally within the top layer when the strain increases to 6.3% (Figures 27(b) *B* and *C*). With the further release of strain energy, the fracture propagates, and the failure zone enlarges considerably when the compressive strain reaches 7.7% (Figure 27(b) *D*), followed by the structure breaking abruptly at 8.7% of strain (Figure 27(b) *E*). This deformation pattern indicates that the VW structure is relatively brittle, and it is not able to sustain large deformations characteristic of high energy-absorbing materials. Figure 27(c)

shows the deformation evolution of the MCC structure. The MCC configuration also fractures locally, however, the compressive strain has reached 10% by the time cracking is evident (Figure 27(d) *F*). The failure then propagates and expands to the whole MCC structure. It is worth noticing that most of the side holes fail at 14% of compressive strain (Figures 27(d) *G* and *H*). As the deformation progresses the structure begins to buckle at the bottom layer and engages contact between different layers. The middle layer fails at a global compressive strain of 28% (Figure 27(d) *I*). With further increase of the compressive strain, the cell walls in the MCC structure completely collapse and contact with each other, giving a rapid increase in stress at a compressive strain of 58% and gradually densifies towards the end (Figure 27(d) *J*). Compared with the VW structure, the MCC configuration features a more stable deformation pattern and exhibits a combination of ductile-like and brittle-like behavior under large deformations. The significantly different deformation patterns observed during the mechanical tests qualitatively explain the exceptional energy absorption of the MCC configuration.

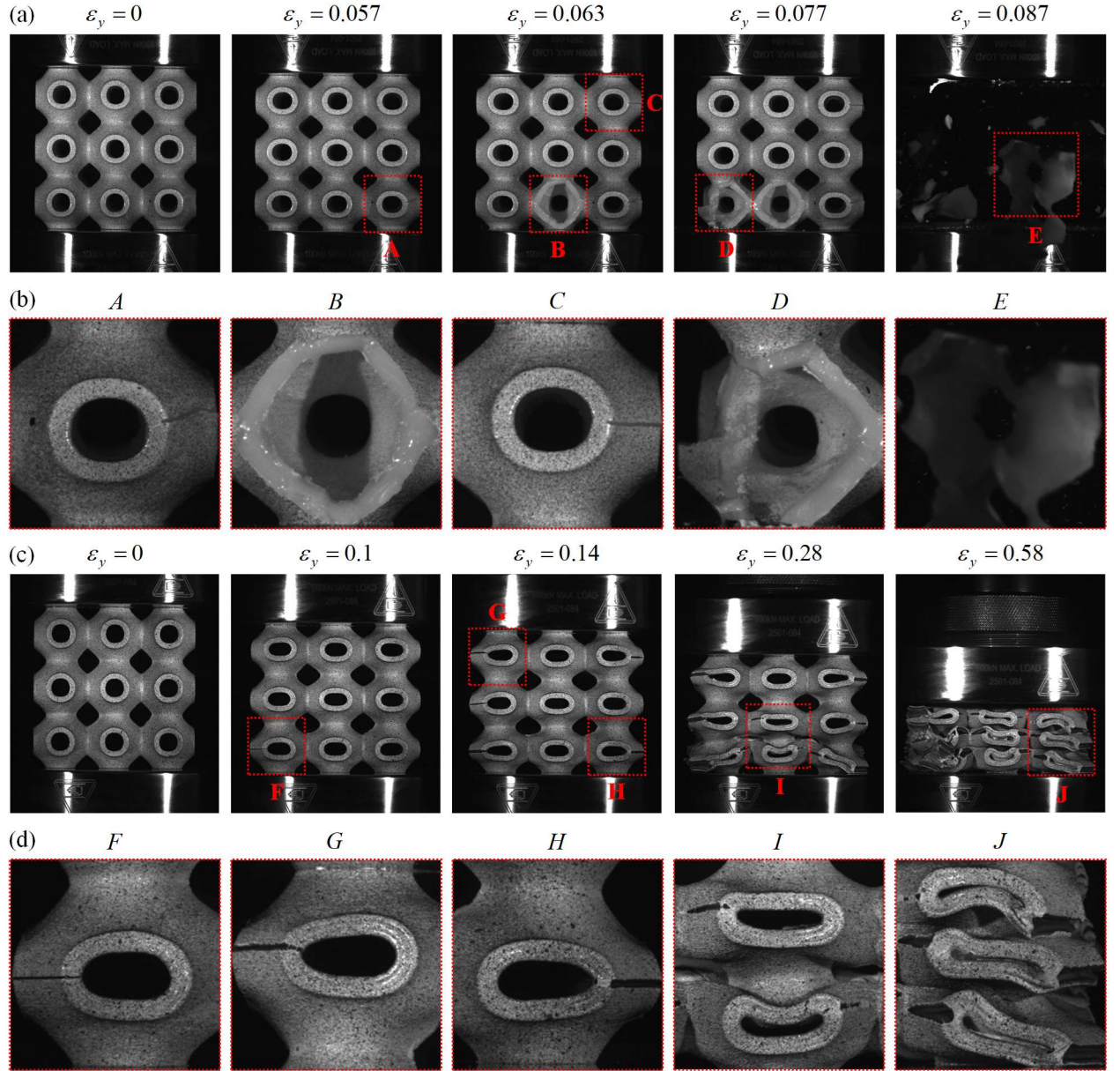


Figure 27 Mechanical deformation of the 3D printed VW and MCC structures (a) and (b) Global deformation and corresponding local deformation of 3D printed VW structure at different strain levels, respectively. (c) and (d) Global deformation and corresponding local deformation of 3D printed MCC configurations at different strain levels, respectively.

5.2.2.2. *Finite element simulations and DIC results*

To further understand the underlying deformation mechanisms related to these structures, finite element (FE) simulations have been performed on both the VW and the MCC structures. A user-defined viscoplastic model for the VeroWhitePlus and a hyperelastic model for Agilus30 have been implemented in a commercial finite element code (VUMAT/ABAQUS). Figures 28(a) and (d) show the comparison between measured and simulated stress-strain relations for the VW and the MCC structures, respectively. The experimental results and the FE simulations are in good quantitative agreement. Very good correlation is evident between experiments and simulations for the VW structure for strains lower than 8%. For the MCC structure, the two sets of stress-strain curves compare well for compressions lower than 10%. Furthermore, the large experimental deformation exhibited by the MCC structure also coincides very well with the FE simulation results for compressions lower than 40%. After this level of strain, the discrepancy between simulations and experiments begins to be significant as densification begins to occur. The main rationale behind the difference between experiments and simulations is the lack of incorporation of failure in the FE models. Nevertheless, the good agreement between experiments and simulations indicate that the FE modeling approach used here can predict the nonlinear mechanical behavior of the cellular structures within a sizeable compressive strain range.

Two-dimensional DIC measurements were also taken to identify the strain patterns of the two configurations during the mechanical testing. The experimental and simulated strain distributions at a global strain level of 5% for the VW structure are displayed in Figures 28(b) and (c). The FE simulations overpredict the magnitudes of the maximum

tensile and compressive strain concentrations. This is because the 2D DIC system used here may not be able to accurately capture the strain distribution in the complex surfaces. Nevertheless, the local strain measurements and the FE predictions are in good qualitative agreement, with distinctive thin horizontal bands of tensile strain near the center of each cell. It is noteworthy that the catastrophic failure of the VW structure (see Figure 27(a)) initiated due to cracks forming in the banded tensile strain region shown in Figures 28(b) and (c).

Figures 28(e) and (f) show the comparison between the DIC measurements and FE simulation results for the MCC structure at a global strain level of 5%. The MCC configuration does not feature the vertical strain concentrated in a small region, rather it is distributed evenly around the contact areas between unit cells along both the horizontal and vertical directions. The MCC configuration shows, therefore, a significantly more uniform stress distribution, suppressing rapid crack propagation and leading to a progressive failure behavior. Consequently, the MCC configuration exhibits the superior energy absorption capability under large deformations.

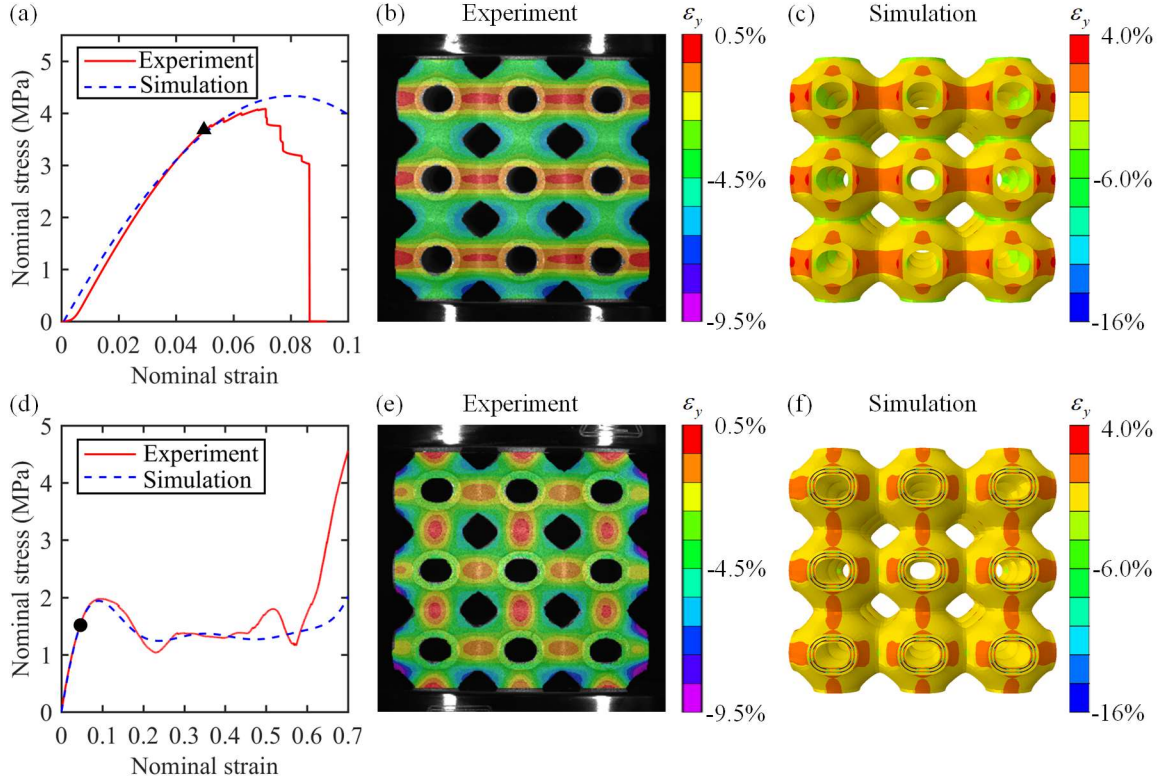


Figure 28 Digital image correlation (DIC) characterization and finite element (FE) modeling (a) Comparison of the stress-strain relations from the mechanical testing and the FE simulations for the VW structure. (b)-(c) Comparison between measured and simulated strain distributions for the VW structure. (d) Comparison of the stress-strain curves from experiments and FE simulations for the MCC configuration. (e)-(f) Comparison between measured and simulated strain distributions for MCC configuration. Here a common 5% of compressive strain is chosen for both the VW and MCC structures.

Digital Image Correlation (DIC) (Correlated Solutions, USA) has been used to capture the deformation and the strain distribution of the samples during compression tests. Figure 29(a) shows the DIC results for the VW structure at strains from 0 to 4%. With the progress of the compression test, a local thin band keeps its shape and position. The strain of the VW structure, therefore, accumulates in the local area, which then leads to the local stress

concentration. The MCC structure, however, features a more uniform distributed strain field as can be seen from Figure 29 (b). This feature is still present when the strain increases. One can even observe that the MCC architecture still exhibits a quasi-uniform strain distribution even when the structure begins to fail.

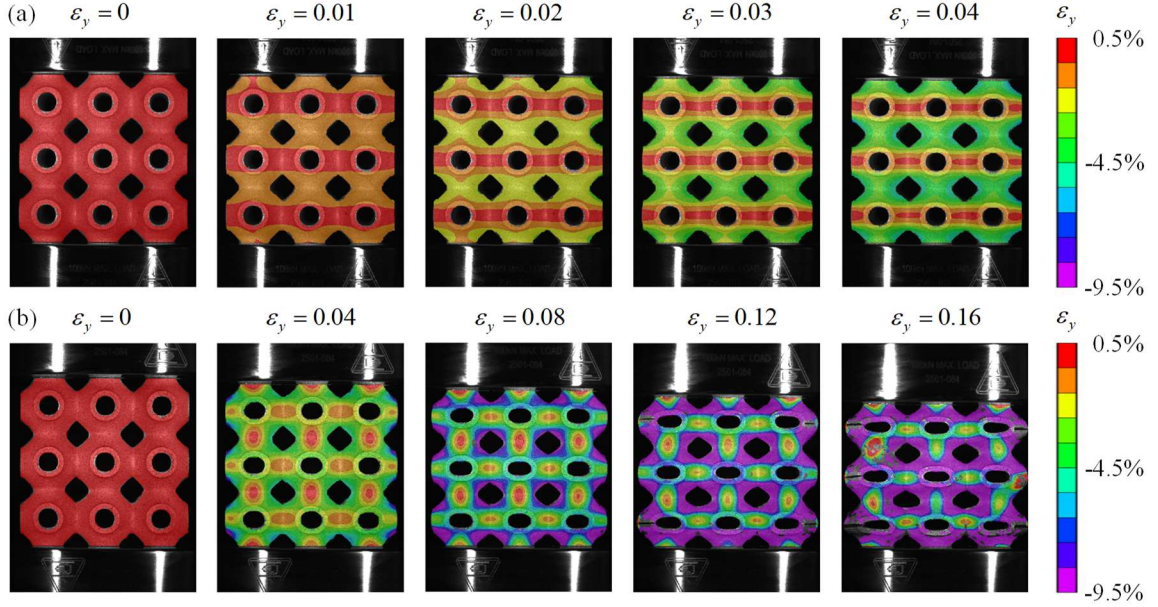


Figure 29 Measured strain evolution of the 3D printed samples (a) VW and (b) MCC structure.

The vertical strain distribution of the VW and MCC architectures from the FE simulations is shown in Figures 30(a) and (b), respectively. The simulated results are qualitatively consistent with those from the DIC at different strain levels. We also show the von Mises stress of the VW and MCC structures at different strains in Figures 30 (c) and (d). The von Mises stresses are concentrated at the local horizontal contact areas between unit cells for the VW configuration. The stress, however, is much more uniform around the sphere of the unit cell of the MCC structure. This further indicates that the MCC architecture has a highly efficient load transfer.

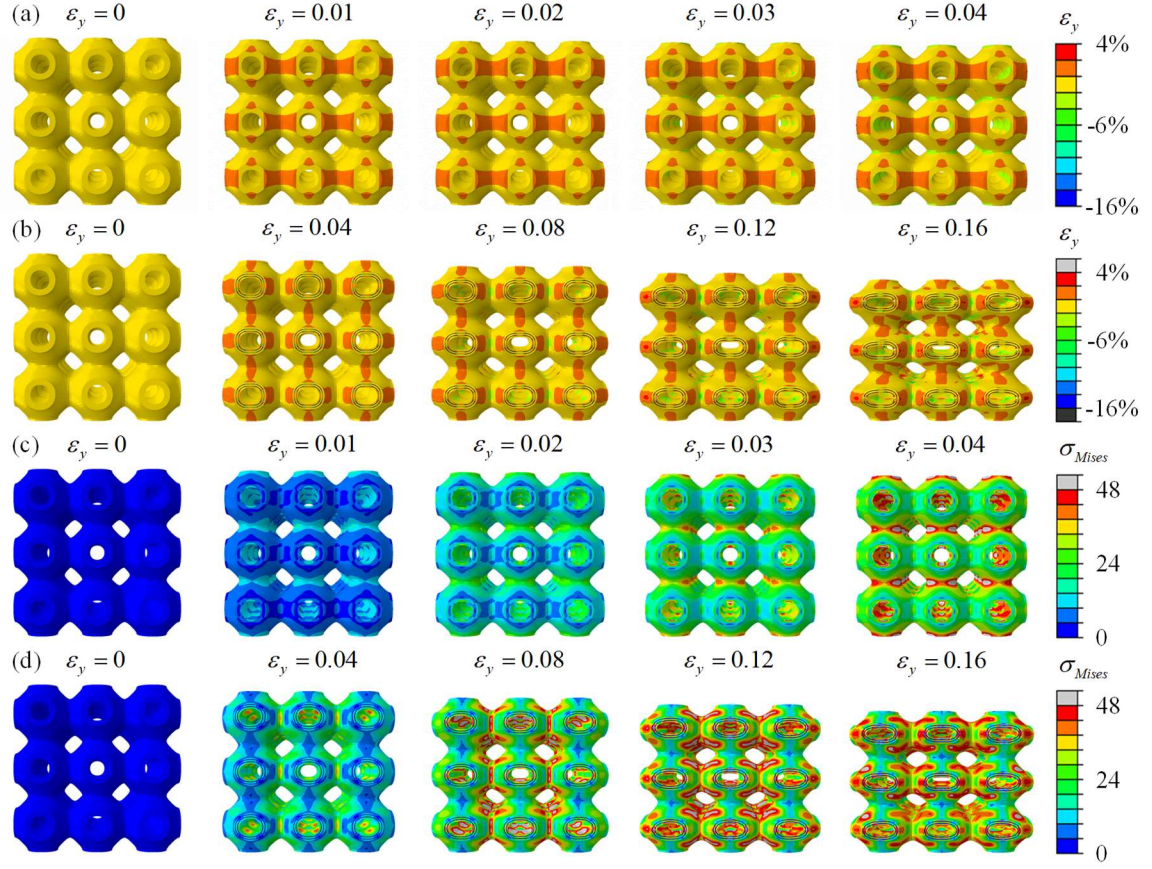


Figure 30 Simulated strain and von Mises stress evolution of the VW and MCC structures (a)-(b) Strain evolution of VW and MCC structures, respectively. (c)-(d) von Mises stress evolution of VW and MCC structures, respectively. The unit of von Mises stress is MPa.

5.2.2.3. Shape recovery under loading-unloading condition

Having explored the mechanical behavior and intrinsic deformation mechanisms of the MCC topologies, we proceed to study their structural integrity and shape recoverability. Cyclic loading tests on the MCC structures were performed for five cycles up to strains of 20% and 40%, respectively. Figure 31(a) shows the stress-strain relations of the MCC structure when compressed up to 20%. For the first cycle, the structure can fully recover its initial form (Figure 31(i)). Even when failure initiates and propagates, the structure can

recover to the initial shape gradually when unloaded. This behavior is due to the synergistic interplay between the multilayered architecture and the two compositions involved. The soft phase in particular acts like a spring between hard layers that absorbs the elastic energy during compression and releases the stored elastic energy when the load is removed.

To accelerate the cyclic tests, each compressed sample after the first cycle was heated up to 75 °C for 10 minutes. The samples can recover their initial form due to the shape memory effect of the VeroWhitePlus. The heated samples cooled down afterwards to room temperature in 30 minutes. Cyclic tests and shape memory assisted recovery were then performed on the samples at maximum compressible strains of 20% and 40%, respectively. Figure 31(b) shows that the effective stiffness of the MCC structure decreases with the number of cycles. This is because the fracture and failure zones increase and accumulate with the increase of the cycle number, similarly to the Mullins effect in porous solids [171]. For the 2nd, 3rd, 4th, and 5th cycles, the stiffness decreased by 23.8%, 25.9%, 29.6%, and 51.1%, respectively. Figure 31(c) shows the maximum stresses at different cycles. The maximum stress, in this case, decreases from the 1st to the 4th cycle but then increases between the 4th and 5th. This is because the failure zone enlarges with the increase of the number of cycles, and this lowers the first peak stress and postpones the maximum stress point to the subsequent densification range. The energy dissipation ratio, defined as the ratio between the area enclosed by the stress-strain curve divided by the area under the loading portion of the stress-strain curve for a given cycle, is plotted in Figure 31(d). The energy dissipation ratio slightly changes during the different cycles, but all are between 0.8 and 0.9, indicating that most of the energy input during the compressive loading phase is efficiently dissipated.

Figure 31(e) shows the stress-strain curve of the MCC configuration when compressed up to 40%. Once again, the MCC structure can recover its initial shape due to the same intrinsic deformation mechanisms (Figure 31(j)). The stiffness decreases quite remarkably from the 1st to 5th cycle by 42.7%, 67.9%, 97.1%, and 98.5%, respectively (Figure 31(f)). The reason for this rapid decrease is the generation of cracks and the enlarging of the failure zone accumulated in the structure with the increase of the number of cycles. The maximum stress shown in Figure 31(g) decreases by ~35% and then remains constant for the other cycles. Similarly, the energy dissipation ratio slightly decreases between the 1st and the 5th cycles with a stable value around 0.9, which indicates that the MCC structure is an excellent energy absorber (Figure 31(h)). These cyclic loading tests indicate that the proposed MCC configuration possesses excellent structural integrity and remarkable shape recoverability under large deformations due to the mutual bonding between hard and soft phases that can prevent catastrophic failure under compression. The compressive energy is partially dissipated by the viscoplastic deformation and fracture of the hard, brittle phase, while the soft phase, though only has a small fraction of the volume, can store considerable elastic energy. This stored strain elastic energy makes the soft phase act similarly to an elastic spring, which is essential for the shape recovery of the MCC structure during the unloading stage.

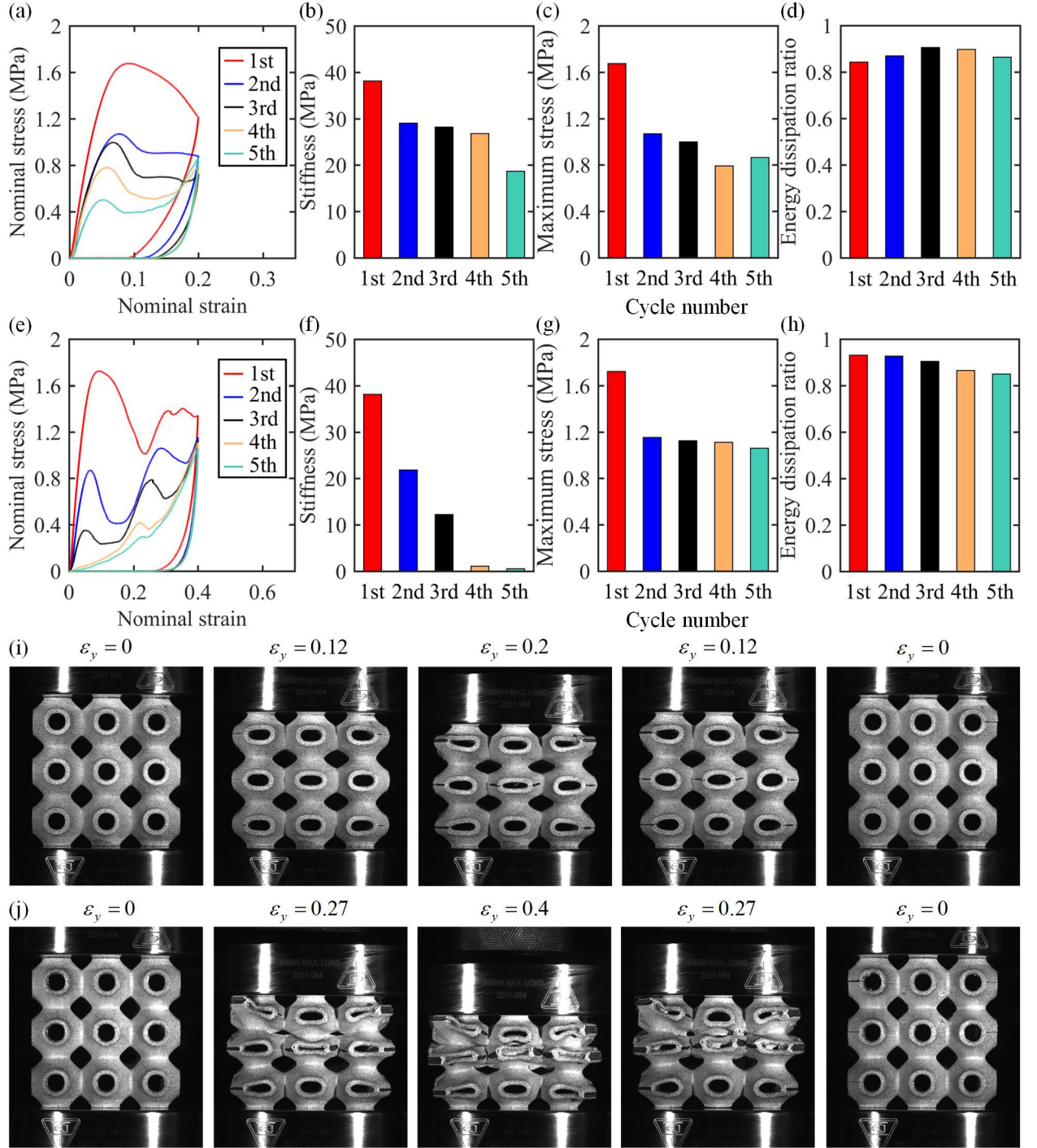


Figure 31 Mechanical properties of the MCC configurations under cyclic loading tests (a)-(d) Stress-strain curves, stiffness, maximum stresses, and energy dissipation ratios at different cycles when the structure is compressed up to 20%. (e)-(h) Stress-strain curves, stiffness, maximum stresses, and energy dissipation ratios at different cycles when the

MCC configuration is compressed up to 40%. (i)-(j) Deformation of the MCC structures at different strain levels when the MCC structure is compressed up to 20% and 40% after the first cycle, respectively.

5.2.2.4. Role of soft phase

It is clear that the soft phase in the MCC structures plays a pivotal role in the energy absorption and shape recoverability of these materials. To further quantify the role of the soft phase on the mechanical performance, study has been performed on the effect of soft phase volume fraction (V_f). Here four additional samples with soft phase V_f of 10%, 30%, 40%, and 50% have been designed, printed and compressed up to 70%. The stress-strain curve for each V_f is shown in Figure 32(a). Beyond the 10% of compressive strain, the stress drops rapidly for the MCC structure with $V_f=10\%$. In this case, the soft phase fraction is so small that it cannot absorb enough elastic energy, and this gives rise to a brittle-like deformation behavior. The onset of failure begins to occur at the corners of the structure at 15% of compressive strain (Figure 32(e)) and the top layer fails in a brittle mode at 25%. The failure zone then expands to the bottom layer and the whole structure when the strain reaches deformations of 40% and 50%. No obvious densification is present due to the subsequent catastrophic failure of the structure. With the increase of the volume fraction, the MCC structure exhibits a stable and progressive failure mode. For example, when the volume fraction of the soft phase increases to 0.5 the stress-strain curve shows a long and constant stress plateau between 5% and 60% of compression, followed by noticeable densification. This stress evolution indicates a progressive failure mode, as highlighted by the deformation patterns shown in Figure 32(f). No visible failure is present within the structure before 25% of compression, and the structure releases strain energy

through buckling instead of fracture due to the significant portion of the soft phase. The structure then fractures in a small portion of the volume while maintaining overall integrity at a strain of 40% and 50%.

The stiffness, strength and energy absorption of the MCC structures with various soft phase volume fractions are summarized in Figures 32(b)-(d). As expected, both stiffness and strength decrease with the increase of the soft phase volume fraction. The energy absorption increases only slightly when the volume fraction changes from 0.1 to 0.2, and this is attributed to the different failure modes present in the two different MCC structures. The energy absorption decreases significantly when the volume fraction increases up to 0.5 to a final value of 0.26 MJ/m^3 , which is comparable to the energy absorption exhibited by the VW structure (0.27 MJ/m^3). This indicates that when the volume fraction of the soft phase exceeds 0.5, it is not possible to obtain further energy absorption increases because of the decreases in stiffness and strength.

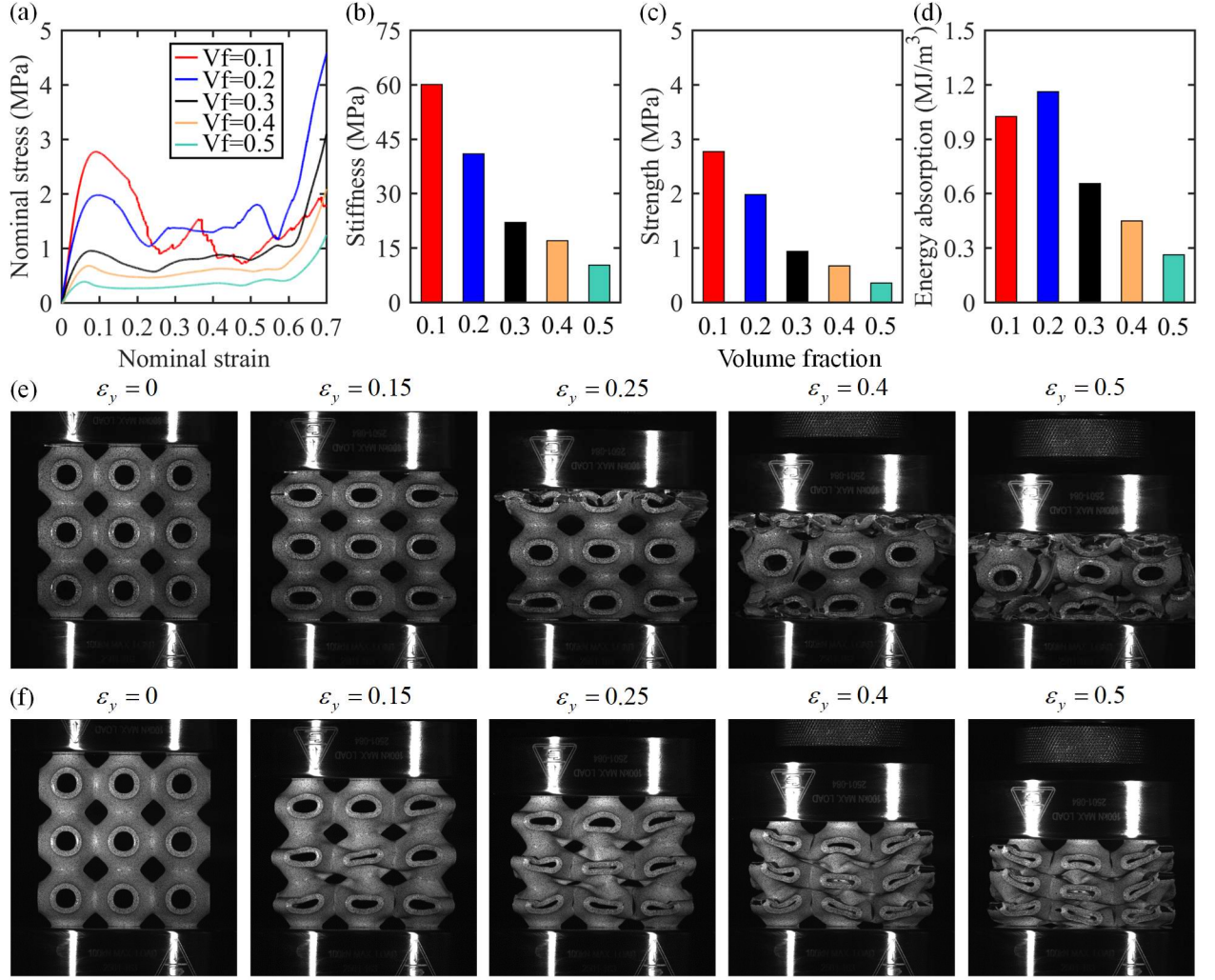


Figure 32 Effect of the volume fraction of the soft phase on the mechanical response of the MCC structures (a)-(d) Stress-strain curves, stiffness, strength, and energy absorption at different volume fractions, respectively. (e)-(f) Deformation patterns of the MCC structures with a soft phase volume fraction of 10% and 50%, respectively.

5.3 Conclusions

In summary, this paper presents the investigation of the mechanical response of a new type of 3D printed, bioinspired, cellular composite through a combined experimental and numerical effort. Compressive mechanical tests carried out on the 3D printed VW and MCC structures suggest that the multilayered architecture used in this work can turn a

structure possessing an original brittle, catastrophic failure mode into one featuring a progressive failure with enhanced energy absorption capabilities under large deformations. Finite element simulations along with 2D DIC measurements reveal that the mutual constraint and interaction between the two material phases, along with the microstructure of the MCC structure, are responsible for this enhanced mechanical performance. In addition, the MCC structures exhibit excellent and remarkable shape recoverability under a compressive strain up to 40 %, which is ascribed to the synergistic interplay between the two phases in the multilayered architecture. The enhanced energy absorption of the proposed cellular composites makes them ideal candidates for structures whose designs are controlled by crash or impact load cases. The remarkable shape recoverability is a feature that could be used to design novel morphing structures and soft robotics devices. Nevertheless, increasing energy absorption is often accompanied by a reduction of stiffness or strength. This issue can be remediated by using topology optimization or machine learning algorithms to optimize the balance between energy absorption and stiffness or strength. Although the 3D printed system evaluated in this work has features at the millimeter scale due to the resolution of the additive manufacturing equipment used, the design principles and the working mechanisms are transferable to other architected cellular materials across multiple length scales. The findings discovered here can be used as useful guidelines to novel develop lightweight composite architectures for various energy absorption engineering applications in automotive, aerospace vehicles, personal protective structures in sports, and lightweight package materials for the semiconductor and energy industry.

CHAPTER 6

PIEZOELECTRIC COMPOSITES WITH MULTIFUNCTIONALITIES AND TOPOLOGY OPTIMIZATION

6.1 Introduction

Materials and structures having energy absorbing capability find broad applications ranging from personnel protection to impact mitigation in militaries [172-175]. Structural components in these applications are often subjected to extreme loading conditions such as transient shock, vibration, and other dynamic loads. Without sufficient protection, these undesired dynamic loads would cause injury to the occupants and damage of structural components [176-178]. This triggers the critical need to develop innovative energy-absorbing materials for mitigating impact induced damage [179-181]. Traditionally, energy-absorbing materials were developed by exploiting intrinsic energy dissipation mechanisms, such as fragmentation in ceramics, viscous losses in polymers, and plastic deformation in metals [182-184]. However, due to the inherent randomness, how to accurately control the pore size, distribution of foams is still challenging, which is a substantial obstacle to ensure the stability of energy absorption. In contrast, architected materials have shown improved energy-absorbing capacity than their bulk counterpart through the interplay between designed architectures and base materials [174, 185].

An intuitive yet logical approach to fulfill this multifunctional need is to create composite materials composed of the energy-absorbing phase and impact-sensing phase. Piezoelectric

composites, which can generate electric signals upon impacts by the piezoelectricity of its piezoelectric fillers and consume the imposed mechanical energy by the viscoelasticity of its polymeric matrix, have been considered as a desired candidate for the advanced multifunctional materials. However, the performance of conventional 0-3 and 1-3 hybrid piezoelectric composites is restricted by the random distribution of the spatial discontinuous particles and fibers, respectively, which renders poor stress transfer efficiency from the surrounding polymeric matrix to the active piezoelectric fillers [76, 77]. As a result, the energy-absorbing capability and piezoelectric response of these piezoelectric composites are quite limited. A proper combination of the two disparate constitutive materials will enable the design of multifunctional composites with exceptional energy dissipation behavior, considerable mechanical flexibility, and high piezoelectrical sensitivity simultaneously. Recent studies indicate that introducing bi-continuous architectures to piezoelectric composite is an alternative way that can fulfill this multifunctional need [186-188].

Here, we proposed a three-dimensional (3-D) interpenetrating-phase piezoelectric composite (IP3C) composed of interconnected piezoelectric PZT ceramic scaffold and a polymeric matrix that can efficiently dissipate mechanical energy and simultaneously monitor the impact loadings. In an IP3C, each constituent phase completely interpenetrates through the composite microstructure in all three dimensions and contributes to the overall composite properties. As a result, the desired mechanical and piezoelectric properties are provided by the constituent phases and interfaces in a synergistic manner. In addition, since each phase in an IPC is continuous, the structural integrity will be retained by the remaining phases even after one phase is damaged or removed during multiple cycles. Therefore, the

proposed IP3C possesses a stronger energy-absorbing capability associated with a distinct perception function.

Moving toward architected materials, the proposed piezoelectric composites achieve significant enhancement with respect to piezoelectric sensing and energy absorption. However, the current research is mainly concentrated on the experimental investigation, which adopts trial-and-error approach to design the piezoelectric composites. On the other hand, the piezoelectric performance and damping capacity are mutually exclusive. Increasing the volume fraction of one phase will result in the poor behavior of the other phase. In this sense, computational framework can be adopted to find the optimal volume ratio and morphology of the piezoelectric composite. Up to now, the optimization method includes homogenization method [189], simple isotropic material with penalization (SIMP) [190], evolutionary structural optimization (ESO) [191], level set method (LSM) [192], and machine learning (ML) method [193]. However, the homogenization method often produces designs with individual small pores in the structure that is usually unmanufacturable. ESO method uses a special criterion to assess the contribution of each element to the structure's behavior and remove those with least contribution. Therefore, this approach is essentially focused on the local consequences other than the global optimum. It is also typically computationally expensive. ML has attracted researchers recently, but this method depends heavily on the training data. Usually, large amount of training data is required and there is no mathematical prove that can guarantee the result from ML is the global optimal design. Notably, LSM is a versatile method to analyze the motion of an interface and following the evolution of interfaces, which can easily develop and merge holes [194]. Furthermore, the continuous of interface will render the smooth

boundary between different material phases. Based on level-set topology optimization method, some works have been done to optimize the piezoelectric composites [195-197]. However, level set-based topology optimization is difficult to implement when it comes to multiphysics problem. In this work, we use SIMP due to its simplicity.

6.2 3D piezoelectric composites with high energy absorption and sensing

6.2.1 Fabrication and structural characteristics

We fabricated the IP³C s using a facile camphene-templated freeze casting method, as shown in Figure 33. The fabrication processes consists of five main steps: (i) dispersing the synthetic PZT ceramic powders and additive organic materials (PS and Hypermer KD-4) in the molten camphene by magnetic stirring; (ii) freezing the prepared warm slurries in a water bath to create the frozen structure and then placing in a freezer to enhance the structural strength; (iii) sublimating the frozen camphene on sponge substrate; (iv) sintering the precursor in the alumina crucibles to yield the 3-D porous PZT ceramics. Meanwhile the additive organic materials (PS and Hypermer KD-4) are volatilized during this high-temperature sintering process; and (v) infiltrating the porous PZT ceramics with PDMS to form the PZT-PDMS composites. Noticeably, compared to the common ice template, which requires costly cryogenic temperature for fast solidification, camphene templated (melting temperature 44-48°C) can be rapidly solidified at room temperature with manageable shrinkage of ~3.1% [198, 199]. Furthermore, by introducing the oligomeric polyester dispersant (Hypermer KD-4) the PZT ceramic powders are homogenously dispersed in the slurry, while the added sufficient polystyrene (PS, 30 vol% to PZT) is to enhance the strength of the porous structures and obtain uniform pores during the frozen forming process [200].

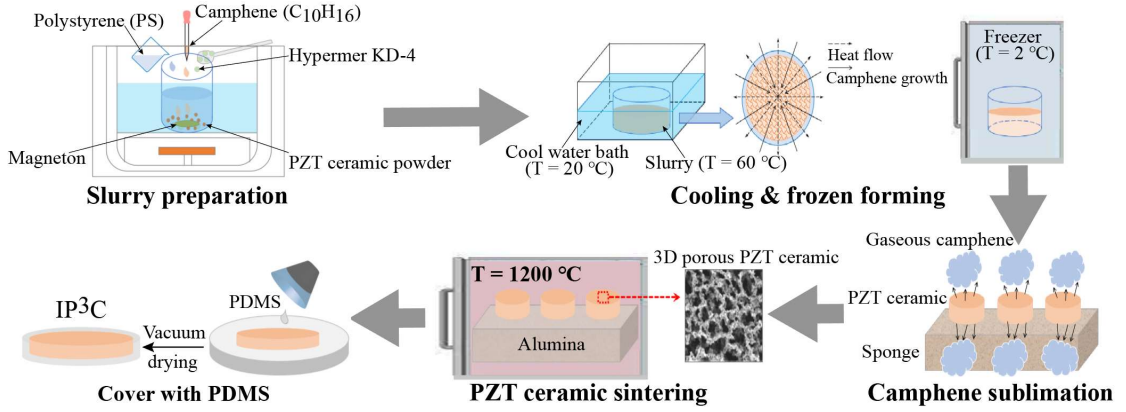


Figure 33 Diagram of the fabrication processes for the IP3C based on camphene-templated freeze casting.

The surface and cross-sectional scanning electron microscopy (SEM) images of the PZT ceramic skeleton are shown in Figure 34(a)-(b), which features the uniform and interconnected porous structures with an average pore size of $\sim 30 \mu m$. The inset of Figure 34(b) is the magnified SEM image of the PZT skeleton. Since the camphene and the additive organic materials (PS and Hypermer KD-4) would be sublimated and volatilized during the fabrication processes, the porosity (P) of the porous structured PZT ceramic skeleton is estimated by $P = (1 - PZT \text{ vol}\%)$. The energy dispersive spectroscopy (EDS) mapping (Figure 34(c)) confirms that the elements of zirconium, lead, titanium and oxygen are homogeneously dispersed in the skeletons with the composition of $[Pb(Zr_{0.52}Ti_{0.48})O_3]$. Figure 34(d) shows the X-ray diffraction (XRD) pattern of porous PZT ceramic after the final calcination process, where the apparent perovskite phase can be observed. The splitting peaks of (002) and (200) indicate the presence of a typical tetragonal phase in the porous PZT ceramic.

As illustrated above, the uncured polymeric PDMS was impregnated into the structured PZT ceramic skeletons to form the IP³C. Followed by the curing procedure of

the PDMS matrix, the PZT-PDMS composites were obtained, see Figure 34(e). The finger-bent specimen in Figure 34(f) displays the moderate flexibility of the IP³C. The final as-proposed IP³C for impact energy-absorbing and monitoring were finally obtained by cutting even around the PZT ceramic skeleton edges of the composites.

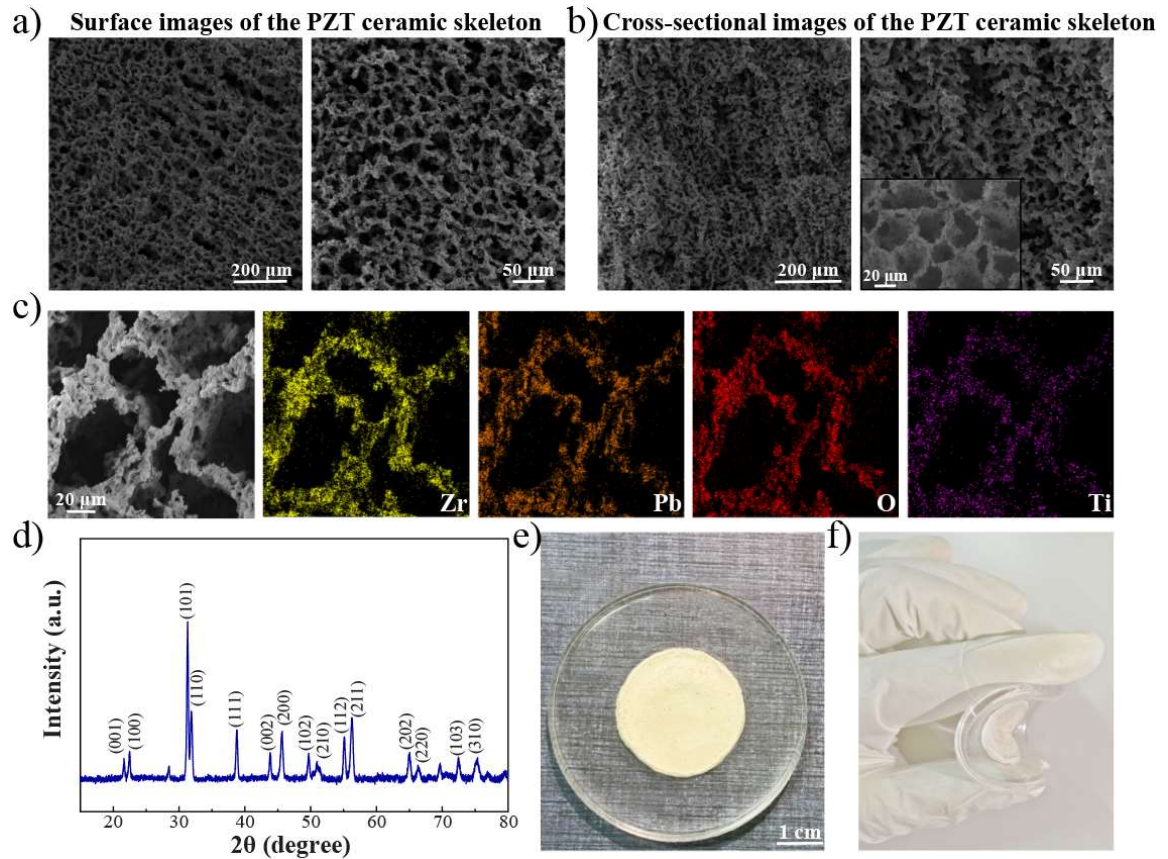


Figure 34 Structural characteristics of the as-fabricated 3-D interpenetrating-phase PDMS-PZT composites (a) The surface and (b) cross sectional SEM images of the 3-D structured PZT ceramic. (c) The EDS mapping analysis of the corresponding PZT skeletons. The elements of zirconium, lead, oxygen and titanium are homogeneously dispersed in the skeletons. (d) XRD diffraction spectra of the PZT ceramic skeletons. (e-f) Optical pictures of an as-prepared IP³C with good flexibility.

6.2.2 The experimental set-up for impact test and d_{33} measurement of the PZT-PDMS composites

For determining the piezoelectricity coefficient (d_{33}), colloidal silver paste (Ted Pella, Redding, CA) was coated on both surface sides of the PZT-PDMS composites, which can be solidified at room temperature. For the loading set-up, the bottom side plate was fixed to the frame and the loading force was applied by directly putting different weights on the top plate (Figure 35(a)). The generated charges were measured by an electrometer (Keithley, 6517B) and a testing circuit system based on LabVIEW software (Figure 35(b)).

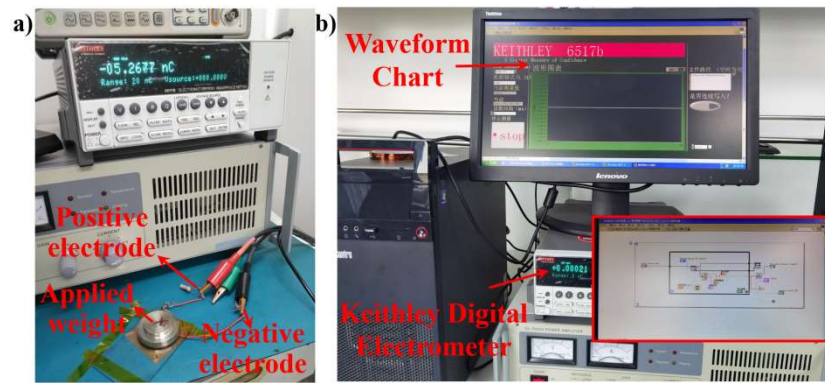


Figure 35 Experiment setup for piezoelectric coefficient measurement (a) The photo of the piezoelectric coefficient (d_{33}) measurement set-up and (b) the piezoelectric performance of the PZT-PDMS composites under cyclic loadings. The inset is the testing circuit of the LabVIEW software.

To illustrate the piezoelectric sensitivity and energy-absorbing capability of the 3-D PZT-PDMS composites, the pendulum impact tests were carried out on an electronic IZOD impact tester(XJUD-5.5) with an impact speed of 3.5 m s⁻¹. The testing produces are as follows:

Firstly, the surfaces on both sides of the 3-D interpenetrating-phase PZT-PDMS composites were coated with the colloidal silver paste (Ted Pella, Redding, CA) with a thickness of 4 mm and a width of 10 mm. Then, the composite specimens were clamped by two insulative plates with an exposing length of 25 mm and connected to an electric signal measurement system composed of a charge amplifier and oscilloscope.

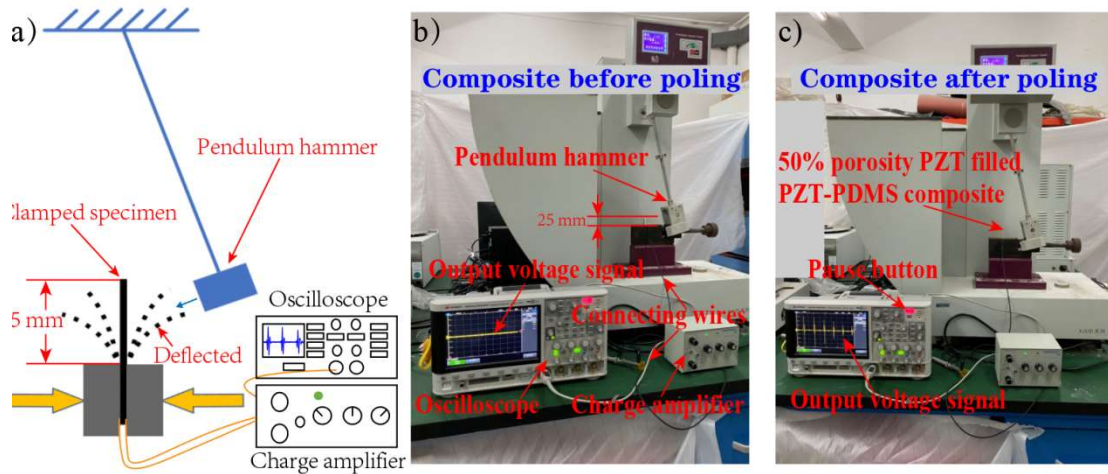


Figure 36 Experiment setup for impact test (a) The schematic of the testing set-up. The photos of the 3-D PZT-PDMS composites under the pendulum impact test using electronic IZOD impact tester (b) before and (c) after electric poling. When taking these photos, the pause button of the oscilloscope was pressed and the pendulum hammer of the impact tester was fixed.

Thirdly, the cyclic impact loading was applied by a free-falling pendulum hammer.

Finally, during the testing, the electric signal outputs were recorded by the oscilloscope, while the absorbing energy of the composites under the first impact was directly read from the impact tester.

Figure 36(b)-(c) display the piezoelectric responses of the 3-D interpenetrating-phase PZT-PDMS composites before and after electric poling. In Figure 36(b), due to the absence of effective polarization of PZT ceramics within the PDMS matrix, the composites show low output voltage before electric poling treatment. In the case of the composites after poling (Figure 36(c)), the dipole moments of the PZT filler are aligned. As a result, more significant output voltage signals are generated.

6.2.3 Experimental energy-absorbing behaviors

To experimentally characterize the advantages of the as-fabricated IP³C in the mechanical energy dissipation, the energy-absorbing behaviors were systematically examined under both quasi-static and dynamic loading conditions. Here, for a fair comparison, the tested IP³C and the corresponding non-structured 0-3 hybrid composite have the same volume percentage of the PZT ceramic filler (50% porosity of the structured PZT skeleton to 50 vol% of filled PZT powders). Here, for fair comparison, we also tested the performance of non-structured 0-3 hybrid composite with the same volume percentage of the PZT ceramic filler (50% porosity of the structured PZT skeleton to 50 vol% of filled PZT powders).

Figure 37 displays the quasi-static loading-unloading stress-strain curves of the PZT-PDMS composites at 5% (solid line) and 10% (dashed line) strain, respectively, in which the hysteresis effect of the composite can be manifested by the stress-strain hysteresis loop. From the plots, it is evident that the proposed IP³C exhibits much more detectable circumscribed areas in the stress-strain hysteresis loop when compared to the corresponding non-structured 0-3 hybrid composite. This indicates that the hysteresis effect of the PZT-PDMS composite has been dramatically enhanced by the interpenetrating

architecture of the structured PZT ceramic and PDMS matrix. The inset of Figure 37 schematically illustrates the characteristic mechanical energy dissipation and storage of the composite hysteresis effect at each loading-unloading cycle, which provides an insight into the deformation processes of the composite. The result reveals that the 3-D interpenetrating-phase feature is beneficial for generating substantial consumption of the imposed mechanical energy in the composite, which could be attributed to the structured PZT filler permitting effective stress transfer within each phase for the enhancement of material internal friction. In that case, the imposed mechanical energy can be additionally consumed by the mechanisms beyond merely viscous loss in the polymeric PDMS matrix, in particular, involving the strong two-phase interaction during the cyclic loading-unloading conditions. Furthermore, due to the flexibility of the polymeric matrix, the integrity and continuity of the structured PZT ceramics are ensured with adequate shape recovery inside the composite.

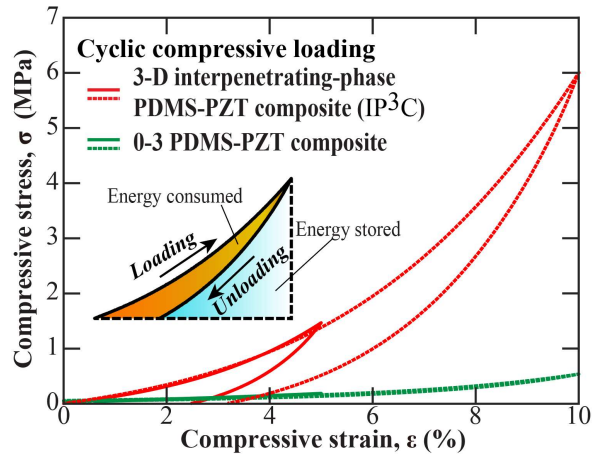


Figure 37 “Quasi-static” unidirectional loading-unloading stress-strain curves of the IP3C and the corresponding non-structured 0-3 PZT-PDMS composite at 5% (solid line) and 10% (dashed line) strain, respectively. The inset illustrates the characteristic in the energy

dissipation and storage during the deformation process at each loading-unloading cycle of the composite material.

To understand the enhanced performance of the proposed 3-D interpenetrating-phase composite materials permitted by the structured PZT fillers for energy dissipation, finite element simulations were performed on representative volume elements of interpenetrating-phase composite (Figure 38 (a)). The finite element package (Abaqus, Providence, USA) was used for the simulation, the coupled mechanical and electrical problem was implemented by defining the piezoelectric element in the software. In the simulations, isotropic elastic constitutive model was used for both PZT ceramic phase and PDMS polymeric matrix phase. The von Mises stress contours of PZT ceramic phase of the randomly distributed 0-3 PZT-PDMS model with 30 vol% PZT powders and 3-D interpenetrating-phase PZT-PDMS model with the same volume fraction of 30% (corresponding to the porosity of 70%) at different compressive strains are shown in Figure 38(b) and (c), respectively. It can be found that within the IP³C, the Mises stress is uniformly concentrated on the PZT skeleton compared with the randomly distributed PZT-PDMS model. The stress in structured PZT spreads much more efficiently than random PZT model. However, for the randomly distributed PZT-PDMS model, the stress is mostly concentrated in the connected PDMS phase. This indicates the superior efficient stress transferability within the structured PZT skeleton and the potential high energy dissipation capability within the proposed IP³C, which are in good agreement with the experimental analysis.

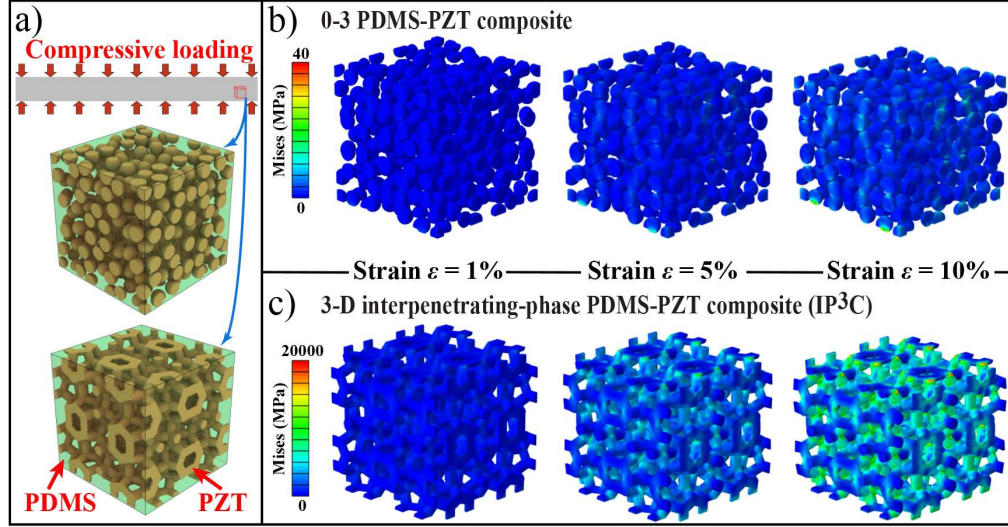


Figure 38 Simulated mechanical response of the PZT-PDMS composites under compression (a) Geometric model of randomly distributed PZT-PDMS composite and IP³C. Mises stress contour of PZT-PDMS composites with (b) 30 vol% PZT powders and (c) 3-D interpenetrating-phase PZT-PDMS model with the porosity of 70% at a compressive strain of 1%, 5% and 10%, respectively.

To examine energy-absorbing behaviors of the IP³C under dynamic loading conditions, the storage and loss moduli of both non-structured 0-3 PDMS-PZT composite and IP³C were measured by using a dynamic mechanical analyzer at a constant strain of 0.5%. Figure 39(a) displays the storage (G') and loss (G'') moduli of the tested composites as a function of loading frequencies (1Hz, 5Hz, 10Hz and 20Hz) at room temperature 25 °C. As the storage and loss moduli measuring the stored energy and the dissipated energy during the deformation processes of materials, respectively, the plots clearly indicate the exceptional energy storage and dissipation capability of the PZT-PDMS composite with 3-D interpenetrating-phase compared to the corresponding 0-3 hybrid composite. That reveals the fact that the 3-D architected ceramic filler playing a critical role in promoting

good damping capacities while ensuring potent mechanical energy storage by rendering highly effective load transfer throughout the composite. This finding agrees with our hypothesis that the interpenetrating architectures of the proposed IP³C is beneficial for generating essential energy storing and dissipating abilities in the PZT-PDMS composite by effective stress transferability. To be noticed that the slight increase of storage (G') and loss (G'') moduli with the loading frequencies is typical properties for polymers and their composites.

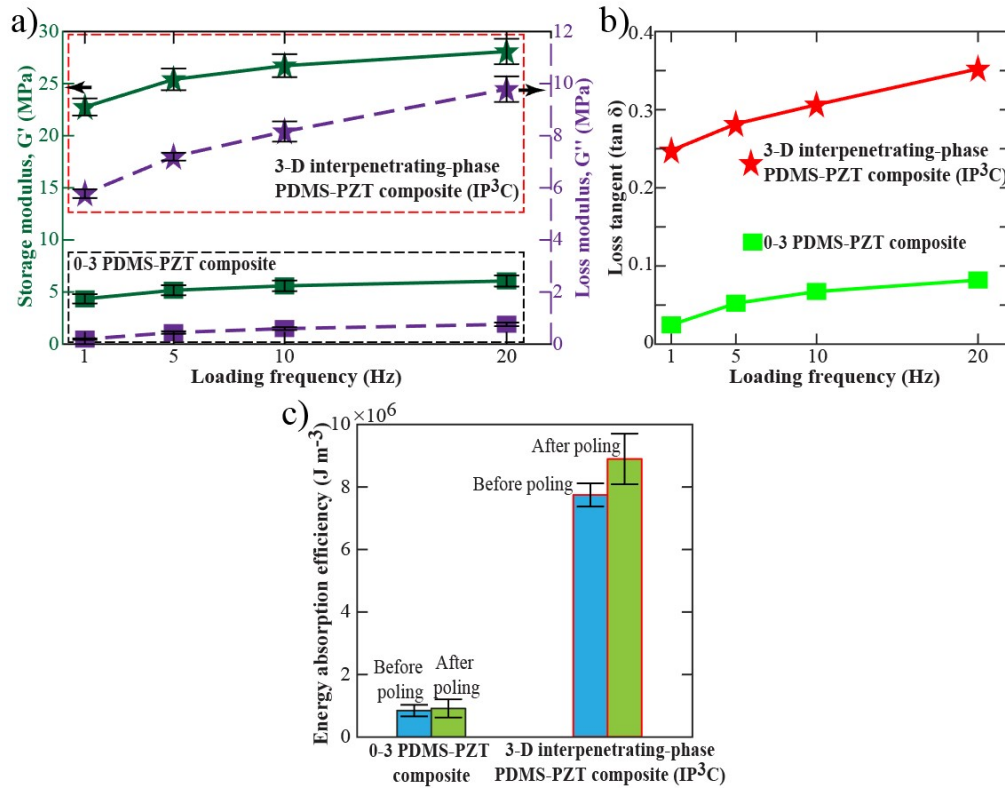


Figure 39 Experimental mechanical characterizations of the PZT-PDMS composite under dynamic loading conditions (a) The comparison of the dynamic storage (G') and loss (G'') moduli of the composites under different loading frequencies. (b) The corresponding material loss factor ($\tan \delta$) of the composites. (c) The energy absorption efficiency of the IP³Cs fabricated from different porosity of structured PZT ceramic fillers during the

pendulum hammer impact. Connected lines are guides for eyes. Error bars indicate standard deviations from 5 independent measurements.

Figure 39(b) shows the material loss factor ($\tan \delta$) of the PZT-PDMS composite as a function of loading frequencies, which is the ratio of the loss (G'') modulus to storage (G') modulus ($\tan \delta = G''/G'$) for measuring damping performance in an energy-absorbing material. It can be seen that the IP³C presents a significantly higher loss factor ($\tan \delta$) than that of the corresponding 0-3 hybrid composite. Specifically, at 1 Hz loading frequency, the $\tan \delta$ of the composite with 50% estimated porosity of the structural PZT filler is 0.246, which is 10 times higher than that of 50 vol% randomly distributed PZT powders filled composite ($\tan \delta=0.023$). As the loading frequency reaching 20 Hz, the IP³C shows a loss factor up to 0.35, which is much higher than traditional metals, polymers, composites and most foam and elastomers. Similar to experimental analysis of “quasi-static” loading case, this is believed to result from the synergistic mechanisms of mechanical energy dissipation, leading to remarkably increased damping capacities of our proposed IP³C. We also characterized the energy-absorbing capability of the proposed IP³C under practical impact loading by conducting a pendulum impact test using an electronic IZOD impact tester with an impact speed of 3.5 m s⁻¹. As shown in Figure 39(c), the PZT-PDMS composite with 3-D interpenetrating-phase exhibits much better energy-absorbing efficiency ($\sim 7.71 \times 10^6$ J m⁻³) compared to that of the corresponding 0-3 hybrid composite with random distributed PZT powder ($\sim 0.84 \times 10^6$ J m⁻³). This outstanding energy-absorbing efficiency of the IP³C can enhance the impact resistance for crucial structure protection by impact damage mitigation and vibration elimination. Interestingly, after electric poling treatment, the damping effect of the 3-D interpenetrating-phase composite becomes more pronounced

($\sim 8.89 \times 10^6 \text{ J m}^{-3}$), which indicates that the structured PZT ceramic exploits its piezoelectric feature for the effective conversion of mechanical energy to electrical energy. The additional energy dissipation route of piezoelectricity helps remove imposed mechanical energy from vibrating structures, necessarily resulting in improving the structural damping performance.

6.2.4 The experimental set-up and method of the d_{33} measurement of the PZT-PDMS piezoelectric composites

For determining the piezoelectricity coefficient (d_{33}), colloidal silver paste (Ted Pella, Redding, CA) was coated on both surface sides of the PZT-PDMS composites, which can be solidified at room temperature. For the loading set-up, the bottom side plate was fixed to the frame and the loading force was applied by directly putting different weights on the top plate (Figure 40(a)). The generated charges were measured by an electrometer (Keithley, 6517B) and a testing circuit system based on LabVIEW software (Figure 40(b)).

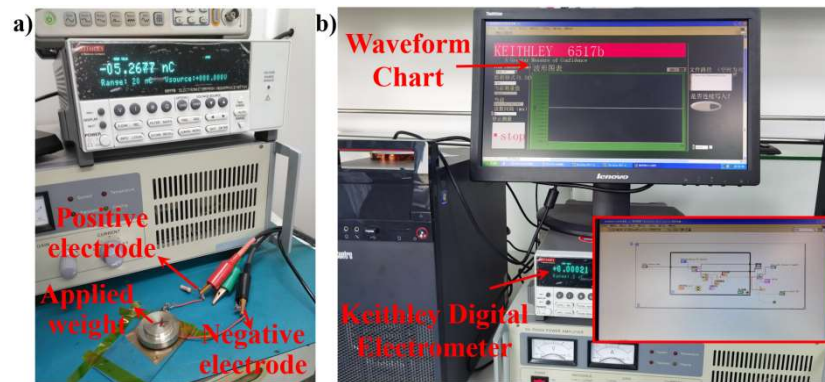


Figure 40 Experiment setup for d_{33} measurement (a) The photo of the piezoelectric coefficient (d_{33}) measurement set-up and (b) the piezoelectric performance of the PZT-PDMS composites under cyclic loadings. The inset is the testing circuit of the LabVIEW software.

It should be noticed that we used this “putting-weight” method to test the piezoelectric response (d_{33}) of the PZT-PDMS piezoelectric composites instead of commercial d_{33} meter. The reason is that during the measuring process of the commercial d_{33} meter, the specimen is point-to-point fixed using the meter’s probes with a static preload and this clamping characteristic is not suitable for flexible piezoelectric materials, in which the gravitational force will deform the flexible piezoelectric materials using this point-to-point clamping method and the applied force cannot be uniformly applied to the flexible material by the point loading. Furthermore, the piezoelectric charge coefficient relates the electric charge generated with an applied mechanical force and is expressed in the unit of Coulomb/Newton (C/N). In our work, we tested the piezoelectric coefficient by gently putting weight on the top surface of the IP³C specimen as the applied load and using a programmable digital electrometer (6517B, Keithley) to measure the generated charges. In this method, the mechanical force can be directly calculated from the applied weight, while the generated charge can be accurately measured from the digital electrometer. Therefore, this “putting-weight” method is good for the measurement of the piezoelectric coefficient of the flexible piezoelectric composite in our work.

6.2.5 Impact loading monitoring

Due to the piezoelectric effect of the PZT ceramic component, the proposed IP³C also exhibits a unique electro-mechanical response compared with other traditional energy-absorbing materials. This makes the proposed IP³C not only has excellent damping behaviors but also has potential applications in impact sensing.

After electric poling treatment, the piezoelectric performances of the PZT-PDMS composites were measured under different compressive loadings. The load was applied by

gently putting weight to the top surface of the composites. The output charge was recorded from a digital electrometer and plotted in Figure 41(a). Upon a ~ 1 N compressive loading, the measured piezoelectric charge was ~ 154 pC, while ~ 2.5 N compression could generate ~ 356 pC piezoelectric charge from the IP³C with 50% porosity of structured PZT skeleton. The almost linear relation between the generation of electric charges of the composites and the applied loading force guarantees the potential applications of the 3-D PZT-PDMS composites in exact force sensing. Figure 41(b) shows the piezoelectric coefficient (d_{33}) of the composites which is determined from the slope of the output charge vs. applied force curves. The piezoelectric coefficient (d_{33}) of the IP³C is first increased from ~ 87 pC N⁻¹ to ~ 146 pC N⁻¹ with the porosity of structured PZT ceramic from 30% to 50%. The enhanced piezoelectric performance is due to the softer material can help to localize the external mechanical stress on the piezoceramic structure, resulting in higher piezoelectric output (i.e., smaller loads required to strain the material) [201]. However, when the porosity of the PZT ceramic filler reaches 60% and 70%, the piezoelectric coefficient d_{33} of the composites shows an obvious drop to 77.39 pC N⁻¹ and 60.59 pC N⁻¹, respectively. That may be because the porosity reduces the fraction of the active piezoceramic, leading to the lower polarization. Despite this, the piezoelectric coefficient d_{33} of the IP³C is still 7 times higher than that of PZT powders filled 0-3 composite (Figure 41(c)). For instance, the piezoelectric coefficient d_{33} of the non-structured 0-3 PZT-PDMS composite with 50 vol% PZT ceramic is ~ 20 pC N⁻¹, which is 7 times lower than the IP³C with the same PZT percentage. This is believed to result from the imposed mechanical energy that can be effectively transferred to the piezoelectric component through the polymeric matrix by using the 3-D interpenetrating-phase structure of PZT and PDMS.

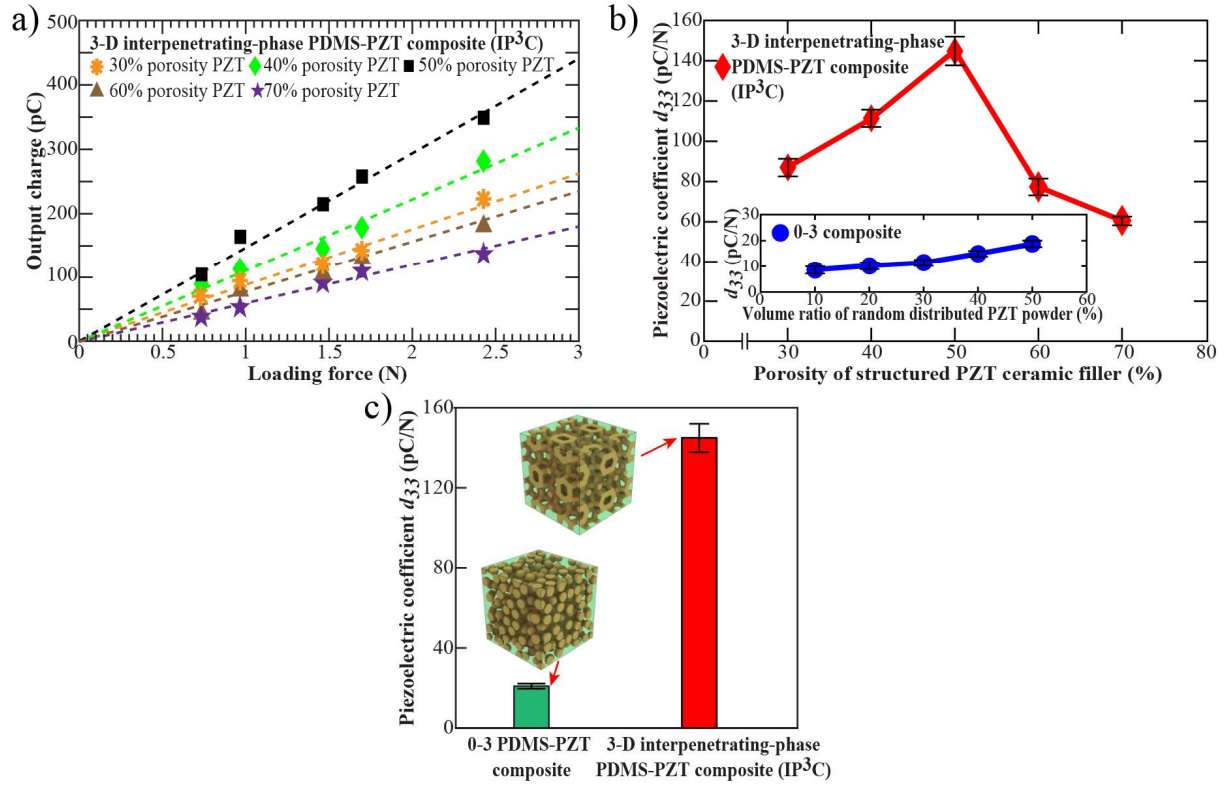


Figure 41 The experimental piezoelectricity of the IP³C (a) The charge vs. loading force plot for piezoelectric coefficient (d_{33}) measurements. (b) The plot of the measured d_{33} for the IP³Cs with different porosity of structured PZT ceramic fillers. Inset is the corresponding non-structured 0-3 PZT-PDMS composites with randomly dispersed PZT powders. Error bars indicate standard deviations from 5 independent measurements. (c) The comparison of piezoelectric coefficient (d_{33}) between our IP³C and its counterpart conventional 0-3 PZT-PDMS composites.

To further investigate the prominent piezoelectric response of the IP³Cs, numerical simulations were performed on representative volume elements with the structured PZT phase, as shown in Figure 42. In the simulations, the isotropic elastic constitutive model with the polarization direction along compressive loading was used for the PZT phase and the bottom surface potential was set to zero. Because of the intrinsic property of the

piezoelectrical phenomenon, stress plays a major role in the piezoelectric response. As expected, the electric potential output of the randomly distributed PZT-PDMS model (Figure 42(a)) is far less than the IP³C (Figure 42(b)). This concludes the superior performance of piezo-response of the structured PZT-PDMS composite.

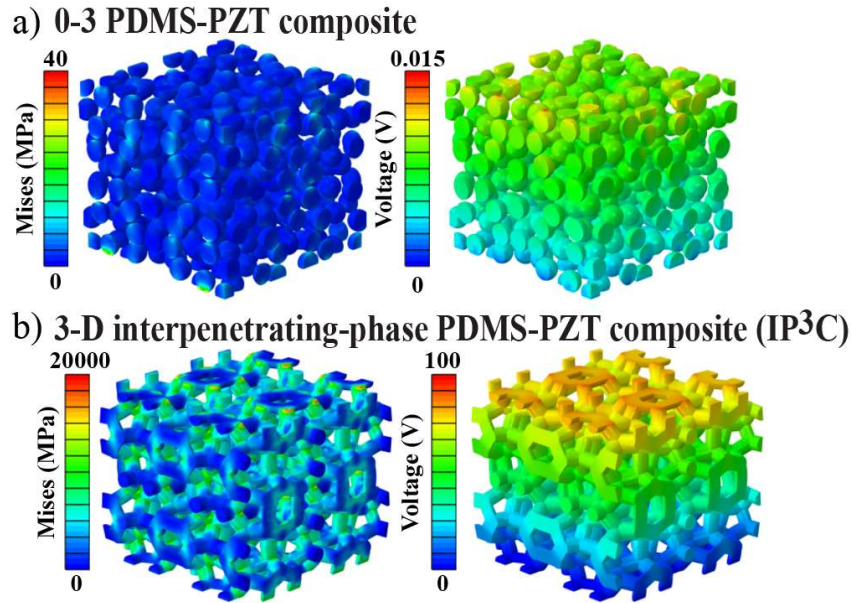


Figure 42 The simulated electric potential of piezoelectric composites (a) IP³C compared to (b) the corresponding non-structured 0-3 composite.

For the potential impact sensing applications, we cyclically put a 100 g weight (loading force ~ 1 N) under low and high frequencies at 50 mm and 30 mm height from the surface of the composite, respectively. In Figure 43(a), the accumulated charge has an immediate rise and fall in response to the mechanical stress along with a small change during the loading and release states. From the plot, it should be noticed that the output charge is higher than 200 pC when we dropped 100 g weight from 50 mm height (~ 1 N loading force), while the measured d_{33} of the composite with 50% porosity PZT ceramic is around 146 pC N⁻¹. That is because the composite suffered from an impact loading with an

acceleration-g, and the lost gravitational potential energy of the weight is directly transferred to the composite over a very short time. Importantly, as we lowered the height of the heavy object, the applied impact force was reduced and the charge generation of the composite was correspondingly reduced. Thus, it is confirmed that the developed 3-D interpenetrating-phase PZT-PMDS composite can be used as an impact sensor for damage predictions.

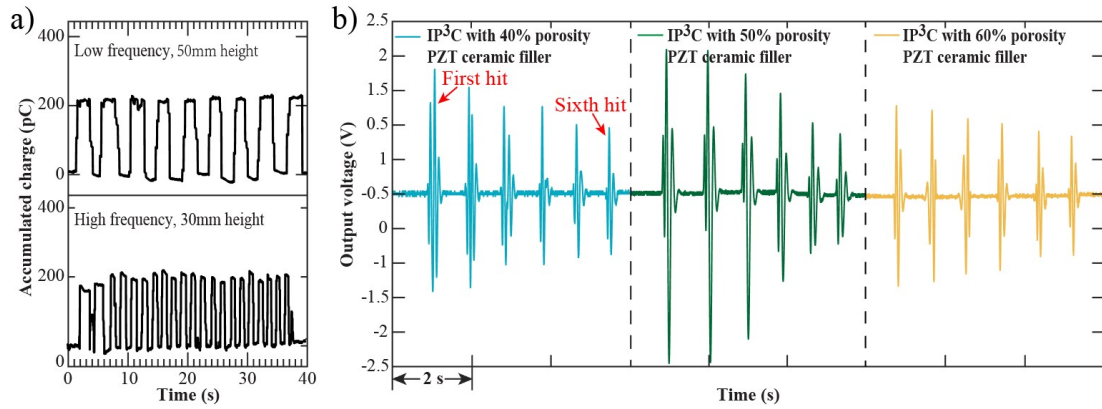


Figure 43 The electro-mechanical responses of the IP3C for the potential applications in impact sensing and energy harvesting (a) The real-time cyclic charge accumulation and dissipation profiles for the IP³C with ~50% porosity of structured PZT filler using a 100g weight. (b) The potential applications of the IP³Cs with different porosity of structured PZT ceramic fillers after poling for pendulum hammer impact loading sensing and absorbing.

Moreover, pendulum impact tests were also performed to illustrate that an exceptional combination of energy-absorbing capability and impact sensitivity has been achieved by the proposed IP³Cs. The composite specimens were clamped by two insulative plates in the pendulum impact test system and connected to an electric signal measurement system composed of a charge amplifier and oscilloscope. When the cyclic impact loading was

applied by a free-falling pendulum hammer, the clamped specimen was deflected and the infilled PZT elements were strained to develop electric outputs. To confirm the measured output electric signals were generated from the piezoelectric effect, the IP³Cs were tested before and after electric poling. Due to the absence of effective polarization of PZT ceramics within the PDMS matrix, the composite shows negligible output voltage signals before electric poling treatment. In the polarized composites, the dipole moments of the PZT filler are aligned, resulting in more significant output voltage signals in Figure 43(b). It can be appreciated that the output voltage amplitudes of the composite specimens have corresponded to their piezoelectric performances when the free-falling pendulum hammer first hit the composite specimens. Notably, after six hits, the average output voltage amplitude of the 3-D interpenetrating-phase composite with ~50% porosity PZT has decreased to 0.79 V with a 65.1% drop, while the percentage decrease by 42.9% and 34.2% of the 3-D interpenetrating-phase composite with 40% and 60% porosity PZT ceramics, respectively. The voltage drops are directly related to the damping features of the composite materials, which has proved that the IP³C with appropriate porosity of piezoceramic filler can simultaneously achieve exceptional energy-absorbing capacity and piezoelectric sensitivity.

6.2.6 Dynamic compressive loading measurement

Figure 44(a)-(b) provide insight into the dynamic behaviors of the 3-D interpenetrating-phase composites under different loading frequencies (1Hz, 5Hz, 10Hz and 20Hz) at a constant strain of 0.5%. In Figure 44(a), both storage (G') and loss (G'') moduli decrease with the porosity of PZT ceramic structures from 30% to 70%, which have a good agreement with the mechanical strength measured in the “quasi-static” loading test.

It is a typical characteristic of polymers and their composites that the storage (G') and loss (G'') moduli increase slightly with the increase of loading frequencies. The passive damping features of the 3-D interpenetrating-phase PZT-PDMS composites are quantified by the material loss factor ($\tan \delta$), which is calculated by the equation of $\tan \delta = G''/G'$ and plotted in Figure 44(b).

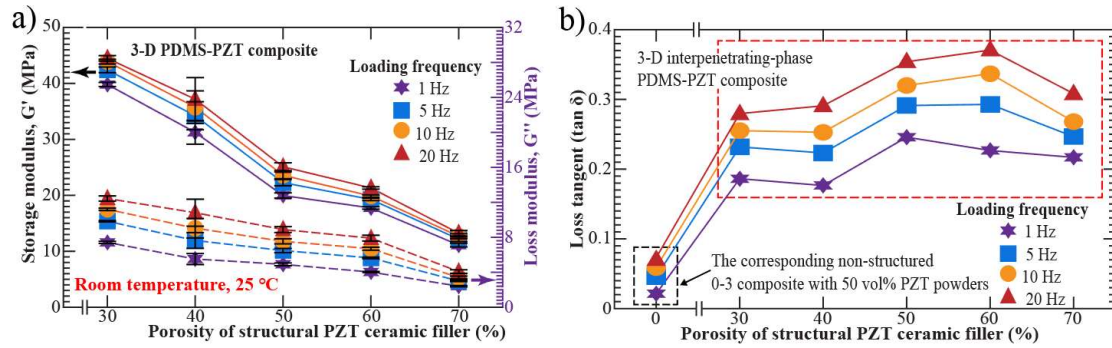


Figure 44 Comparison of interpenetrating phase composite and conventional composite (a) The comparison of the dynamic storage (G') and loss (G'') moduli of the composites with different porosity of infilled PZT structures. (b) The corresponding material loss factor ($\tan \delta$) of the composites under different loading frequencies.

As shown in Figure 45, the loss coefficient (loss factor - $\tan \delta$) of the paper proposed 3-D interpenetrating-phase PZT-PDMS composites is much higher than that of conventional metals, polymers, composites and most foam and elastomers.

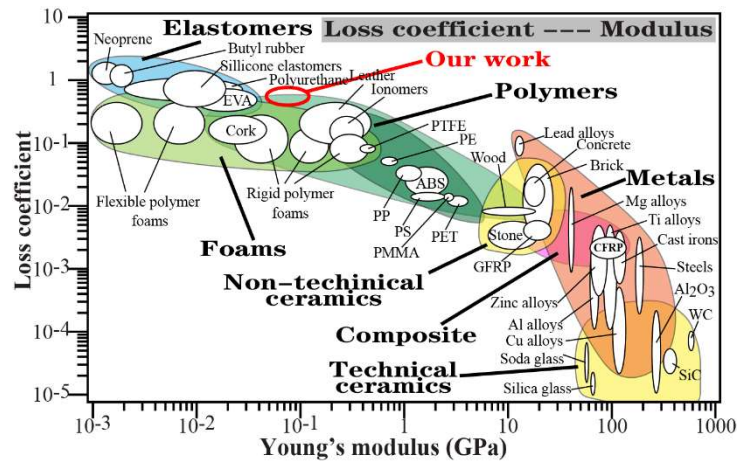


Figure 45 The comparison of the properties of the proposed 3-D interpenetrating-phase PZT-PDMS composite with other materials

6.3 Topology optimization of piezoelectric composites

The topology optimization method is a promising approach for designing smart materials systematically. Initially intended for mechanical structure design, this method was founded by Bendsøe and Kikuchi [85] a decade ago. Nowadays, it has matured and is being used to solve various industrial and academic problems, such as smart and passive material design, mechanism design, and microelectromechanical systems (MEMS) design. More recently, significant research works have been done towards designing composite structures.

The topology optimization problem involves distributing a given amount of material within a design domain to optimize an objective function. For instance, it could be used to design a load-bearing structure for maximum stiffness while keeping the weight under a certain limit. The goal is to find the optimal topology that connects, shapes, and numbers of holes within the structure to optimize the objective function.

To initialize the topology optimization problem, the design domain is discretized into a large number of elements. Each element can be either solid or void, creating a "bit-map"

of the structure by turning individual elements or pixels on or off. This 0/1 problem is ill-posed, as refining the mesh leads to a solution with finer details [202]. Optimal structures, at least for compliance optimization, consist of regions with infinitely fine microstructure. To overcome this, a microscale was introduced using the homogenization approach to topology optimization. This approach allows for the design of composites, including structures with fine microstructure. The homogenization approach has recently been applied to three-dimensional problems and multiple material problems. However, it can produce structures with large "grey" regions consisting of perforated material. This issue can be addressed by introducing a penalization of intermediate densities. An alternative method is to use SIMP method [203]. Because of the introduction of penalty term, the drawback of conventional homogenization method can be overcome. We start first by introducing the framework of SIMP.

6.3.1 SIMP for elastic compliance optimization

6.3.1.1 density interpolation for SIMP

The density-based SIMP method has been widely used to solve different mechanical problems, one of the benchmark example is the compliance problem considering only elasticity. Here we verify the SIMP code with this classic case.

A design domain is discretized by square finite elements and each element e is assigned a density x_e that determines its Young's modulus E_e :

$$E_e(x_e) = E_{\min} + x_e^p (E_0 - E_{\min}) \quad x_e \in [0 \ 1] \quad (6.1)$$

where E_0 is the stiffness of the material, E_{\min} is a very small stiffness assigned to void regions in order to prevent the stiffness matrix from becoming singular, and p is the penalization factor (usually $p=3$) introduced to ensure black-and-white solutions.

6.3.1.2 Filtering

To ensure the existence of solutions to the topology optimization problem; meanwhile, in order to avoid the formation of the checker-board patterns, some restriction on the design must be imposed. To do this, a common approach is the application of filter to either the sensitivities or the densities. A range of filtering methods is thoroughly discussed in [204].

The sensitivity filter modifies the sensitivities $\partial c / \partial x_e$ as follows

$$\frac{\partial \hat{c}}{\partial x_e} = \frac{1}{\max(\gamma, x_e) \sum_{i \in N_e} H_{ei}} \sum_{i \in N_e} H_{ei} x_i \frac{\partial c}{\partial x_i} \quad (6.2)$$

where N_e is the set of elements i for which the center to center distance $\Delta(e, i)$ to element e is smaller than the filter radius r_{\min} , c is the objective function, and H_{ei} is the weight factor defined as

$$H_{ei} = \max(0, r_{\min} - \Delta(e, i)) \quad (6.3)$$

The term γ ($=10^{-3}$) is small positive number introduced in order to avoid division by zero.

The density filter transforms the original densities x_e as follows:

$$\tilde{x}_e = \frac{1}{\sum_{i \in N_e} H_{ei}} \sum_{i \in N_e} H_{ei} x_i \quad (6.4)$$

6.3.1.3 MBB beam

The mathematical formulation of the optimization problem is described as:

$$\begin{aligned}
 \min : c(\mathbf{x}) &= \mathbf{U}^T \mathbf{K} \mathbf{U} = \sum_{e=1}^N E_e(x_e) \mathbf{u}_e^T \mathbf{k}_0 \mathbf{u}_e \\
 \text{subject to : } & V(\mathbf{x})/V_0 \\
 & \mathbf{K} \mathbf{U} = \mathbf{F} \\
 & 0 \leq \mathbf{x} \leq 1
 \end{aligned} \tag{6.5}$$

where c is the compliance, \mathbf{U} and \mathbf{F} are the global displacement and force, \mathbf{K} is the global stiffness matrix, \mathbf{u}_e is the element displacement vector, \mathbf{k}_0 is the element stiffness matrix for an element with unit Young's modulus, \mathbf{x} is the vector of design variables, N is the number of elements used to discretize the design domain, $V(\mathbf{x})$ and V_0 are the material volume and design domain volume, f is the prescribed volume fraction.

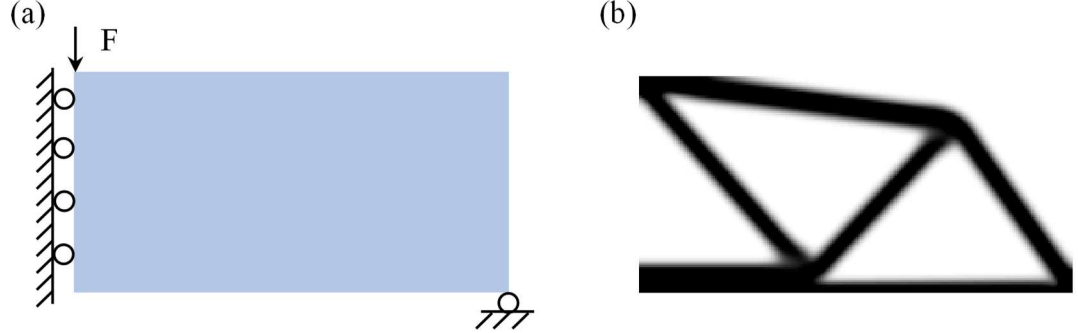


Figure 46 Numerical examples of beams for compliance optimization

The first MBB beam structure with boundary conditions as shown in Figure 46 (a) is studied, here only one material and voids are studied. The dimension of rectangle design domain is 100×50 , The beam is fixed at the left side, and a unit concentrated force is applied at the lower right corner. The Young's moduli of material 1 and voids are $E_1 = 1$

GPa, and $E_{\min} = 1E - 9$, respectively. Both materials have the same Poisson's ratio $\nu = 0.3$.

The volume fraction of the soft phase is $V_0 = 0.3$.

6.3.2 Finite element verification for piezoelectricity

The piezoelectric material converts mechanical energy into electrical energy and vice versa.

The linear coupled constitutive relation between mechanical and electrical behavior of piezoelectric material can be written in the following stress-charge form as

$$\begin{cases} T_{ij} = \mathbf{c}_{ijkl}^E S_{kl} - \mathbf{e}_{kij} E_k \\ D_i = \mathbf{e}_{ikl} S_{kl} + \boldsymbol{\epsilon}_{ik}^S E_k \end{cases} \quad (6.6)$$

where T_{ij} and S_{kl} are the stress and strain tensors, respectively. D_i and E_k denote the electric displacement and electric field. \mathbf{c}_{ijkl}^E is the elastic tensor under short circuit conditions, $\boldsymbol{\epsilon}_{ik}^S$ is the free body dielectric tensor, and \mathbf{e}_{ikl} is the piezoelectric strain tensor.

The above governing equation can be written in a compact matrix format as

$$\begin{cases} T = \mathbf{c}^E S - \mathbf{e} E \\ D = \mathbf{e}^T S + \boldsymbol{\epsilon}^S E \end{cases} \quad (6.7)$$

The strain and electric field of a single element can be described by shape functions in the finite element framework as

$$S^e = B_u u^e \quad (6.8)$$

$$E^e = B_\phi \phi^e \quad (6.9)$$

where u^e and ϕ^e are the displacements and potentials at the element nodes; B_u and B_ϕ are their shape functions related matrices.

Considering that given the external mechanical force, the internal virtual work is equal to the work done by the external force, the equilibrium equation can be expressed as

$$\int_{\Omega^e} (\delta S^e)^T T^e dv = (\delta u^e)^T F^e \quad (6.10)$$

On the other hand, due to the coupling effect, when electric field is applied to the element, the internal virtual work is equivalent to the work done by the external electric charges, so we have

$$\int_{\Omega^e} (\delta E^e)^T D^e dv = -(\delta \phi^e)^T Q^e \quad (6.11)$$

where Ω^e is the space of element e , δS^e and δE^e are the variations of strain and electric fields. The above equations leads to

$$\begin{cases} \left(\int_{\Omega^e} B_u^t \mathbf{c}^E B_u dv \right) u^e + \left(\int_{\Omega^e} B_u^t \mathbf{e} B_\phi dv \right) \phi^e = F^e \\ \left(\int_{\Omega^e} B_\phi^t \mathbf{e}^t B_u dv \right) u^e + \left(\int_{\Omega^e} B_\phi^t \boldsymbol{\epsilon}^S B_\phi dv \right) \phi^e = Q^e \end{cases} \quad (6.12)$$

The equation can be further simplified by

$$\begin{cases} \mathbf{K}_{uu}^e u^e + \mathbf{K}_{u\phi}^e \phi^e = F^e \\ \mathbf{K}_{\phi u}^e u^e - \mathbf{K}_{\phi\phi}^e \phi^e = Q^e \end{cases} \quad (6.13)$$

where $\mathbf{K}_{\phi u}^e = (\mathbf{K}_{u\phi}^e)^T$, and \mathbf{K}_{uu} and $\mathbf{K}_{\phi\phi}$ are two symmetric sparse matrices at the element level.

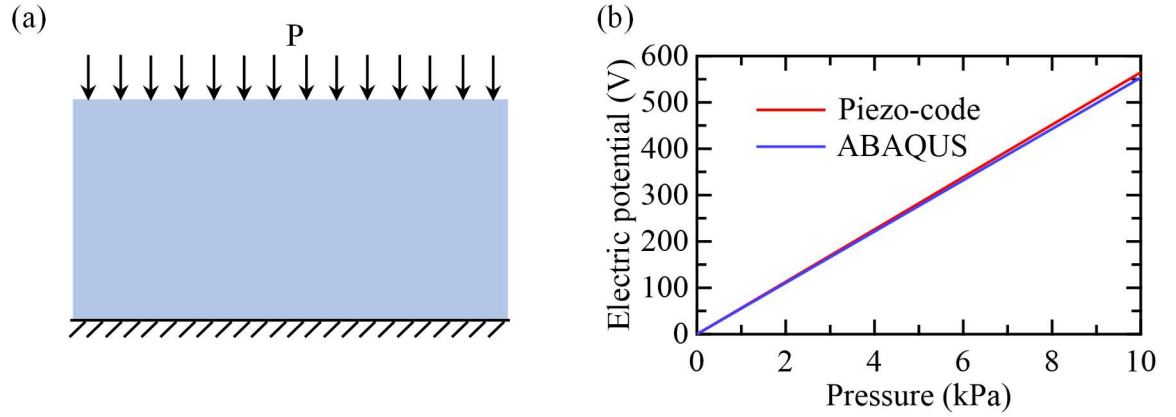


Figure 47 Piezoelectric finite element code verification against ABAQUS

For the second example, 2D piezoelectric plate is subject to pressure as shown in Figure 47(a). Young's modulus is $E=2.0$ GPa, Poisson's ratio $\nu=0.29$. Piezoelectric strain coefficients are $d_{31}=2.2\text{e-}11$ C/N, $d_{33}=-3.0\text{e-}11$ C/N. Relative permittivity $\mu=12$. The geometrical dimension of the design domain is 40×20 , as shown in Figure 47(a). The structure is under uniform pressure of $P=10$ kPa on the top surface. The electric potential versus time is plotted in Figure 47(b), it can be observed that the finite element code is consistent with the abaqus results.

6.3.3 Topology optimization of piezoelectric composite

6.3.3.1 Sensitivity analysis

Sensitivity analysis provides valuable insights into how a model responds to changes in input data. It can detect outliers, define testing strategies, optimize resources, reduce costs, and increase reliability. Incorporating sensitivity analysis into a study can significantly enhance the quality of the results and boost confidence in the model's predictions.

Although not a standard procedure, sensitivity analysis is highly beneficial to designers, builders, and code makers. It helps them identify the most influential data values and

understand how changes in materials, safety factors, or failure probabilities affect the overall reliability and cost of the work being designed. This method is both efficient and straightforward, allowing for simultaneous calculation of all sensitivities, making it an ideal tool for optimization procedures. The following demonstrates the sensitivity analysis for topology optimization of piezoelectric composites.

The work done by external force F is stored in the form of strain energy, Π^S , and electrical energy, Π^E . They are defined as the following:

$$\Pi^S = \frac{1}{2} u^T \mathbf{K}_{uu} u \quad (6.14)$$

$$\Pi^E = \frac{1}{2} \phi^T \mathbf{K}_{\phi\phi} \phi \quad (6.15)$$

Here we define the energy conversion factor as

$$\eta = \frac{\Pi^E}{\Pi^E + \Pi^S} \quad (6.16)$$

Our objective here is to simultaneously optimize the energy absorption and energy conversion factor. Therefore, we define the objection function as

$$f_{TO} = \Pi^S + \eta = \Pi^S + \frac{\Pi^E}{\Pi^E + \Pi^S} \quad (6.17)$$

The topology optimization problem becomes

$$\begin{aligned}
\min \quad & \zeta = \frac{1}{f_{TO}} = \frac{(\Pi^S)^2 + \Pi^E \Pi^S + \Pi^E}{\Pi^E + \Pi^S} \\
s.t. \quad & V(x) = \sum_{i=1}^N x_i v_i \leq \bar{V} \\
& 0 < x_i < 1, i \in [1, N]
\end{aligned} \tag{6.18}$$

The optimal configuration can be obtained by re-distributing materials among the design domain using a gradient search method. In order to acquire the optimal solution using the gradient search, sensitivity analysis must be performed with respect to objective functions and constraints. Basically, the sensitivity can be calculated as the first order derivative of the objective function with regard to the design variables. By taking the derivative of the objective function, we have

$$\begin{aligned}
\frac{\partial \zeta}{\partial x_i} = & \frac{1}{(\Pi^S)^2 + \Pi^E \Pi^S + \Pi^E} \left(\frac{\partial \Pi^E}{\partial x_i} + \frac{\partial \Pi^S}{\partial x_i} \right) \\
& - \frac{(\Pi^E + \Pi^S)}{\left[(\Pi^S)^2 + \Pi^E \Pi^S + \Pi^E \right]^2} \left(2\Pi^S \frac{\partial \Pi^S}{\partial x_i} + \Pi^S \frac{\partial \Pi^E}{\partial x_i} + \Pi^E \frac{\partial \Pi^S}{\partial x_i} + \frac{\partial \Pi^E}{\partial x_i} \right)
\end{aligned} \tag{6.19}$$

There are two derivatives in the above equation, $\frac{\partial \Pi^S}{\partial x_i}$, $\frac{\partial \Pi^E}{\partial x_i}$, which can be obtained by using adjoint method. This is discussed below.

From the governing equation, we can write

$$\Pi^{S*} = \Pi^S = \frac{1}{2} u^T \mathbf{K}_{uu} u + \lambda_1^T (\mathbf{K}_{uu} u + \mathbf{K}_{u\phi} \phi - F) + \theta_1^T (\mathbf{K}_{\phi u} u - \mathbf{K}_{\phi\phi} \phi) \tag{6.20}$$

where λ_1 and θ_1 are the arbitrary adjoint displacement and potential vectors. Taking the first-order derivative of above equation, we have

$$\begin{aligned}
\frac{\partial \Pi^{S*}}{\partial x_i} &= \frac{\partial \Pi^S}{\partial x_i} = \left(u^T \mathbf{K}_{uu} + \lambda_1^T \mathbf{K}_{uu} + \theta_1^T \mathbf{K}_{\phi u} \right) \frac{\partial u}{\partial x_i} \\
&\quad + \left(\lambda_1^T \mathbf{K}_{u\phi} - \theta_1^T \mathbf{K}_{\phi\phi} \right) \frac{\partial \phi}{\partial x_i} \\
&\quad + \frac{1}{2} u^T \frac{\partial \mathbf{K}_{uu}}{\partial x_i} + \lambda_1^T \frac{\partial \mathbf{K}_{uu}}{\partial x_i} + \lambda_1^T \frac{\partial \mathbf{K}_{u\phi}}{\partial x_i} \phi \\
&\quad + \theta_1^T \frac{\partial \mathbf{K}_{\phi u}}{\partial x_i} u - \theta_1^T \frac{\partial \mathbf{K}_{\phi\phi}}{\partial x_i} \phi - \lambda_1^T \frac{\partial F}{\partial x_i}
\end{aligned} \tag{6.21}$$

It is easy to find the derivatives of all the stiffness matrices, but it's difficult to obtain the derivatives of displacement and potential. To eliminate the calculation of derivatives of displacement and potential, adjoint equations are formulated as

$$\begin{cases} \mathbf{K}_{uu} \lambda_1 + \mathbf{K}_{u\phi} \theta_1 = -\mathbf{K}_{uu} u \\ \mathbf{K}_{\phi u} \lambda_1 + \mathbf{K}_{\phi\phi} \theta_1 = 0 \end{cases} \tag{6.22}$$

After solving the above equation, we can obtain λ_1 and θ_1 . Then we substitute λ_1 and θ_1 back into Eq. 6.21, we could easily obtain the gradient of strain energy.

On the other hand, by adding the governing equation to Π^E and take the derivative, we have

$$\Pi^{E*} = \Pi^E = \frac{1}{2} \phi^T \mathbf{K}_{\phi\phi} u + \lambda_2^T \left(\mathbf{K}_{uu} u + \mathbf{K}_{u\phi} \phi - F \right) + \theta_2^T \left(\mathbf{K}_{\phi u} u - \mathbf{K}_{\phi\phi} \phi \right) \tag{6.23}$$

$$\begin{aligned}
\frac{\partial \Pi^{E*}}{\partial x_i} &= \frac{\partial \Pi^E}{\partial x_i} = \left(\lambda_2^T \mathbf{K}_{uu} + \theta_2^T \mathbf{K}_{\phi u} \right) \frac{\partial u}{\partial x_i} \\
&\quad + \left(\phi^T \mathbf{K}_{\phi\phi} + \lambda_2^T \mathbf{K}_{u\phi} - \theta_1^T \mathbf{K}_{\phi\phi} \right) \frac{\partial \phi}{\partial x_i} \\
&\quad + \frac{1}{2} \phi^T \frac{\partial \mathbf{K}_{\phi\phi}}{\partial x_i} + \lambda_2^T \frac{\partial \mathbf{K}_{uu}}{\partial x_i} + \lambda_2^T \frac{\partial \mathbf{K}_{u\phi}}{\partial x_i} \phi \\
&\quad + \theta_2^T \frac{\partial \mathbf{K}_{\phi u}}{\partial x_i} u - \theta_2^T \frac{\partial \mathbf{K}_{\phi\phi}}{\partial x_i} \phi - \lambda_2^T \frac{\partial F}{\partial x_i}
\end{aligned} \tag{6.24}$$

Using the same approach, the derivatives of displacement and potential with respect to design variable can be eliminated by solving the adjoint equations

$$\begin{cases} \mathbf{K}_{uu} \lambda_2 + \mathbf{K}_{u\phi} \theta_2 = 0 \\ \mathbf{K}_{\phi u} \lambda_2 + \mathbf{K}_{\phi\phi} \theta_2 = -\mathbf{K}_{\phi\phi} \phi \end{cases} \tag{6.25}$$

6.3.3.2 examples

For the piezoelectric composites example, 2D piezoelectric plate is subject to concentrate load as shown in Figure 48(a). Only two phases are considered, one phase is piezoelectric material; the other one is the non-piezoelectric material, and voids are not included. Young's modulus piezoelectric material is $E_p=2.0$ GPa, Poisson's ratio $\nu=0.29$. Non-piezoelectric material has Young's modulus $E_{np}=10$ Mpa, Poisson's ratio $\nu=0.29$. Piezoelectric strain coefficients are $d_{31}=2.2\text{e-}11$ C/N, $d_{33}=-3.0\text{e-}11$ C/N. Relative permittivity $\mu=12$, Volume fraction of piezoelectric material is 0.3. The geometrical dimension of the design domain is 100×50 , as shown in Figure 48(a).

The interpolation scheme for this problem is

$$E_e(x_e) = E_{np} + x_e^p (E_p - E_{np}) \quad x_e \in [0 \ 1] \tag{6.26}$$

$$\mathbf{e}(x_e) = x_e^p \mathbf{e}_p \quad x_e \in [0 \ 1] \tag{6.27}$$

$$\mathbf{\epsilon}(x_e) = x_e^p \mathbf{\epsilon}_p \quad x_e \in [0 \ 1] \quad (6.28)$$

where E_p and E_{np} are Young's modulus for piezoelectric material and non-piezoelectric material, p is penalty factor, \mathbf{e}_p and $\mathbf{\epsilon}_p$ are the piezoelectric coupling and dielectric coefficient, respectively.

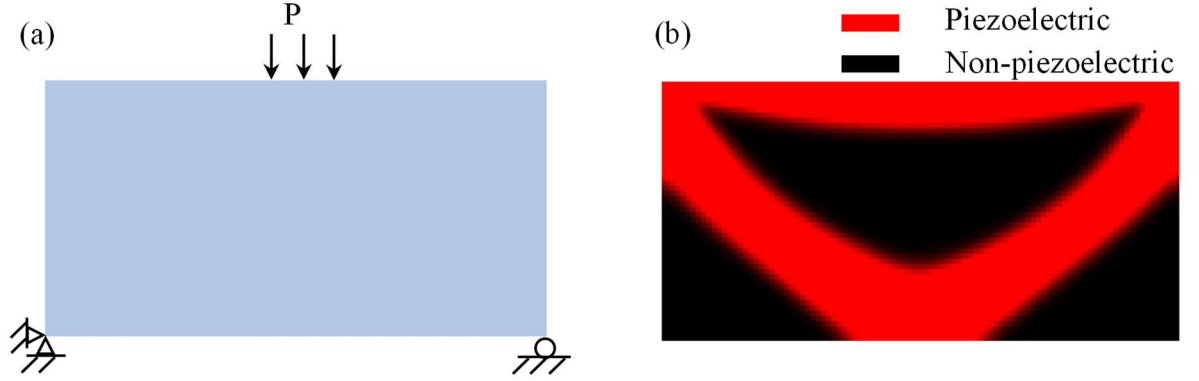


Figure 48 Topology optimization of piezoelectric composites considering linear elastic properties

6.4 Conclusions

In this chapter, we first presented the investigation of a new type of high-performance and multifunctional energy-absorbing composite materials have been developed by infiltrating 3-D structured PZT ceramic with polymeric PDMS matrix. The interpenetrating architecture of each phase ensures the unprecedented combination of mechanical and piezoelectric properties of the proposed multifunctional composites. Mechanically, the mutual constraint between the interconnected PZT skeleton and polymer phase has significantly improved the stress transferability within the IP³C, which cannot be attained in conventional hybrid composites. This characteristic is accompanied by a synergetic

enhancement of its energy dissipation efficiency, resulting in extraordinary damping capacity exceeding that of a rule-of-mixtures estimate from its compositions. Specifically, attribute to the intrinsic piezoelectricity of the PZT ceramic and the effective load transfer permitted by the interpenetrating architectures, the proposed IP³C displays prominent piezoelectric performance for impact monitoring. Then we adopted the SIMP-based topology optimization framework to optimize the piezoelectric composites. Although only linear elasticity is considered in the study, topology optimization has proved to be an efficient approach to find the material distribution to maximize the objective function.

CHAPTER 7

CONCLUSIONS AND OUTLOOK

7.1 Main contributions

The research studies presented from chapter 2 to 6 are focused on designing, modeling, 3D printing, mechanical testing, and topology optimization of architected materials. The objective is to achieve enhanced mechanical performance and multifunctionalities. In addition, the tunability of the mechanical properties is also studied. The main scientific contributions are summarized as follows:

(1) Proposed new design paradigm to achieve low-frequency phononic band gaps in 3D architected metamaterials. Phononic band gaps are formed through two main mechanisms, Bragg scattering and local resonance. Band gaps induced by Bragg scattering are dependent on periodicity and the symmetry of the lattice. However, phononic crystals with Bragg-type band gaps are limited in their application because they do not attenuate vibration at lower frequencies without requiring large geometries. Alternatively, band gaps formed by local resonance are due to the excitation of resonant frequencies, and these band gaps are independent of periodicity. Nonetheless, the application of phononic metamaterials is largely hindered by their limited operation frequency range and inferior mechanical properties. In the work presented in chapter 3, a new design paradigm is proposed. By tailoring the geometric parameters of 3D architected hollow sphere foams, a

broad range of band gap can be obtained. In addition, by tailoring the stiffness contrast between hollow sphere and binder, phononic band gaps can be shifted toward a very low-frequency range.

(2) Developed 3D graded architected polymer foams for enhanced energy absorption.

Graded design strategy has been exploited to achieve enhanced mechanical performance, the research is mainly focused on the simple lattice structures. In the work presented in chapter 4, a graded design of 3D architected polymer foam is proposed. By using a combined numerical and experimental approach, the large deformation of 3D polymer foam is studied. It is found that three failure mechanisms dominate the mechanical behavior of foams for different binder sizes, including binder-failure-only, shell-failure-only, and binder-shell failure. In addition, the relative density studies show that the foam structure demonstrates bending-dominated deformation mechanism. Guided by the findings, graded design of 3D architected polymer foam is developed, it is found that the specific energy absorption of hybrid graded foam is significantly improved with respect to binder graded foam, shell graded foam and uniform foam. Furthermore, compared with the existing lattice-based and shell-based graded foams, the hybrid graded foam shows superior mechanical performance, including stiffness, strength and energy absorption. This findings presented open a new avenue to engineer architected materials with enhanced mechanical properties.

(3) Developed multiphased architected composites for enhanced energy absorption and shape recovery. Bioinspired materials have received much attention recently, however, studies related to the mechanical behavior and failure modes under large deformations are limited. In chapter 5, bioinspired multilayered cellular composites is

developed and explored systematically through experiment and simulation approaches. It is found that under large deformation framework, the finite element simulations and 2D digital image correlation (DIC) reveal that the multilayered architecture provides more uniform strain distribution and higher stress transfer efficiency; and the failure mode shows a progressive pattern compared to the catastrophic failure of conventional material. In addition, the cyclic loading tests demonstrate that the multilayered cellular composites possesses exceptional shape recoverability under compressive strains. These remarkable performance characteristics result from the synergies between the properties of the two constituent materials and the chosen multilayered cellular microstructure. The deformation mechanisms demonstrated here are robust and are applicable to other architected cellular materials across multiple length scales and provide new avenue to design lightweight and high-resilience structural materials.

(4) Developed new piezoelectric composites with multifunctionalities and a topology optimization framework to optimize the composites with multiple objectives.

Conventionally, piezoelectric materials have limited mechanical properties and electromechanical-conversion properties, mainly due to the inefficient of stress transferability. In chapter 6, by using facial camphene-templated freeze-casting method, a 3D interconnected piezoelectric composites are fabricated and studied. The rationally designed interpenetrating architecture endows the proposed piezoelectric composites with unprecedented combination of mechanical-damping and electromechanical-conversion properties. Intrinsically, the interpenetrating design motif enables the high stress transfer efficiency within the piezoelectric material phase. On the other hand, although this rational design yields superior multifunctionalities, this design is still not optimal. In order to

overcome the expensiveness of conventional design approaches. Topology optimization framework is proposed to realize the optimal design. To incorporate multiple objective functions, a single objective function with weighted combination of multiple objectives is developed. Adjoint method is adopted to derive the shape sensitivity analysis. Based on the SIMP topology optimization method, a simple example with linear elasticity is demonstrated in chapter 6.

7.2 Future work

Architected metamaterial design concept is a powerful tool to explore novel and unusual physical properties. The designed architected metamaterials therefore have a wide range of promising applications, especially when design is combined with the modern manufacturing technologies like 3D printing. Some future works could be toward, but are not limited to, the following directions.

(1) Topology optimization of architected materials considering non-linear constitutive relations and multiphysics problem. As demonstrated in this work, topology optimization is very efficient to design architected materials with optimal architecture and material layouts. However, the linear elasticity assumption in this work is not sufficient to simulate the material properties in most of applications. Therefore, non-linear constitutive relation needs to be considered, such as elastic-plastic model, viscoplastic model, hyperelastic model, and damage mechanics model, etc. On the other hand, many applications involve multiphysics problem. For example, topology optimization of stent structure in vivo entails multiphysics coupling between structural mechanics, fluid mechanics, and chemistry. Therefore, developing a topology optimization framework

considering non-linear material behavior and multiphysics coupling is still open research area.

(2) High velocity impact of architected materials. The 3D architected materials studied in chapter 4 & 5 have shown enhanced energy absorption properties under large deformation in a quasi-static condition. However, in practice, many of the engineering applications of materials and structures such as auto industry, defense industry require robust mechanical behavior in the extreme conditions such as high velocity. Although the deformation mechanism and failure mode have been explored in quasi-static condition, they are not applicable in high velocity impact. Therefore, a systematic study of 3D architected materials under high velocity impact is needed to understand their mechanical behavior.

(3) Multifunctional design of architected materials toward more applications. It has been demonstrated that in chapter 3 & 4, architected polymer foam can be featured with broad band vibration mitigation property and superior mechanical performance. In chapter 6, piezoelectric composites exhibit unprecedented combination of mechanical-damping and electromechanical-conversion properties. Therefore, multifunctional architected materials serve as better candidates to meet the requirements of more broad applications. However, the current studies are still quite limited with respect to the demands from engineering applications. For example, in the battery module, the separator should embed robust mechanical properties with superior thermal properties in order to prevent thermal runaway. Therefore, there is need for designing more multifunctional architected materials for various applications.

REFERENCES

1. Tretyakov, S.A., *A personal view on the origins and developments of the metamaterial concept*. Journal of Optics, 2016. **19**(1): p. 013002.
2. Mousavi, S.H., A.B. Khanikaev, and Z. Wang, *Topologically protected elastic waves in phononic metamaterials*. Nature Communications, 2015. **6**(1): p. 8682.
3. Wang, Y.-F., et al., *Tunable and Active Phononic Crystals and Metamaterials*. Applied Mechanics Reviews, 2020. **72**(4).
4. Wang, J., G. Dai, and J. Huang, *Thermal Metamaterial: Fundamental, Application, and Outlook*. iScience, 2020. **23**(10): p. 101637.
5. Li, Y., et al., *Transforming heat transfer with thermal metamaterials and devices*. Nature Reviews Materials, 2021. **6**(6): p. 488-507.
6. Feng, L., et al., *Photonic Metamaterial Absorbers: Morphology Engineering and Interdisciplinary Applications*. Advanced Materials, 2020. **32**(27): p. 1903787.
7. Litchinitser, N.M. and V.M. Shalaev, *Photonic metamaterials*. Laser Physics Letters, 2008. **5**(6): p. 411-420.
8. Bertoldi, K., et al., *Flexible mechanical metamaterials*. Nature Reviews Materials, 2017. **2**(11): p. 17066.
9. Barchiesi, E., M. Spagnuolo, and L. Placidi, *Mechanical metamaterials: a state of the art*. Mathematics and Mechanics of Solids, 2018. **24**(1): p. 212-234.
10. Ashby, M.F. and Y.J.M. Bréchet, *Designing hybrid materials*. Acta Materialia, 2003. **51**(19): p. 5801-5821.
11. Masoumi Khalil Abad, E., S. Arabnejad Khanoki, and D. Pasini, *Fatigue design of lattice materials via computational mechanics: Application to lattices with smooth transitions in cell geometry*. International Journal of Fatigue, 2013. **47**: p. 126-136.
12. Schaedler, T.A. and W.B.J.A.R.o.M.R. Carter, *Architected cellular materials*. 2016. **46**: p. 187-210.
13. Vyatskikh, A., et al., *Additive manufacturing of 3D nano-architected metals*. Nature Communications, 2018. **9**(1): p. 593.
14. Stansfeld, S.A. and M.P. Matheson, *Noise pollution: non-auditory effects on health*. British Medical Bulletin, 2003. **68**(1): p. 243-257.
15. Smith, M.G., et al., *On the Influence of Freight Trains on Humans: A Laboratory Investigation of the Impact of Nocturnal Low Frequency Vibration and Noise on Sleep and Heart Rate*. PLOS ONE, 2013. **8**(2): p. e55829.
16. Athanasopoulos, G.A. and P.C. Pelekis, *Ground vibrations from sheetpile driving in urban environment: measurements, analysis and effects on buildings and occupants*. Soil Dynamics and Earthquake Engineering, 2000. **19**(5): p. 371-387.
17. Konon, W. and R. Schuring John, *Vibration Criteria for Historic Buildings*. Journal of Construction Engineering and Management, 1985. **111**(3): p. 208-215.
18. Rivin, E.I., *Vibration isolation of precision equipment*. Precision Engineering, 1995. **17**(1): p. 41-56.
19. Gasser, S., Y. Brechet, and F.J.A.E.M. Paun, *Materials Design for Acoustic Liners: an Example of Tailored Multifunctional Materials*. 2004. **6**(1-2): p. 97-102.
20. Khan, S.U., et al., *Vibration damping characteristics of carbon fiber-reinforced composites containing multi-walled carbon nanotubes*. Composites Science and Technology, 2011. **71**(12): p. 1486-1494.
21. Huang, X., et al., *Topology optimization for microstructures of viscoelastic composite materials*. Computer Methods in Applied Mechanics and Engineering, 2015. **283**: p. 503-516.

22. Asadpoure, A., M. Tootkaboni, and L. Valdevit, *Topology optimization of multiphase architected materials for energy dissipation*. Computer Methods in Applied Mechanics and Engineering, 2017. **325**: p. 314-329.
23. Schaedler, T.A. and W.B. Carter, *Architected Cellular Materials*. Annual Review of Materials Research, 2016. **46**(1): p. 187-210.
24. Bertoldi, K., *Harnessing Instabilities to Design Tunable Architected Cellular Materials*. Annual Review of Materials Research, 2017. **47**(1): p. 51-61.
25. Lu, M.-H., L. Feng, and Y.-F. Chen, *Phononic crystals and acoustic metamaterials*. Materials Today, 2009. **12**(12): p. 34-42.
26. Zhang, G.Y. and X.L. Gao, *Band gaps for flexural elastic wave propagation in periodic composite plate structures based on a non-classical Mindlin plate model incorporating microstructure and surface energy effects*. Continuum Mechanics and Thermodynamics, 2019. **31**(6): p. 1911-1930.
27. Zhang, G.Y. and X.L. Gao, *Elastic wave propagation in 3-D periodic composites: Band gaps incorporating microstructure effects*. Composite Structures, 2018. **204**: p. 920-932.
28. Elmadhi, W., et al., *Mechanical vibration bandgaps in surface-based lattices*. Additive Manufacturing, 2019. **25**: p. 421-429.
29. Ampatzidis, T., et al., *Band gap behaviour of optimal one-dimensional composite structures with an additive manufactured stiffener*. Composites Part B: Engineering, 2018. **153**: p. 26-35.
30. Xia, B., G. Wang, and S. Zheng, *Robust edge states of planar phononic crystals beyond high-symmetry points of Brillouin zones*. Journal of the Mechanics and Physics of Solids, 2019. **124**: p. 471-488.
31. Zhang, P. and A.C. To, *Broadband wave filtering of bioinspired hierarchical phononic crystal*. Applied Physics Letters, 2013. **102**(12): p. 121910.
32. Bacigalupo, A. and L. Gambarotta, *Dispersive wave propagation in two-dimensional rigid periodic blocky materials with elastic interfaces*. Journal of the Mechanics and Physics of Solids, 2017. **102**: p. 165-186.
33. Liu, Z., C.T. Chan, and P. Sheng, *Three-component elastic wave band-gap material*. Physical Review B, 2002. **65**(16): p. 165116.
34. Achaoui, Y., et al., *Experimental observation of locally-resonant and Bragg band gaps for surface guided waves in a phononic crystal of pillars*. Physical Review B, 2011. **83**(10): p. 104201.
35. Wang, G., et al., *Two-Dimensional Locally Resonant Phononic Crystals with Binary Structures*. Physical Review Letters, 2004. **93**(15): p. 154302.
36. Hsu, J.-C., *Local resonances-induced low-frequency band gaps in two-dimensional phononic crystal slabs with periodic stepped resonators*. Journal of Physics D: Applied Physics, 2011. **44**(5): p. 055401.
37. Liu, Z., et al., *Locally Resonant Sonic Materials*. Science, 2000. **289**(5485): p. 1734-1736.
38. Chen, Y. and L. Wang, *Periodic co-continuous acoustic metamaterials with overlapping locally resonant and Bragg band gaps*. Applied Physics Letters, 2014. **105**(19): p. 191907.
39. Krushynska, A.O., V.G. Kouznetsova, and M.G.D. Geers, *Towards optimal design of locally resonant acoustic metamaterials*. Journal of the Mechanics and Physics of Solids, 2014. **71**: p. 179-196.
40. Matlack Kathryn, H., et al., *Composite 3D-printed metastructures for low-frequency and broadband vibration absorption*. Proceedings of the National Academy of Sciences, 2016. **113**(30): p. 8386-8390.
41. Ahuja, K., et al., *A new wide-band acoustic liner with high temperature capability*, in *3rd AIAA/CEAS Aeroacoustics Conference*. 1997, American Institute of Aeronautics and Astronautics.

42. Jiang, H. and Y. Chen, *Lightweight architected hollow sphere foams for simultaneous noise and vibration control*. Journal of Physics D: Applied Physics, 2019. **52**(32): p. 325303.
43. Sanders, W.S. and L.J. Gibson, *Mechanics of hollow sphere foams*. Materials Science and Engineering: A, 2003. **347**(1): p. 70-85.
44. Jia, Z., et al., *Prediction of the Effective Thermal Conductivity of Hollow Sphere Foams*. ACS Applied Energy Materials, 2018. **1**(3): p. 1146-1157.
45. Zhang, Q., et al., *Quasi-static and dynamic compression behavior of glass cenospheres/5A03 syntactic foam and its sandwich structure*. Composite Structures, 2018. **183**: p. 499-509.
46. Song, Y., et al., *Dynamic crushing behavior of 3D closed-cell foams based on Voronoi random model*. Materials & Design, 2010. **31**(9): p. 4281-4289.
47. Chen, Y., R. Das, and M. Battley, *Effects of cell size and cell wall thickness variations on the strength of closed-cell foams*. International Journal of Engineering Science, 2017. **120**: p. 220-240.
48. Maiti, A., et al., *3D printed cellular solid outperforms traditional stochastic foam in long-term mechanical response*. Scientific Reports, 2016. **6**(1): p. 24871.
49. Jiang, H., et al., *Mechanical properties of 3D printed architected polymer foams under large deformation*. Materials & Design, 2020. **194**: p. 108946.
50. Deshpande, V.S., N.A. Fleck, and M.F. Ashby, *Effective properties of the octet-truss lattice material*. Journal of the Mechanics and Physics of Solids, 2001. **49**(8): p. 1747-1769.
51. Chen, Y., Z. Jia, and L. Wang, *Hierarchical honeycomb lattice metamaterials with improved thermal resistance and mechanical properties*. Composite Structures, 2016. **152**: p. 395-402.
52. Queheillalt, D.T., Y. Katsumura, and H.N.G. Wadley, *Synthesis of stochastic open cell Ni-based foams*. Scripta Materialia, 2004. **50**(3): p. 313-317.
53. Niino, M.J.J.C.M., *Functionally gradient materials as thermal barrier for space plane*. 1987. **13**: p. 257-264.
54. Maskery, I., et al., *A mechanical property evaluation of graded density Al-Si10-Mg lattice structures manufactured by selective laser melting*. Materials Science and Engineering: A, 2016. **670**: p. 264-274.
55. Song, J., et al., *Metal-coated hybrid meso-lattice composites and their mechanical characterizations*. Composite Structures, 2018. **203**: p. 750-763.
56. Zhang, X., et al., *Three-Dimensional High-Entropy Alloy-Polymer Composite Nanolattices That Overcome the Strength-Recoverability Trade-off*. Nano Letters, 2018. **18**(7): p. 4247-4256.
57. Mueller, J., et al., *Architected Lattices with High Stiffness and Toughness via Multicore-Shell 3D Printing*. Advanced Materials, 2018. **30**(12): p. 1705001.
58. Stanković, T., et al., *A Generalized Optimality Criteria Method for Optimization of Additively Manufactured Multimaterial Lattice Structures*. Journal of Mechanical Design, 2015. **137**(11).
59. Chan, Y.-C., K. Shintani, and W. Chen, *Robust topology optimization of multi-material lattice structures under material and load uncertainties*. Frontiers of Mechanical Engineering, 2019. **14**(2): p. 141-152.
60. Boley, J.W., et al., *Shape-shifting structured lattices via multimaterial 4D printing*. Proceedings of the National Academy of Sciences, 2019. **116**(42): p. 20856-20862.
61. Dimas, L.S., et al., *Tough Composites Inspired by Mineralized Natural Materials: Computation, 3D printing, and Testing*. Advanced Functional Materials, 2013. **23**(36): p. 4629-4638.
62. Dimas, L.S. and M.J. Buehler, *Modeling and additive manufacturing of bio-inspired composites with tunable fracture mechanical properties*. Soft Matter, 2014. **10**(25): p. 4436-4442.

63. Grossman, M., et al., *Hierarchical Toughening of Nacre-Like Composites*. Advanced Functional Materials, 2019. **29**(9): p. 1806800.
64. Grossman, M., et al., *Mineral Nano-Interconnectivity Stiffens and Toughens Nacre-like Composite Materials*. Advanced Materials, 2017. **29**(8): p. 1605039.
65. Wegst, U.G.K., et al., *Bioinspired structural materials*. Nature Materials, 2015. **14**(1): p. 23-36.
66. Ortiz, C. and C. Boyce Mary, *Bioinspired Structural Materials*. Science, 2008. **319**(5866): p. 1053-1054.
67. Gao, H., et al., *Materials become insensitive to flaws at nanoscale: Lessons from nature*. Proceedings of the National Academy of Sciences, 2003. **100**(10): p. 5597-5600.
68. Tran, P., et al., *Bimaterial 3D printing and numerical analysis of bio-inspired composite structures under in-plane and transverse loadings*. Composites Part B: Engineering, 2017. **108**: p. 210-223.
69. Woesz, A., et al., *Micromechanical properties of biological silica in skeletons of deep-sea sponges*. Journal of Materials Research, 2006. **21**(8): p. 2068-2078.
70. Birkbak, M.E., et al., *Internal structure of sponge glass fiber revealed by ptychographic nanotomography*. Journal of Structural Biology, 2016. **194**(1): p. 124-128.
71. Gao, H., J. Lam, and C. Wang, *Robust energy-to-peak filter design for stochastic time-delay systems*. Systems & Control Letters, 2006. **55**(2): p. 101-111.
72. Studart, A.R., *Towards High-Performance Bioinspired Composites*. Advanced Materials, 2012. **24**(37): p. 5024-5044.
73. Chen, P.Y., et al., *Structure and mechanical properties of selected biological materials*. Journal of the Mechanical Behavior of Biomedical Materials, 2008. **1**(3): p. 208-226.
74. Gibson, L.J. and M.F. Ashby, *Cellular Solids: Structure and Properties*. 2 ed. Cambridge Solid State Science Series. 1997, Cambridge: Cambridge University Press.
75. Newnham, R.E., D.P. Skinner, and L.E. Cross, *Connectivity and piezoelectric-pyroelectric composites*. Materials Research Bulletin, 1978. **13**(5): p. 525-536.
76. Park, K.-I., et al., *Flexible Nanocomposite Generator Made of BaTiO₃ Nanoparticles and Graphitic Carbons*. Advanced Materials, 2012. **24**(22): p. 2999-3004.
77. Zhou, Z., H. Tang, and H.A. Sodano, *Scalable Synthesis of Morphotropic Phase Boundary Lead Zirconium Titanate Nanowires for Energy Harvesting*. Advanced Materials, 2014. **26**(45): p. 7547-7554.
78. Yan, M., et al., *Flexible pillar-base structured piezocomposite with aligned porosity for piezoelectric energy harvesting*. Nano Energy, 2021. **88**: p. 106278.
79. Zhang, G., et al., *Flexible three-dimensional interconnected piezoelectric ceramic foam based composites for highly efficient concurrent mechanical and thermal energy harvesting*. Energy & Environmental Science, 2018. **11**(8): p. 2046-2056.
80. Ha, N.S. and G. Lu, *A review of recent research on bio-inspired structures and materials for energy absorption applications*. Composites Part B: Engineering, 2020. **181**: p. 107496.
81. Roscow, J.I., et al., *Freeze cast porous barium titanate for enhanced piezoelectric energy harvesting*. Journal of Physics D: Applied Physics, 2018. **51**(22): p. 225301.
82. Cui, H., et al., *Three-dimensional printing of piezoelectric materials with designed anisotropy and directional response*. Nature Materials, 2019. **18**(3): p. 234-241.
83. Sigmund, O., *On the Design of Compliant Mechanisms Using Topology Optimization*. Mechanics of Structures and Machines, 1997. **25**(4): p. 493-524.
84. Sigmund, O., *Design of multiphysics actuators using topology optimization – Part II: Two-material structures*. Computer Methods in Applied Mechanics and Engineering, 2001. **190**(49): p. 6605-6627.
85. Bendsoe, M.P. and N. Kikuchi, *Generating optimal topologies in structural design using a homogenization method*. Computer Methods in Applied Mechanics and Engineering, 1988. **71**(2): p. 197-224.

86. Suzuki, K. and N. Kikuchi, *A homogenization method for shape and topology optimization*. Computer Methods in Applied Mechanics and Engineering, 1991. **93**(3): p. 291-318.
87. Díaz, A.R. and M.P. Bendsøe, *Shape optimization of structures for multiple loading conditions using a homogenization method*. Structural optimization, 1992. **4**(1): p. 17-22.
88. Bendsøe, M.P., *Optimal shape design as a material distribution problem*. Structural optimization, 1989. **1**(4): p. 193-202.
89. Mlejnek, H.P., *Some aspects of the genesis of structures*. Structural optimization, 1992. **5**(1): p. 64-69.
90. Bendsøe, M.P. and O. Sigmund, *Material interpolation schemes in topology optimization*. Archive of Applied Mechanics, 1999. **69**(9): p. 635-654.
91. Xie, Y.M. and G.P. Steven, *A simple evolutionary procedure for structural optimization*. Computers & Structures, 1993. **49**(5): p. 885-896.
92. Osher, S. and J.A. Sethian, *Fronts propagating with curvature-dependent speed: Algorithms based on Hamilton-Jacobi formulations*. Journal of Computational Physics, 1988. **79**(1): p. 12-49.
93. Shu, L., et al., *Level set based structural topology optimization for minimizing frequency response*. Journal of Sound and Vibration, 2011. **330**(24): p. 5820-5834.
94. Zhang, P. and A.C. To, *Transversely isotropic hyperelastic-viscoplastic model for glassy polymers with application to additive manufactured photopolymers*. International Journal of Plasticity, 2016. **80**: p. 56-74.
95. Arruda, E.M. and M.C. Boyce, *A three-dimensional constitutive model for the large stretch behavior of rubber elastic materials*. Journal of the Mechanics and Physics of Solids, 1993. **41**(2): p. 389-412.
96. Kohan, M.I., *Nylon Plastics Handbook*. 1995: Nylon plastics handbook.
97. Beranek, L.L., I.L. Vér, and L.R. Quartararo, *Noise and vibration control engineering: Principles and applications*. Acoustical Society of America Journal, 1995. **97**(2): p. 1358-1359.
98. Sanders, W.S. and L.J. Gibson, *Mechanics of BCC and FCC hollow-sphere foams*. Materials Science and Engineering: A, 2003. **352**(1): p. 150-161.
99. Caty, O., E. Maire, and R. Bouchet, *Fatigue of Metal Hollow Spheres Structures*. Advanced Engineering Materials, 2008. **10**(3): p. 179-184.
100. Fiedler, T. and A. Öchsner, *On the anisotropy of adhesively bonded metallic hollow sphere structures*. Scripta Materialia, 2008. **58**(8): p. 695-698.
101. Taşdemirci, A., Ç. Ergönenç, and M. Güden, *Split Hopkinson pressure bar multiple reloading and modeling of a 316 L stainless steel metallic hollow sphere structure*. International Journal of Impact Engineering, 2010. **37**(3): p. 250-259.
102. Lucklum, F. and M.J. Vellekoop, *Bandgap engineering of three-dimensional phononic crystals in a simple cubic lattice*. Applied Physics Letters, 2018. **113**(20): p. 201902.
103. D'Alessandro, L., et al., *Mechanical low-frequency filter via modes separation in 3D periodic structures*. Applied Physics Letters, 2017. **111**(23): p. 231902.
104. Born, M.A.X., *Wave Propagation in Periodic Structures*. Nature, 1946. **158**(4026): p. 926-926.
105. Wang, P., et al., *Harnessing Buckling to Design Tunable Locally Resonant Acoustic Metamaterials*. Physical Review Letters, 2014. **113**(1): p. 014301.
106. Bertoldi, K. and M.C. Boyce, *Mechanically triggered transformations of phononic band gaps in periodic elastomeric structures*. Physical Review B, 2008. **77**(5): p. 052105.
107. D'Alessandro, L., et al., *Modeling and experimental verification of an ultra-wide bandgap in 3D phononic crystal*. Applied Physics Letters, 2016. **109**(22): p. 221907.
108. Li, J., V. Slesarenko, and S. Rudykh, *Microscopic instabilities and elastic wave propagation in finitely deformed laminates with compressible hyperelastic phases*. European Journal of Mechanics - A/Solids, 2019. **73**: p. 126-136.

109. Chen, Y., et al., *Harnessing multi-layered soil to design seismic metamaterials with ultralow frequency band gaps*. Materials & Design, 2019. **175**: p. 107813.
110. Brûlé, S., et al., *Experiments on Seismic Metamaterials: Molding Surface Waves*. Physical Review Letters, 2014. **112**(13): p. 133901.
111. Liu, Y., et al., *Thermomechanics of shape memory polymers: Uniaxial experiments and constitutive modeling*. International Journal of Plasticity, 2006. **22**(2): p. 279-313.
112. Brinson, L.C., *One-Dimensional Constitutive Behavior of Shape Memory Alloys: Thermomechanical Derivation with Non-Constant Material Functions and Redefined Martensite Internal Variable*. Journal of Intelligent Material Systems and Structures, 1993. **4**(2): p. 229-242.
113. Ginder, J., et al., *Controllable-stiffness components based on magnetorheological elastomers*. Proceedings of SPIE - The International Society for Optical Engineering, 2000. **3985**.
114. Ginder, J.M., et al. *Magnetorheological elastomers: properties and applications*. in *Smart Structures*. 1999.
115. Li, Y., et al., *Thermally triggered tunable vibration mitigation in Hoberman spherical lattice metamaterials*. Applied Physics Letters, 2019. **114**(19): p. 191904.
116. Molerón, M., et al., *Sound propagation in periodic urban areas*. Journal of Applied Physics, 2012. **111**(11): p. 114906.
117. Dikshit, V., et al., *Quasi-static indentation analysis on three-dimensional printed continuous-fiber sandwich composites*. 2021. **23**(2): p. 385-404.
118. Jackson, M. and A. Shukla, *Performance of sandwich composites subjected to sequential impact and air blast loading*. Composites Part B: Engineering, 2011. **42**(2): p. 155-166.
119. Kepler, J.J.J.o.S.S. and Materials, *Impact penetration of sandwich panels at different velocities—an experimental parameter study: Part II—interpretation of results and modeling*. 2004. **6**(5): p. 379-397.
120. Schubel, P.M., J.-J. Luo, and I.M. Daniel, *Impact and post impact behavior of composite sandwich panels*. Composites Part A: Applied Science and Manufacturing, 2007. **38**(3): p. 1051-1057.
121. Rathbun, H.J., et al., *Performance of metallic honeycomb-core sandwich beams under shock loading*. International Journal of Solids and Structures, 2006. **43**(6): p. 1746-1763.
122. McElroy, M., et al., *Simulation of delamination–migration and core crushing in a CFRP sandwich structure*. Composites Part A: Applied Science and Manufacturing, 2015. **79**: p. 192-202.
123. Wadley, H.N.G., et al., *Impact response of aluminum corrugated core sandwich panels*. International Journal of Impact Engineering, 2013. **62**: p. 114-128.
124. Velmurugan, R., M.G. Babu, and N.J.I.J.o.C. Gupta, *Projectile impact on sandwich panels*. 2006. **11**(2): p. 153-164.
125. Hassan, M.Z., et al., *The influence of core density on the blast resistance of foam-based sandwich structures*. International Journal of Impact Engineering, 2012. **50**: p. 9-16.
126. Yu, S., J. Sun, and J. Bai, *Investigation of functionally graded TPMS structures fabricated by additive manufacturing*. Materials & Design, 2019. **182**: p. 108021.
127. Chung, H. and S. Das, *Functionally graded Nylon-11/silica nanocomposites produced by selective laser sintering*. Materials Science and Engineering: A, 2008. **487**(1): p. 251-257.
128. Mumtaz, K.A. and N.J.J.o.m.s. Hopkinson, *Laser melting functionally graded composition of Waspaloy® and Zirconia powders*. 2007. **42**(18): p. 7647-7656.
129. Zhang, Y., et al., *Characterization of laser powder deposited Ti–TiC composites and functional gradient materials*. Journal of Materials Processing Technology, 2008. **206**(1): p. 438-444.
130. Durejko, T., et al., *Thin wall tubes with Fe3Al/SS316L graded structure obtained by using laser engineered net shaping technology*. Materials & Design, 2014. **63**: p. 766-774.

131. Choy, S.Y., et al., *Compressive properties of functionally graded lattice structures manufactured by selective laser melting*. Materials & Design, 2017. **131**: p. 112-120.
132. Dai, M., et al., *Experimental and numerical studies on compressive mechanical properties of hollow-sphere structures with perforations*. Mechanics of Materials, 2019. **134**: p. 193-203.
133. Fan, J., et al., *Dynamic crushing behavior of random and functionally graded metal hollow sphere foams*. Materials Science and Engineering: A, 2013. **561**: p. 352-361.
134. Sun, G., et al., *Experimental study on the dynamic responses of foam sandwich panels with different facesheets and core gradients subjected to blast impulse*. International Journal of Impact Engineering, 2020. **135**: p. 103327.
135. Liu, X., et al., *Blast resistance of sandwich-walled hollow cylinders with graded metallic foam cores*. Composite Structures, 2012. **94**(8): p. 2485-2493.
136. Jiang, H. and Y.J.J.o.P.D.A.P. Chen, *Lightweight architected hollow sphere foams for simultaneous noise and vibration control*. 2019. **52**(32): p. 325303.
137. McGee, O., et al., *3D printed architected hollow sphere foams with low-frequency phononic band gaps*. Additive Manufacturing, 2019. **30**: p. 100842.
138. Bonatti, C. and D. Mohr, *Large deformation response of additively-manufactured FCC metamaterials: From octet truss lattices towards continuous shell mesostructures*. International Journal of Plasticity, 2017. **92**: p. 122-147.
139. Berger, J., H. Wadley, and R.J.N. McMeeking, *Mechanical metamaterials at the theoretical limit of isotropic elastic stiffness*. 2017. **543**(7646): p. 533-537.
140. Tancogne-Dejean, T., et al., *3D plate-lattices: an emerging class of low-density metamaterial exhibiting optimal isotropic stiffness*. 2018. **30**(45): p. 1803334.
141. Sun, G., et al., *Crashworthiness design for functionally graded foam-filled thin-walled structures*. Materials Science and Engineering: A, 2010. **527**(7): p. 1911-1919.
142. Cole, G.S. and A.M. Sherman, *Light weight materials for automotive applications*. Materials Characterization, 1995. **35**(1): p. 3-9.
143. Joost, W.J.J.J., *Reducing vehicle weight and improving US energy efficiency using integrated computational materials engineering*. 2012. **64**(9): p. 1032-1038.
144. Amjad, S., S. Neelakrishnan, and R. Rudramoorthy, *Review of design considerations and technological challenges for successful development and deployment of plug-in hybrid electric vehicles*. Renewable and Sustainable Energy Reviews, 2010. **14**(3): p. 1104-1110.
145. Kobayashi, S., S. Plotkin, and S.K.J.E.E. Ribeiro, *Energy efficiency technologies for road vehicles*. 2009. **2**(2): p. 125-137.
146. Lu, G.J.P.o.t.I.o.M.E., Part F: Journal of Rail and R. Transit, *Energy absorption requirement for crashworthy vehicles*. 2002. **216**(1): p. 31-39.
147. Banhart, J.J.I.J.o.v.d., *Aluminium foams for lighter vehicles*. 2005. **37**(2-3): p. 114-125.
148. Griškevičius, P. and A.J.T. Žiliukas, *The crash energy absorption of the vehicles front structures*. 2003. **18**(2): p. 97-101.
149. Xu, P., et al., *Crash performance and multi-objective optimization of a gradual energy-absorbing structure for subway vehicles*. International Journal of Mechanical Sciences, 2016. **107**: p. 1-12.
150. Cheon, S.S., D.G. Lee, and K.S. Jeong, *Composite side-door impact beams for passenger cars*. Composite Structures, 1997. **38**(1): p. 229-239.
151. Hosseinzadeh, R., M.M. Shokrieh, and L.B. Lessard, *Parametric study of automotive composite bumper beams subjected to low-velocity impacts*. Composite Structures, 2005. **68**(4): p. 419-427.
152. Wegst, U.G., et al., *Bioinspired structural materials*. 2015. **14**(1): p. 23-36.
153. Ortiz, C. and M.C.J.S. Boyce, *Bioinspired structural materials*. 2008. **319**(5866): p. 1053-1054.

154. Dimas, L., et al., *Tough Composites Inspired by Mineralized Natural Materials: Computation, 3D printing, and Testing*. Advanced Functional Materials, 2013. **23**.
155. Mayer, G., et al., *Lessons for New Classes of Inorganic/Organic Composites from the Spicules and Skeleton of the Sea Sponge Euplectella aspergillum*. MRS Proceedings, 2004. **844**: p. Y4.2.
156. Weaver, J.C., et al., *Hierarchical assembly of the siliceous skeletal lattice of the hexactinellid sponge Euplectella aspergillum*. Journal of Structural Biology, 2007. **158**(1): p. 93-106.
157. Bechtle, S., S.F. Ang, and G.A. Schneider, *On the mechanical properties of hierarchically structured biological materials*. Biomaterials, 2010. **31**(25): p. 6378-6385.
158. Gibson, L.J., et al., *The mechanics of two-dimensional cellular materials*. Proceedings of the Royal Society of London. A. Mathematical and Physical Sciences, 1982. **382**(1782): p. 25-42.
159. Compton, B.G. and J.A. Lewis, *3D-Printing of Lightweight Cellular Composites*. Advanced Materials, 2014. **26**(34): p. 5930-5935.
160. Malek, S., et al., *Lightweight 3D cellular composites inspired by balsa*. Bioinspiration & Biomimetics, 2017. **12**(2): p. 026014.
161. Chen, Y., et al., *3D printed hierarchical honeycombs with shape integrity under large compressive deformations*. Materials & Design, 2018. **137**: p. 226-234.
162. Gibson, L.J., K.E. Easterling, and M.F. Ashby, *The structure and mechanics of cork*. Proceedings of the Royal Society of London. A. Mathematical and Physical Sciences, 1981. **377**(1769): p. 99-117.
163. Le Barbenchon, L., et al., *Multi-scale foam : 3D structure/compressive behaviour relationship of agglomerated cork*. Materialia, 2019. **5**: p. 100219.
164. Potes, F.C., J.M. Silva, and P.V. Gamboa, *Development and characterization of a natural lightweight composite solution for aircraft structural applications*. Composite Structures, 2016. **136**: p. 430-440.
165. Silva, S.P., et al., *Cork: properties, capabilities and applications*. International Materials Reviews, 2005. **50**(6): p. 345-365.
166. Song, X. and J. Zhao, *Ultrastructural study of plasmodesmata in cork cells from Quercus variabilis Blume (Fagaceae)*. Industrial Crops and Products, 2017. **97**: p. 275-280.
167. Pereira, H., *Chemical composition and variability of cork from Quercus suber L*. Wood Science and Technology, 1988. **22**(3): p. 211-218.
168. Al-Ketan, O., R. Rowshan, and R.K. Abu Al-Rub, *Topology-mechanical property relationship of 3D printed strut, skeletal, and sheet based periodic metallic cellular materials*. Additive Manufacturing, 2018. **19**: p. 167-183.
169. Bonatti, C. and D. Mohr, *Smooth-shell metamaterials of cubic symmetry: Anisotropic elasticity, yield strength and specific energy absorption*. Acta Materialia, 2019. **164**: p. 301-321.
170. Maldovan, M., et al., *Sub-Micrometer Scale Periodic Porous Cellular Structures: Microframes Prepared by Holographic Interference Lithography*. Advanced Materials, 2007. **19**(22): p. 3809-3813.
171. Ge, C., et al., *A preliminary study of cushion properties of a 3D printed thermoplastic polyurethane Kelvin foam*. Packaging Technology and Science, 2018. **31**(5): p. 361-368.
172. Ptak, M. *Method to Assess and Enhance Vulnerable Road User Safety during Impact Loading*. Applied Sciences, 2019. **9**, DOI: 10.3390/app9051000.
173. Zhang, J., et al., *Bridge Structure Dynamic Analysis under Vessel Impact Loading considering Soil-Pile Interaction and Linear Soil Stiffness Approximation*. Advances in Civil Engineering, 2019. **2019**: p. 5173132.
174. Xu, F., X. Zhang, and H. Zhang, *A review on functionally graded structures and materials for energy absorption*. Engineering Structures, 2018. **171**: p. 309-325.

175. Yin, Z., F. Hannard, and F. Barthelat, *Impact-resistant nacre-like transparent materials*. Science, 2019. **364**(6447): p. 1260-1263.
176. Lu, G. and T. Yu, *Energy absorption of structures and materials*. 2003: Elsevier.
177. Vera-Tudela, L. and M. Kühn, *Analysing wind turbine fatigue load prediction: The impact of wind farm flow conditions*. Renewable Energy, 2017. **107**: p. 352-360.
178. Tuo, H., et al., *An experimental and numerical investigation on low-velocity impact damage and compression-after-impact behavior of composite laminates*. Composites Part B: Engineering, 2019. **167**: p. 329-341.
179. Shan, S., et al., *Multistable Architected Materials for Trapping Elastic Strain Energy*. Advanced Materials, 2015. **27**(29): p. 4296-4301.
180. McKittrick, J., et al., *Energy absorbent natural materials and bioinspired design strategies: A review*. Materials Science and Engineering: C, 2010. **30**(3): p. 331-342.
181. Kumar, S., et al., *Tunable Energy Absorption Characteristics of Architected Honeycombs Enabled via Additive Manufacturing*. ACS Applied Materials & Interfaces, 2019. **11**(45): p. 42549-42560.
182. Papka, S.D. and S. Kyriakides, *In-plane compressive response and crushing of honeycomb*. Journal of the Mechanics and Physics of Solids, 1994. **42**(10): p. 1499-1532.
183. Tattersall, H.G. and G. Tappin, *The work of fracture and its measurement in metals, ceramics and other materials*. Journal of Materials Science, 1966. **1**(3): p. 296-301.
184. Li, J., et al., *Analytical, numerical, and experimental studies of viscoelastic effects on the performance of soft piezoelectric nanocomposites*. Nanoscale, 2017. **9**(37): p. 14215-14228.
185. Wang, Y., et al., *Architected lattices with adaptive energy absorption*. Extreme Mechanics Letters, 2019. **33**: p. 100557.
186. Tao, H. and J. Gibert, *Multifunctional Mechanical Metamaterials with Embedded Triboelectric Nanogenerators*. Advanced Functional Materials, 2020. **30**(23): p. 2001720.
187. Xu, H., et al., *Piezoelectric properties of triply periodic minimum surface structures*. Composites Science and Technology, 2020. **200**: p. 108417.
188. Song, X., et al., *Additive Manufacturing of Bi-Continuous Piezocomposites With Triply Periodic Phase Interfaces for Combined Flexibility and Piezoelectricity*. Journal of Manufacturing Science and Engineering, 2019. **141**(11).
189. Gibiansky, L.V., S.J.J.o.t.M. Torquato, and P.o. Solids, *On the use of homogenization theory to design optimal piezocomposites for hydrophone applications*. 1997. **45**(5): p. 689-708.
190. Yoon, G., H. Choi, and S. Hur, *Multiphysics topology optimization for piezoelectric acoustic focuser*. Computer Methods in Applied Mechanics and Engineering, 2017. **332**.
191. de Almeida, B. and R. Pavanello, *Topology Optimization of the Thickness Profile of Bimorph Piezoelectric Energy Harvesting Devices*. Journal of Applied and Computational Mechanics, 2019. **5**: p. 113-127.
192. Chen, S., et al., *A level set approach for optimal design of smart energy harvesters*. Computer Methods in Applied Mechanics and Engineering, 2010. **199**(37): p. 2532-2543.
193. Yuan, R., et al., *The Search for BaTiO₃-Based Piezoelectrics With Large Piezoelectric Coefficient Using Machine Learning*. IEEE Trans Ultrason Ferroelectr Freq Control, 2019. **66**(2): p. 394-401.
194. Wang, S. and M.Y. Wang, *Radial basis functions and level set method for structural topology optimization*. International Journal for Numerical Methods in Engineering, 2006. **65**(12): p. 2060-2090.
195. Subbiah, N., et al., *Detection of material interfaces using a regularized level set method in piezoelectric structures*. Inverse Problems in Science and Engineering, 2015. **24**: p. 1-24.
196. Luo, Z., et al., *Design of piezoelectric actuators using a multiphase level set method of piecewise constants*. 2009. **228**(7 %J J. Comput. Phys.): p. 2643–2659.

197. Porn, S., et al., *Level set based structural optimization of distributed piezoelectric modal sensors for plate structures*. 2016. **80**: p. 348-358.
198. Araki, K. and J.W. Halloran, *New Freeze-Casting Technique for Ceramics with Sublimable Vehicles*. Journal of the American Ceramic Society, 2004. **87**(10): p. 1859-1863.
199. Yoon, B.-H., et al., *Generation of Large Pore Channels for Bone Tissue Engineering Using Camphene-Based Freeze Casting*. Journal of the American Ceramic Society, 2007. **90**(6): p. 1744-1752.
200. Koh, Y.-H., et al., *Effect of Polystyrene Addition on Freeze Casting of Ceramic/Camphene Slurry for Ultra-High Porosity Ceramics with Aligned Pore Channels*. Journal of the American Ceramic Society, 2006. **89**(12): p. 3646-3653.
201. McCall, W.R., et al., *Piezoelectric Nanoparticle-Polymer Composite Foams*. ACS Applied Materials & Interfaces, 2014. **6**(22): p. 19504-19509.
202. Cheng, K.-T. and N. Olhoff, *An investigation concerning optimal design of solid elastic plates*. International Journal of Solids and Structures, 1981. **17**(3): p. 305-323.
203. Zhou, M. and G.I.N. Rozvany, *The COC algorithm, Part II: Topological, geometrical and generalized shape optimization*. Computer Methods in Applied Mechanics and Engineering, 1991. **89**(1): p. 309-336.
204. Sigmund, O., *Morphology-based black and white filters for topology optimization*. Structural and Multidisciplinary Optimization, 2007. **33**(4): p. 401-424.

CURRICULUM VITAE

Name: Huan Jiang

Address: 2565 S University Blvd, 80210

Email: huan.jiang@louisville.edu

EDUCATION

University of Louisville 01/2019-02/2023

Major: Mechanical Engineering

Degree: PhD

University of Chinese Academy of Sciences 09/2013-06/2016

Major: Geotechnical Engineering

Degree: Master

Changsha University of Sciences and Technology 09/2009-06/2013

Major: Civil Engineering

Degree: Bachelor

PUBLICATIONS

Fatih Usta, Zhennan Zhang, **Huan Jiang**, Yanyu Chen. Harnessing structural hierarchy and multi-material approaches to improve crushing performance of re-entrant honeycombs.

Journal of Manufacturing Processes, 92 (2023)

Huan Jiang, Hannah Ziegler, Zhennan Zhang, Heng Zhang, Louise Le Barbenchon, Sundar Atre, Yanyu Chen. 3D printed tubular lattice metamaterials for mechanically robust stents. Composites Part B: Engineering, 236, 109809 (2022)

Jing Li, Ying Yang, **Huan Jiang**, Yunhe Wang, Yanyu Chen, Shenglin Jiang, Jia-Min Wu, Guangzu Zhang. 3D interpenetrating piezoceramic-polymer composites with high

damping and piezoelectricity for impact energy-absorbing and perception. *Composites Part B: Engineering*, 232, 109617 (2022)

Huan Jiang, Hannah Ziegler, Zhennan Zhang, Sundar Atre, Yanyu Chen. Bending behavior of 3D printed mechanically robust tubular lattice metamaterials. *Additive Manufacturing*, 50, 102565 (2022)

Han Meng, Wael Elmadih, **Huan Jiang**, Tristan Lawrie, Yanyu Chen, and Dimitrios Chronopoulos. Broadband vibration attenuation achieved by additively manufactured 3D rainbow hollow sphere foams. *Applied Physics Letters*, 119, 181901 (2021)

Jing Li, Tianyu Wu, **Huan Jiang**, Yanyu Chen, Qibiao Yang. Ultrasensitive Hierarchical Piezoresistive Pressure Sensor for Wide-Range Pressure Detection. *Advanced Intelligent Systems*, 2100070 (2021)

Huan Jiang, Aaron Coomes, Zhennan Zhang, Hannah Ziegler, Yanyu Chen. Tailoring 3D printed graded architected polymer foams for enhanced energy absorption. *Composites Part B: Engineering*, 224, 109183 (2021)

Fangzhou Wang, **Huan Jiang**, Yanyu Chen, Xianglin Li. Predicting thermal and mechanical performance of stochastic and architected foams. *International Journal of Heat and Mass Transfer*, 171, 121139 (2021)

Huan Jiang, Louise Le Barbenchon, Brett A Bednarczyk, Fabrizio Scarpa, Yanyu Chen. Bioinspired multilayered cellular composites with enhanced energy absorption and shape recovery. *Additive Manufacturing*, 36, 101430 (2020)

Huan Jiang, Hannah Ziegler, Zhennan Zhang, Han Meng, Dimitrios Chronopoulos, Yanyu Chen. Mechanical properties of 3D printed architected polymer foams under large deformation. *Material and Design*, 194, 108946 (2020)

Huan Jiang, Zhennan Zhang, Yanyu Chen. 3D printed tubular lattice metamaterials with engineered mechanical performance. *Applied Physics Letters*, 117, 011906 (2020)

Olivia McGee, **Huan Jiang**, Feng Qian, Zian Jia, Lifeng Wang, Han Meng, Dimitrios Chronopoulos, Yanyu Chen, Lei Zuo. 3D printed architected hollow sphere foams with low-frequency phononic band gaps. *Additive Manufacturing*, 30, 100842 (2019)

Huan Jiang, Yanyu Chen. Lightweight architected hollow sphere foams for simultaneous noise and vibration control. *Journal of Physics D: Applied Physics*, 52, 325303 (2019)

CONFERENCE PRESENTATIONS

Huan Jiang, Louise Le Barbenchon, Brett Bednarczyk, Fabrizio Scarpa, Yanyu Chen, “Bioinspired Architected Composites with Enhanced Energy Absorption”, *Bulletin of the American Physical Society- Virtual, Conference Presentation*, 2021.

Huan Jiang, Hannah Ziegler, Zhennan Zhang, Yanyu Chen, “3D Printed Tubular Lattice Structure with Robust Mechanical Properties”, *Society of Engineering Science Annual Conference- Virtual, Conference Presentation*, 2021.

Huan Jiang, Aaron Coomes, Zhennan Zhang, Hannah Ziegler, Yanyu Chen, “Graded Polymer Foams with Enhanced Energy Absorption”, *SPIE Smart Structures + Nondestructive Evaluation- CA, Long Beach, Conference Presentation*, 2022.

Huan Jiang, Hannah Ziegler, Zhennan Zhang, Yanyu Chen, “3D Printed Tubular Lattice Metamaterials with Enhanced Mechanical Properties”, Society of Engineering Science Annual Conference- MD, Baltimore, Conference Presentation, 2022.

Huan Jiang, Hannah Ziegler, Zhennan Zhang, Yanyu Chen, “3D printed tubular metamaterials with enhanced mechanical properties”, The 10th International Conference on Multiscale Materials Modeling- MD, Baltimore, Conference Presentation, 2022.

Huan Jiang, Yanyu Chen, “Isotropic hybrid architected foams with enhanced energy absorption”, SPIE Smart Structures + Nondestructive Evaluation- CA, Long Beach, Conference Presentation, 2023.

AWARDS

- Conference Travel Award for attending The 10th International Conference on Multiscale Materials Modeling (2022).
- Conference Travel Award for attending SPIE Smart Structures + Nondestructive Evaluation (2023).
- Chinese Government Award for Outstanding Self-financed Students Abroad (2022)